UNIVERSITE LIBANAISE
ECOLE DOCTORALE DES SCIENCES ET DE TECHNOLOGIE

Master 2 Research Report

A Thesis Submitted in Partial Fulfillment of the
Requirements for the Degree of

MECANIQUE 3M

A Comparative Study of Static and Fatigue Behaviors for Various Composite Orthotropic Properties for a Wind Turbine Using a Coupled FEM-BEM Method

Presented By: **Adam Rafic Chehouri**

Supervised the **16/07/2013**   Supervisory Committee:

Dr. Mazen Ghandour   Member of Jury

Dr. Khalil Khoury   Member of Jury

Dr. Rafic Younes   Supervisor

ABSTRACT

In the wind industry, the current trend is towards building larger and larger turbines. This presents additional structural challenges and requires blade materials that are both lighter and stiffer than the ones presently used. [1] This work is aimed to aid the work of designing new wind turbine blades by providing a comparative study of different composite materials.

A coupled Finite-Element-Method (FEM) - Blade Element Momentum (BEM) code was used to simulate the aerodynamic forces subjected on the blade. The developed BEM code was written using LabView allowing an iterative numerical approach solver taking into the consideration the unsteady aerodynamic effects and off –design performance issues such as Tip Loss, Hub Loss and Turbulent Wake State therefore developing a more rational aerodynamic model. For this thesis, the finite element study was conducted on the Static Structural Workbench of ANSYS, as for the geometry of the blade it was imported from a previous study prepared by Cornell University [2]. Confirmation of the performance analysis of the chosen wind turbine blade are presented and discussed blade including the generated power, tip deflection, thrust and tangential force for a steady flow of 8m/s.

The elastic and ultimate strength properties were provided by Hallal et al [3]. The Tsai-Hill and Hoffman failure criterions were both conducted to the resulting stresses and shears for each blade composite material structure to determine the presence of static rupture. A progressive fatigue damage model was conducted to simulate the fatigue behavior of laminated composite materials, an algorithm developed by Shokrieh [4].

It is concluded that with respect to a material blade design cycle, the coupling between a finite element package and blade element and momentum code under steady and static conditions can be useful. Especially when an integration between this coupled approach and a dynamic simulation tool could be established, a more advanced flexible blade design can be then analyzed for a novel generation of more flexible wind turbine blades.

Keywords: wind turbine blade − BEM − FEM − aerodynamic − orthotropic − static − fatigue

ACKNOWLEDGMENTS

May be the last few month were exhausting and full of challenges, but what I find most difficult at this time is writing the few words to come that has to summarize me acknowledgement.

May be the best way, is to name the names of few that their presence was indispensable and their efforts must be marked. My professor and master thesis coordinator, Dean Rafic Younes, who has been an inspiration, a leader and a researcher colleague that has supported me since the first day till present.

Dr Mazen Ghandour, I would not have been in this current position today without your continuous contributions and all of your support will never be forgotten.

To Dr Hussein Ibrahim and the team of TechnoCentre Éolien in Gaspé Québec a special appreciation, they have been threw out my research internship a second family that not only offered professional assistance for my thesis but also made room for me in there life.

To all my colleagues, classmates, academic staff at the Faculty of Engineering and the EDST at the Lebanese University, the best of success and much love.

Lastly, all of my achievements derive from one source, my loving family, to whom I owe all of my success, overcoming many struggles and prevailing over many cynics.

"Parce qu'aimer c'est renoncer à la force"
Milan Kundera

TABLE OF CONTENTS

NOMENCLATURE

Latin Symbols

a	- Induction factor	[-]
a'	- Tangential induction factor	[-]
A	- Area	[m²]
c	- Chord	[m]
C_D	- 2-D Drag coefficient	[-]
C_L	- 2-D Lift coefficient	[-]
C_N	- 2-D normal direction coefficient	[-]
C_{Tang}	- 2-D tangential direction coefficient	[-]
C_T	- Coefficient of thrust	[-]
D	- Drag force	[N]
E	- Stiffness	[N/m²]
f	- Glauert correction	[-]
F_{tip}	- Tip loss correction factor	[-]
F_{hub}	- Hub loss correction factor	[-]
H	- Total head	[N/m²]
L	- Lift force	[N]
m	- Mass	[kg]
m_{aero}	- Aerodynamic moment per unit of length	[N]
M_{corr}	- Correction moment per unit of length	[N]
M	- Induced moment	[N.m]
n	- Number of cycles	[-]
N	- Number of blades	[-]
P	- Pressure	[N/m²]
P_N	- Resultant in the normal direction	[N]
P_T	- Resultant in the tangential direction	[N]
r	- Local radius position	[m]
R	- Tip blade radius position	[m]
R	- Stress ratio	[-]
R	- Residual strength	[N/m²]
R_{hub}	- Hub position	[m]

T	- Thrust	[N]
V_0	- Undisturbed air stream	[m/s]
v	- Velocity	[m/s]
v_f	- Fiber content	[-]

Greek Symbols

α	- Angle of attack	[rd]
β	- Comparative parameter	[-]
δ	- Material nonlinearity parameter	[-]
θ	- Pitch angle	[rd]
ρ	- Air density	[kg.m^3]
σ	- Stress	[N/m^2]
σ '	- Local solidity	[-]
χ	- Average of $f(\sigma)$	[-]
$\emptyset$	- Relative flow angle	[rd]
ω	- Rotational velocity	[rd/s]
Ω	- Rotation of the wind near the blade	[rd/s]
ϑ	- Standard deviation	[-]

Abbreviations

ADAMS/WT	- Automatic Dynamic Analysis of Mechanical Systems - Wind Turbine
BEM	- Blade Element Momentum Theory
CFD	- Computational Fluid Dynamics
FAST	- Fatigue, Aerodynamics, Structures, and Turbulence
FEM	- Finite Element Method
HAWC	- Horizontal Axis Wind Turbine Code
NACA	- National Advisory Committee for Aeronautics
NREL	- National Renewable Energy Laboratory
REV	- Representative Elementary Volume

LIST OF FIGURES

LIST OF TABLES

CHAPTER I: LITERATURE REVIEW

1.1 Background

Until recently, wind turbine blades had a relative high rigidity and small deformations. This allowed for modeling techniques which assumed a simplified aeroelastic response. Recent reports have shown that an aeroelastic optimized flexible blade can offer a number of advantages over the more rigid variant: higher energy yield and/or shedding loads (increasing fatigue life) [5]. Consequently, there is a trend towards lighter and more flexible wind turbines, which makes design and dimensioning even more demanding and important [6].

Wind turbines operate in a hostile environment where strong flow fluctuations, due to the nature of the wind, can excite high loads. The varying loads, together with an elastic structure, create a perfect breeding ground for induced vibration and resonance problems [6]. Many manufactured items are designed to a reference "design point". This corresponds to an operating condition such that, if met it will perform adequately to any other set of conditions. A single design point is not adequate, but rather the wind turbine must be able to withstand other unusual conditions with no significant damage. The most important considerations are [7]:

1. Expect event during normal operation
2. Extreme events
3. Fatigue

As is commonly used in mechanics, the loads are the externally applied forces or moments to the entire turbine or to any of the components considered separately. Wind turbines are usually designed for two types of loads (1) ultimate loads and (2) fatigue loads. Ultimate loads refer to likely maximum loads, multiplied by a safety factor. Fatigue loads refer to the component's ability to withstand an expected number of cycles of possibly varying magnitude [7]. Most Materials can withstand a load of a certain magnitude when applied once, but cannot withstand the same load when applied in a cyclic pattern. The decreasing ability to survive repeated loads is called fatigue.

1.2 Scopes and Aims

The goal of this project is to develop a comparative study of different composite material structures, a study that will be based on their quasi- static and fatigue behavior subjected to the same aerodynamic load. The majority of the aeroelasticity models are based on a modal formulation or finite element (FE) representation. However a coupled FEM-BEM method was used in this work to calculate the aeroelastic response and compare the static failure performance knowing the ultimate strengths of each material. The use of computation fluid dynamics (CFD) rather than BEM is due to the fact that a computational fluid dynamic simulation is time consuming and hence considered to be impractical for the purpose of our study (see figure 1.1). The BEM offers the advantage of having short computation time and the model can be simulated without difficulty.

FEM – BEM

Structure Study (deformation and stress analysis)

Determine the aerodynamic loading knowing the geometric parameters

FEM – CFD

Structure Study (deformation and stress analysis)

Determine the aerodynamic loading due to unavailability of the coefficients of lift, drag and moment
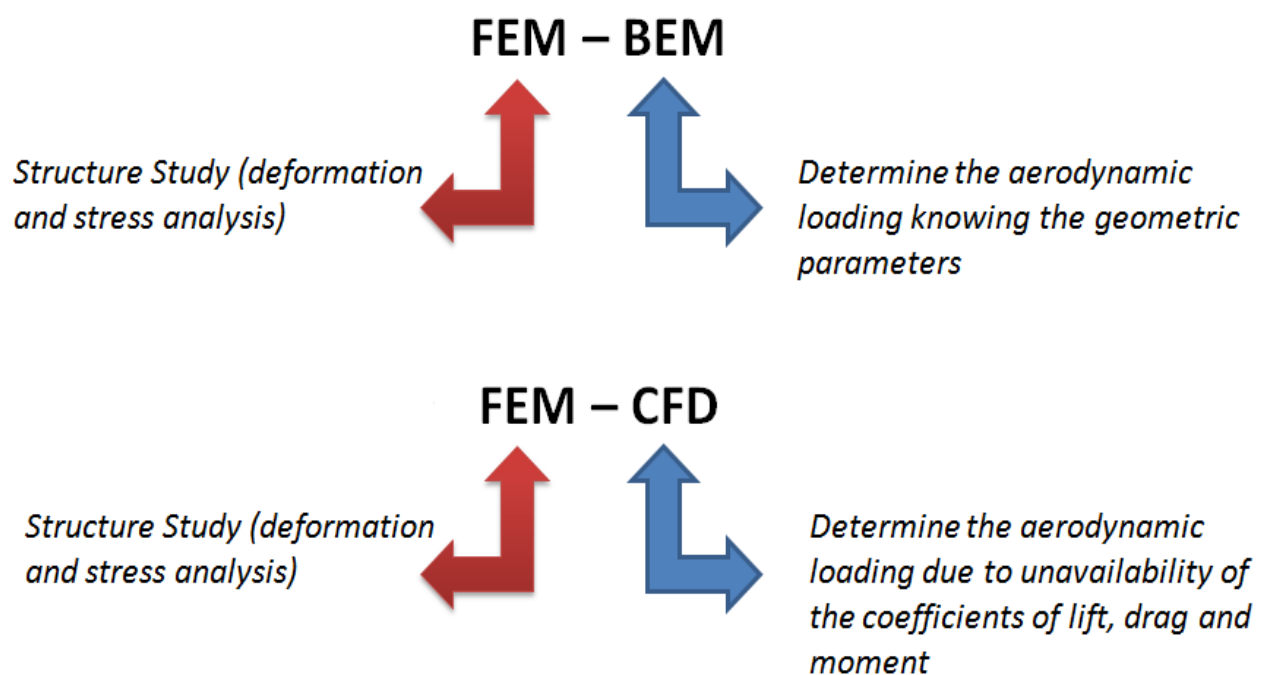
Figure 9.1: Comparison between two method solving strategies; FEM-BEM and FEM-BEM

A number of design codes have been used over to model the wind turbines dynamic behavior, or to carry out design calculations. Listed below are some of the most common design codes:

- ADAMS/WT (Automatic Dynamic Analysis of Mehhhhhhhchanical Systems – Wind Turbine). ADAMS/WT is designed as an application-specific add-on to ADAMS/SOLVER and ADAMS/View and it is a toolkit for analyzing wind-turbine aeromechanics [8].

- FAST (Fatigue, Aerodynamics, Structures, and Turbulence). The FAST code is being developed through a subcontract between National Renewable Energy Laboratory (NREL) and Oregon State University. NREL has modified FAST to use the AeroDyn subroutine package developed at the University of Utah to generate aerodynamic forces along the blade [9].

- HAWC (Horizontal Axis Wind Turbine Code). HAWC is developed at Risø in Denmark. The model is based on the FE method using the substructure approach. The code predicts the response of horizontal axis two- or three bladed machines in time domain [10]

- YawDyn. YawDyn is developed at the Mechanical Engineering Department University of Utah, with support of the National Renewable Energy Laboratory (NREL), National Wind Technology Center. YawDyn simulates e.g. the yaw motions or loads of a horizontal axis wind turbine, with a rigid or teetering hub [11].

Finally, this thesis will serve as an aid and a step towards the design of a more lightweight blade and hope that it will serve as a tool that will aid the design of new wind turbine blade composite material. This tool can be used to evaluate the pros and cons of using more lightweight material and their behavior for different operating condition

CHAPTER II: AERODYNAMIC MODELINGh

2.1 Methods for Calculating the Aerodynamic Forces

As mentioned earlier the aerodynamic forces used in this thesis are calculated using the Blade Element Momentum (BEM) method, which is described in this chapter. The BEM theory is the most commonly used method for calculating aerodynamic loads in the wind-power industry [1].

Other methods such as the Helical Vortex Method (HVM) and the Free Vortex Method (FVM) are not much used for wind turbines yet, but find great application in the helicopter industry and in the propeller industry. The most advanced ones are numerical methods solving the Navier-Stokes equations for the global compressible flow as well as the flow near the blades [6]. These methods may see increasing use in the wind-power industry as well.

2.2 BEM Model

2.2.1   Introduction

BEM is a very common tool for wind turbine applications; it offers the advantage of having a very short computational time and good accuracy, at least for the cases for which BEM is suitable for. In short, the benefits of BEM are:

- Very fast.
- Accurate.

The disadvantages are:

- No way to define the geometry in flap or edge wise direction, (for example pre-bend or a curved blade).
- Engineering models needed.

BEM can accurately be used when the blade is straight (no complicated shapes in either direction), and the analysis is done assuming a steady state. The actuator disc model used to derive the momentum equations assumes an infinite number of blades but in reality

wind turbines will have only two or three blades, therefore not every air particle passing through the rotor swept area will be strongly affected by the pressure fields of the blades of the wind turbine. To compensate for this fact, so-called tip-loss corrections can be used. These corrections will reduce the induction factor in the outer annuli and therefore the aerodynamic forces acting near the tip [12].

2.2.2   BEM Theory

The Blade Element Momentum (BEM) theory[1] is a very widely used method for calculating the forces on a wind turbine [1]. It is actually the combination of *blade element theory* (also known as strip theory) and *momentum theory*.

Blade element theory divides the blade into discrete 2D sections, for which the aerodynamic lift and drag forces per unit length are calculated based on local values of pitch angle, angle of attack, chord length, airfoil section lift/drag coefficients, induction and wind speed. Note that the wind speed is the vectorial sum of the free stream velocity and the rotational induced velocity. Further, the aerodynamic coefficients of the 2D airfoil section have to be known as function of angle of attack. See figure 2.1.
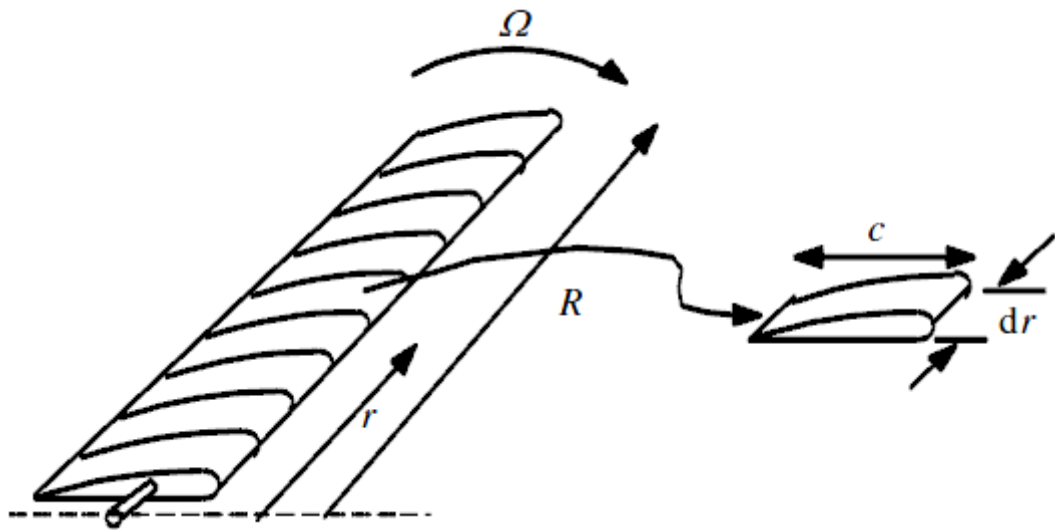
Figure 10.1: Schematic of blade elements; c, airfoil chord length; *dr*, radial length of element; *r*, radius; *R*, rotor radius; Ω, angular velocity of rotor

The momentum theory relates rotor thrust to the induction over the rotor plane. The induction could be interpreted as the change in wind speed conditions due to the presence of the lift and drag generating rotor blades [5].

By using the actuator disk theory where the disk changes the pressure and the rotation of the fluid, and couple it with blade theory a

[1]The derivations shown in this chapter have been extracted from [9] and [10]

very fast tool can be created [1]. The actuator disk theory assumes that the blade is replaced by a circular plane that changes the pressure, and creates a rotational force on the fluid, see figure 2.2.
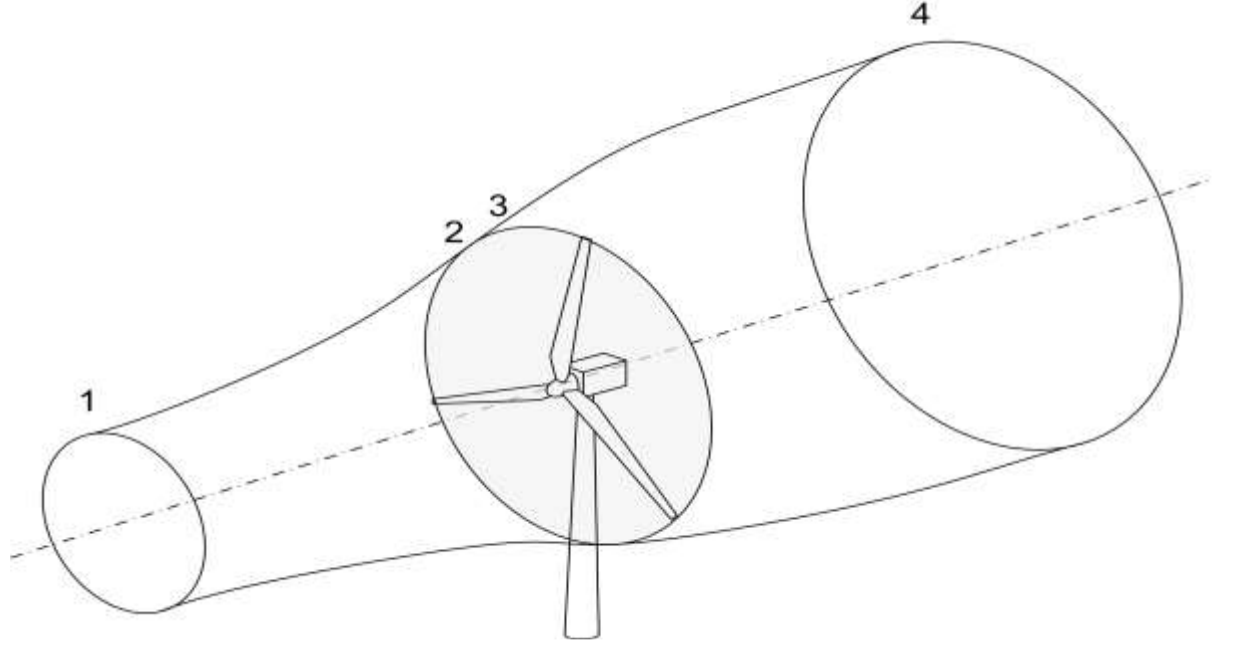
Figure 2.2: Actuator disk model

By the actuator disk theory the thrust can be calculated as the pressure drop over the disk.

$$T = \Delta p . A \tag{2.1}$$

and the induced moment can be calculated as:

$$dM = \rho u \omega r^2 dA \tag{2.2}$$

where Δp is the pressure drop and A is the area of the disk i.e.

$$\Delta p = p_2 - p_3 \tag{2.3}$$

$$A = \pi r^2 \tag{2.4}$$

assuming that the flow is incompressible and stationary Bernoulli's equation can be used to calculate p_2 and p_3. This is done by calculating the state far upstream of the blade, and just before it (between 1 and 2) and calculating the state for far downstream of the blade and just after it (between 4 and 3).

$$H_1 = p_1 + \frac{\rho u_1^2}{2} = p_2 + \frac{\rho u_2^2}{2} \tag{2.5}$$

$$H_2 = p_3 + \frac{\rho (u_3^2 + (\omega_3 r)^2)}{2} = p_4 + \frac{\rho (u_4^2 + (\omega_4 r)^2)}{2} \tag{2.6}$$

where:

$$\Delta p = p_2 - p_3 \Rightarrow p_3 = p_2 - \Delta p$$

also

$$\Delta v = 0 = v_2 - v_3 \Rightarrow v_2 = v_3 \tag{2.7}$$

and
$$p_1 = p_4 \tag{2.8}$$

adding equations these equations and you get:

$$H1 = p_1 + \frac{\rho u_1^2}{2} = p_2 + \frac{\rho u_2^2}{2} \tag{2.9}$$

$$H2 = p_2 - \Delta p + \frac{\rho(u_3^2 + (\omega_3 r)^2)}{2} = p_1 + \frac{\rho(u_4^2 + (\omega_4 r)^2)}{2} \tag{2.10}$$

by combining these equations the head drop can be calculated as:

$$\Delta H = -\Delta p + \rho \omega_3^2 r_3^2 / 2 \tag{2.11}$$

where the total pressure head also can be calculated as:

$$0 = p_1 - p_4 = \frac{\rho(u_4^2 - u_1^2)}{2} + \frac{\rho(\omega_4^2 r_4^2 - \omega_3^2 r_3^2)}{2} + \Delta p \tag{2.12}$$

due to the fact that $\Delta H = 0$, the pressure drop over the blade can be written as:

$$\Delta p = \rho(\Omega + \frac{\omega}{2})\omega r_3^2 \tag{2.13}$$

where Ω is the rotation of the wind close to the blade.

By combining these equations the total pressure drop can be calculated as:

$$0 = \frac{\rho(u_4^2 - u_1^2)}{2} + \rho \omega_4^2 r_4^2 (\Omega + \frac{\omega}{2}) \tag{2.14}$$

since the angular velocity omega is supposed to be small, the term ω_2 can be neglected. By applying these assumptions, on the actuator disk model the thrust and the moment can be calculated as:

$$dT = (u_1 - u_4)dm = 2\pi r \rho r_3 u_1 (u_1 - u_4)dr \tag{2.15}$$

Similarly the momentum can be calculated as

$$dM = r\omega dm = 2\pi \rho u_1 r_3^2 \omega dr \tag{2.16}$$

where m is the mass of the fluid.

By substituting some variables, these equations can be written as:

$$dT = (V_0 - u_1)d\dot{m} = 2\pi \rho u(V_0 - u_1)dr \tag{2.17}$$

$$dM = rC_\theta d\dot{m} = 2\pi r^2 \rho u C_\theta dr \tag{2.18}$$

By expressing u as $u = (1 - 2a)V_0$ these two equations can be written as:

$$dT = 4\pi r \rho V_0^2 a(1 - a)dr \tag{2.19}$$

$$dM = 4\pi r^3 \rho V_0 \omega(1 - a)a'dr \tag{2.20}$$

The axial induction factor and the tangential induction factor can be defined respectively

by:
$$a = \frac{u_1 - u_2}{u_1} \quad a' = \frac{\Omega}{2\omega}$$

and the angle of attack can be calculated as:

$$\alpha = \phi - \Theta \tag{2.21}$$

where: ϕ is the relative flow angle

Θ is the pitch angle (see figure 2.3)
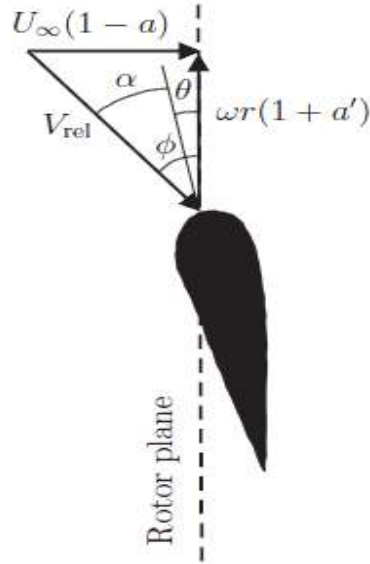
Figure 2.3: Velocities at the rotorplane

where:
$$\tan(\phi) = \frac{(1-a)V_0}{(1+a')\omega r}$$

(2.22)

which makes it possible to calculated the lift and the drag:

$$L = 1/2 \rho V_{rel}^2 c C_L \qquad (2.23)$$

$$D = 1/2 \rho V_{rel}^2 c C_D \qquad (2.24)$$

where C_L and C_D can be gathered from tabulated data (see figure 2.4).
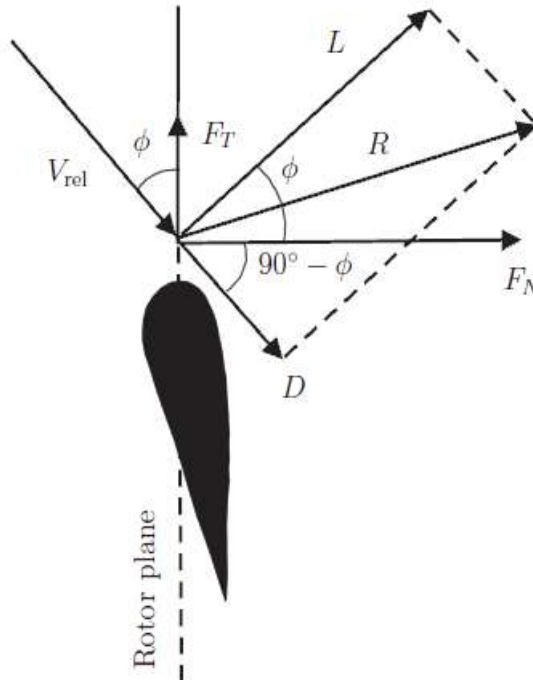
Figure 2.4: The local forces on a cross section of a blade

The lift and drag is calculated in the same direction as the flow. However a better way of dividing the forces is in the normal and tangential direction, compared to the rotor plane. By calculating the forces as:

$$P_N = L.\cos(\phi) + D.\sin(\phi) \tag{2.25}$$

$$P_T = L.\sin(\phi) - D.\cos(\phi) \tag{2.26}$$

or doing it already for the coefficients :

$$C_N = C_L.\cos(\phi) + C_D.\sin(\phi) \tag{2.27}$$

$$C_{Tang} = C_L.\sin(\phi) - C_D.\cos(\phi) \tag{2.28}$$

they can therefore be expressed as this:

$$C_N = \frac{P_N}{1/2\rho V_{rel}^2 c} \tag{2.29}$$

$$C_{Tang} = \frac{P_T}{1/2\rho V_{rel}^2 c} \tag{2.30}$$

when using the formulation as above the thrust and moment can be calculated as:

$$dT = N_B P_N dr \tag{2.31}$$

$$dM = r N_B P_T dr \tag{2.32}$$

inserting these equation into equations 2.19 and 2.20 the thrust can be calculated as:

$$dT = 1/2\rho N_B \frac{V_0^2(1-a)^2}{sin^2(\phi)} c C_N dr \tag{2.33}$$

$$dM = 1/2\rho N_B \frac{V_0(1-a)\omega r(1+a')}{sin(\phi).cos(\phi)} c C_{Tang} r dr \tag{2.34}$$

which means that the indical functions a and a' can be calculated as:

$$a = \frac{1}{1 + \frac{4sin^2(\phi)}{\sigma C_N}} \tag{2.35}$$

$$a' = \frac{1}{1 + \frac{4 sin(\phi)cos(\phi)}{\sigma C_N}} \tag{2.36}$$

where σ, the local solidity can be calculated as:

$$\sigma(r) = \frac{c(r)N_B}{2\pi r} \tag{2.37}$$

Using these equations and following the numerical procedure seen in figure 2.5 the forces on the blade can be easily calculated. Most of the loads and the directions are illustrated in figure 2.6.

A preliminary code was developed that allowed the convergence of the two induction factors and hence giving the loads on each element of the blade. Despite its simplicity, the BEM theory provides relatively accurate results. There are other aerodynamic effects on a real turbine, which cannot be directly modeled by the BEM code because of the assumptions made in the theory. These are effects due to heavy loaded rotors with high induction factors, blade tip loss and hub loss, mainly due to a limited number of blades and skewed inflow which is not perpendicular to the rotor plane [15].
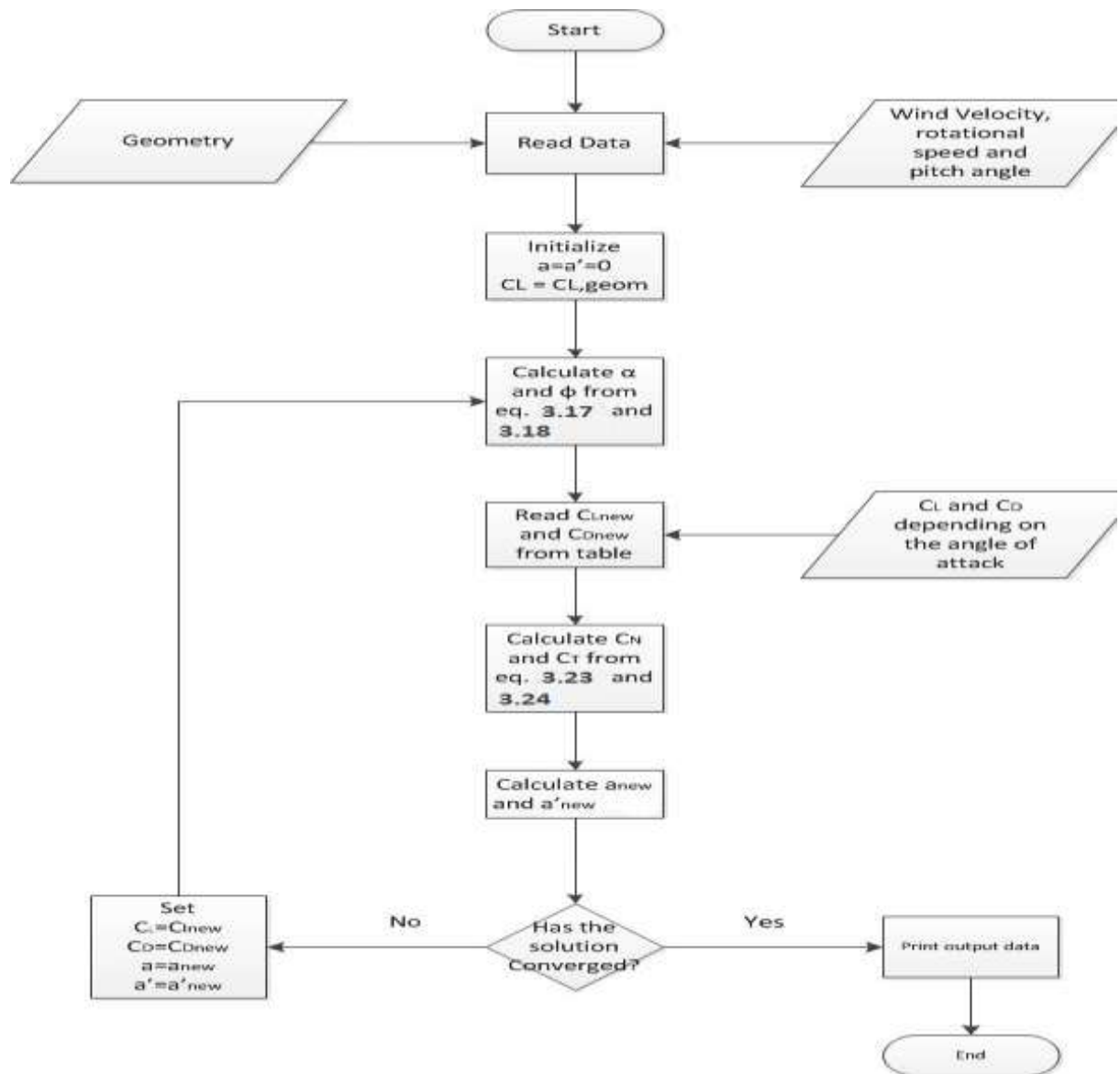
Figure 2.5: The numerical approach when using BEM
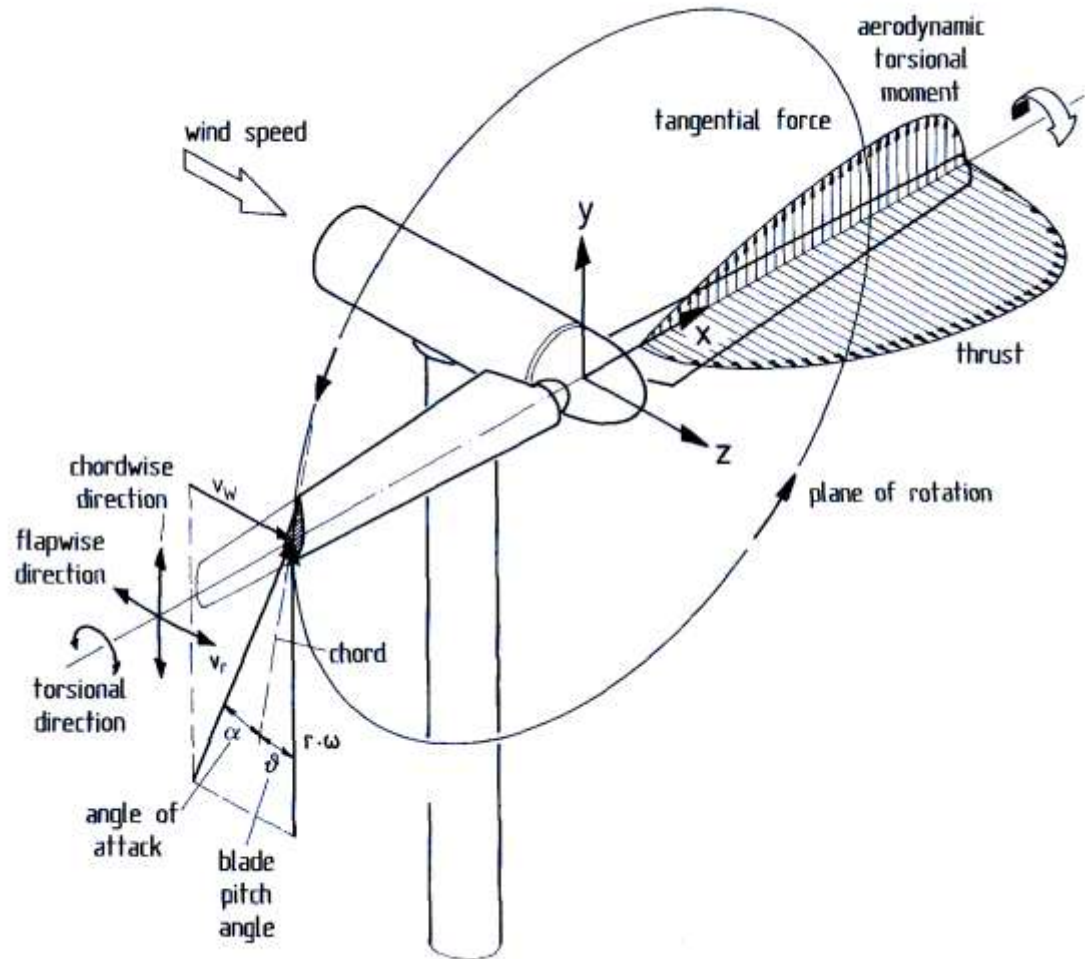
Figure 2.6: Terms used for representing displacements, loads and stresses on the rotor. Reproduced from [16]

2.2.3 Correction Models

I. <u>Prandtl's Tip Loss factor</u>

Because the pressure on the suction side of a blade is lower than that on the pressure side, air tends to flow around the tip from the lower to upper surface, reducing lift and hence power production near the tip. This effect is most noticeable with fewer, wider blades [7].

A number of methods have been suggested for including the effect of the tip loss but the most straightforward approach in use is the one developed by Prandtl. According to this method, a correction factor, *F,* must be introduced into the previously discussed equations. This correction factor is a function of the number of blades, relative wind angle, and the position on the blade. Based on Prandtl's method [7]:

$$F_{tip} = \frac{2}{\pi} cos^{-1}\{exp(-f)\} \tag{2.38}$$

f is a part in the so-called *Glauert correction factor* which can be calculated as:

$$f = \frac{N(R-r)}{2rsin(\varphi)}$$

where the angle resulting from the inverse cosine function is assumed to in radians. Note, also that F is always between 0 and 1. This tip loss correction factor characterizes the reduction in the forces at a radius r along the blade.

The tip loss correction factor affects the forces derived from momentum theory. Thus equations 2.19 and 2.20 become:

$$dT = F\pi r \rho V_0^2 4a(1-a)dr \tag{2.39}$$

$$dM = 4Fa'(1-a)\rho V_0 \pi r^3 \omega dr$$

(2.40)

This modification in the momentum affects the values of *a* and *a'*. So instead of the equations 2.35 and 2.36, with Prantl's tip loss factor the equations 2.41 and 2.41 should be used. [14]

$$a = \frac{1}{1+\frac{4Fsin^2(\phi)}{\sigma C_N}} \tag{2.41}$$

$$a' = \frac{1}{1+\frac{4F\,sin(\phi)cos(\phi)}{\sigma C_N}} \tag{2.42}$$

II.   Prandtl's Hub Loss factor

Similarly to the tip loss, a correction for the induced velocity resulting from a vortex being shed near the hub of the rotor is also taken into consideration. The hub-loss model uses a nearly identical implementation of the Prandtl tip-loss model to describe the effect of this vortex, replacing Equation 2.38 with the following:

$$f = \frac{N(r-R_{hub})}{2rsin(\varphi)} \tag{2.43}$$

For a given element, the local aerodynamics may be affected by both the tip loss and hub loss, in which case the tip-loss and hub-loss correction factors are multiplied to create the total loss factor used in Equations 2.39 and 2.40. [16]

$$F = F_{hub}.F_{tip} \tag{2.44}$$

III. Glauert Correction

Another limitation of the BEM theory is that when the induction factor is greater than about 0.4, the basic theory becomes invalid. This occurs with turbines operating at high tip speed ratios (e.g. constant speed turbine at low wind speeds), as the rotor enters what is known as the *turbulent wake state* ($a > 0.5$). According to momentum theory, this operating state result from some of the flow in the far wakes starts to propagate upstream, which is a violation of the basic assumptions of BEM theory. Physically, this flow reversal cannot occur, and what actually happens is more flow entrains from outside the wake and the turbulence increases. The flow behind the rotor slows down, but the thrust on the rotor disk continues to increase. To compensate for this effect, Glauert (1926) developed a correction to the rotor thrust coefficient based on experimental measurements of helicopter rotors with large induced velocities [16].

While this model was originally developed as a correction to the thrust coefficient of an entire rotor, it has also been used to correct the local coefficient of the individual blade elements when used with BEM theory. When the losses near the tip are high, the induced velocities are large; therefore, the possibility of a turbulent wake near the tips increases. Thus, for each element the total induced velocity calculation must use a combination of the tip-loss and Glauert corrections. Buhl (2004) derived a modification to the Glauert empirical relation that included the tip-loss correction as follows [16]:

$$C_T = \frac{8}{9} + \left(4F - \frac{40}{90}\right)a + \left(\frac{50}{9} - 3F\right)a^2 \tag{2.45}$$

And when for solving for a, we find the following expression:

$$a = \frac{18F - 20 - 3\sqrt{C_T(50 - 36F) + 12F(3F - 4)}}{36F - 50} \tag{2.46}$$

Key assumptions for BEM

- Wind is steady, and normal to the rotor plane.
- A radial element of the blade is not affected by other close-by elements.
- C_L, C_D and C_M data are used from static measurements for different angle of attacks.

Now that all of the equations for BEM theory have been established, we will identify the iteration procedure. This process was written using LabView, allowing a user friendly interface and rapid simulation results (fig 2.7). Annex A

1. Initial estimate of the axial induction factor

2. Inflow angle ϕ is small ($\sin\phi \approx \phi$)

3. Thrust coefficient for the element is calculated

4. The tip- and hub-loss corrections are calculated

5. Now, if $C_T > 0.96F$, the element is highly loaded and the modified Glauert correction will be used to determine the new axial induction factor

6. If $C_T \leq 0.96F$, the standard BEM theory is used to calculate the axial induction

7. The tangential induction factor is found

8. This process is then repeated for each element, starting again and iterated until the values of induction factors and inflow angle reach convergence.
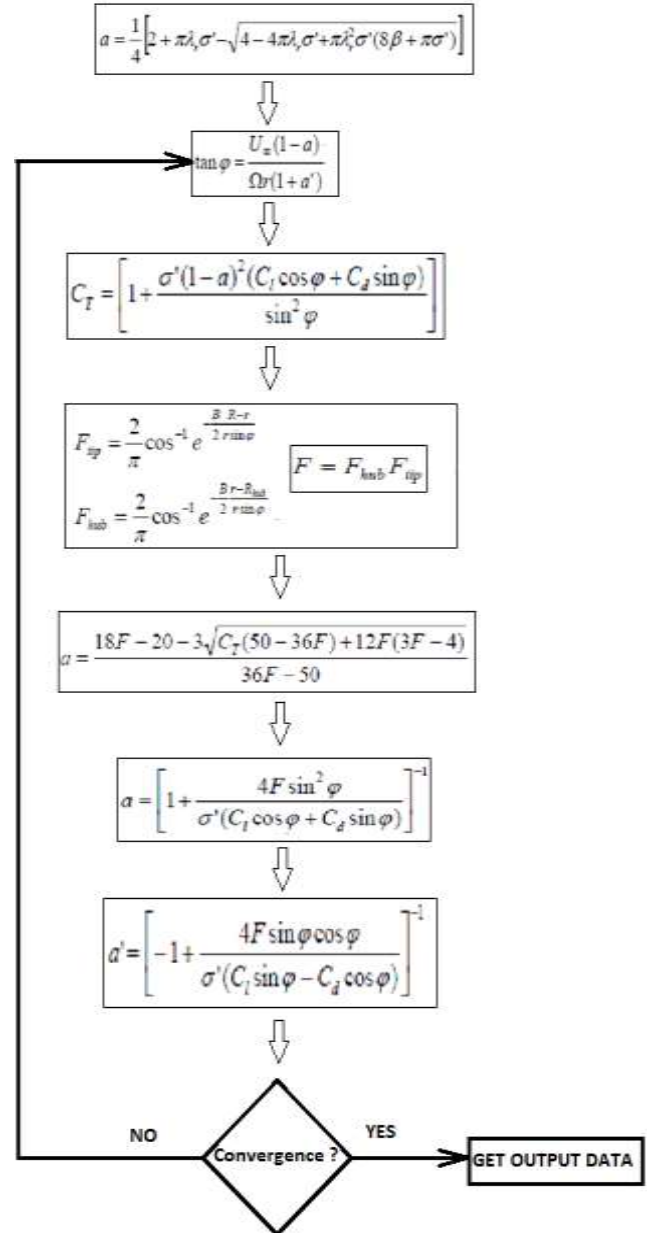
Figure 2.7: Flowchart BEM code

CHAPTER III: STRUCTURAL MODELING

3.1 Blade Design

The cross section of the wind turbine blade is shown in figure 3.1 imported from a previous study from the Cornell University [2]. Throughout this thesis, we have kept constant the used geometry for all the composite materials allowing a comparative study of the static and fatigue behavior. In other words, it is not the purpose of this work to pursue an optimization of the profile but rather a comparison between different blade materials. The original outer surface and spar were prepared using aluminum with a

thickness of 0.2 m for the spar in [2].

A variable thickness for the outer surface was used, beginning with an initial thickness at the hub of 3cm varying along the blade length according to the following equation: 0.03 - 0.00048485*x, x being the blade radius measured in meters from the hub.
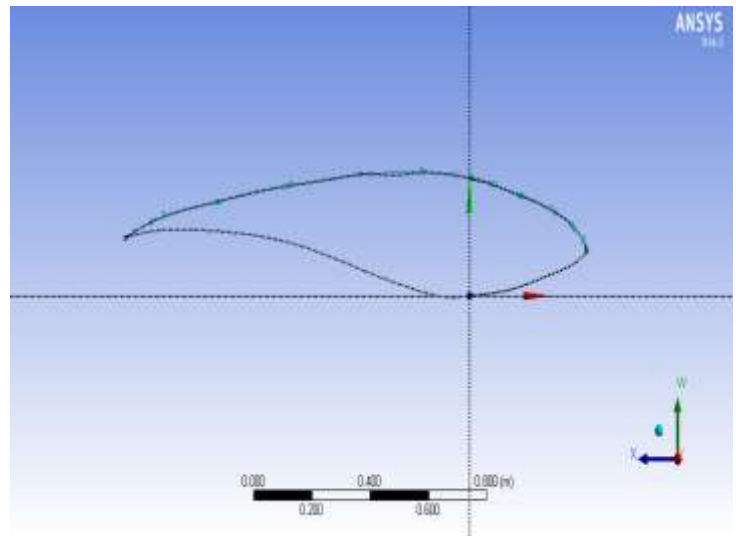
Figure 3.1: Cross section of the blade

The cross section of the wind turbine blade was assumed to be the same along the blade, with a NACA S821 airfoil and the corresponding aerodynamic coefficients such as the lift, drag and moment coefficients were imported from Xfoil [17].
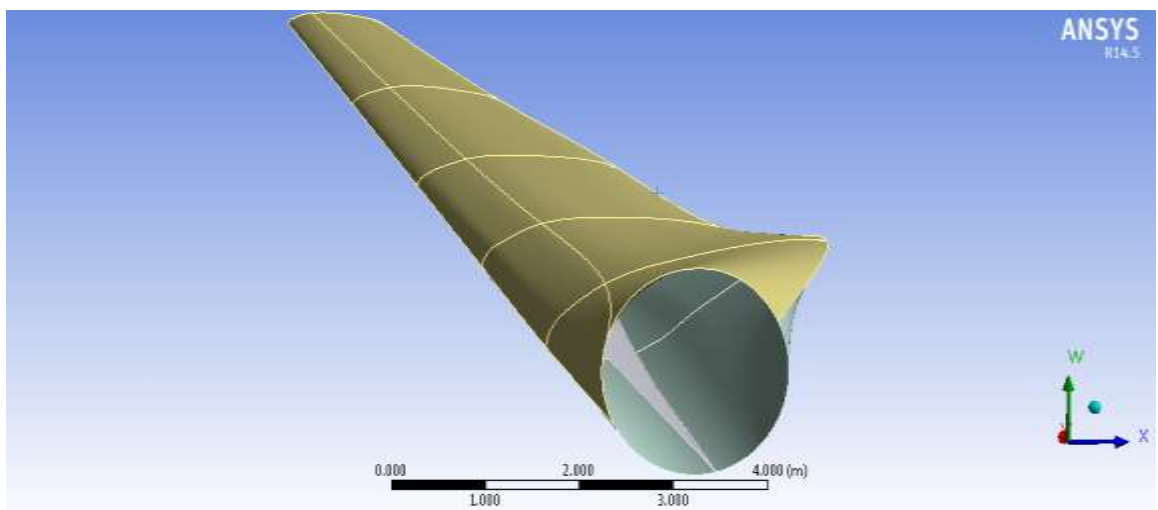
Figure 11.2: Geometry of the blade

3.2 Blade Model

To create the structural model of the blade, a finite element approach using the static structural workbench of ANSYS was used. A hexahedral element meshing with a 0.1 m size allowed the decomposition of the blade into 14770 nodes and 15103 elements. A zero total deformation at the hub was assumed as a constraint and hence the blade is assumed a cantilever beam attached to a rotating ring (see figure 3.3).
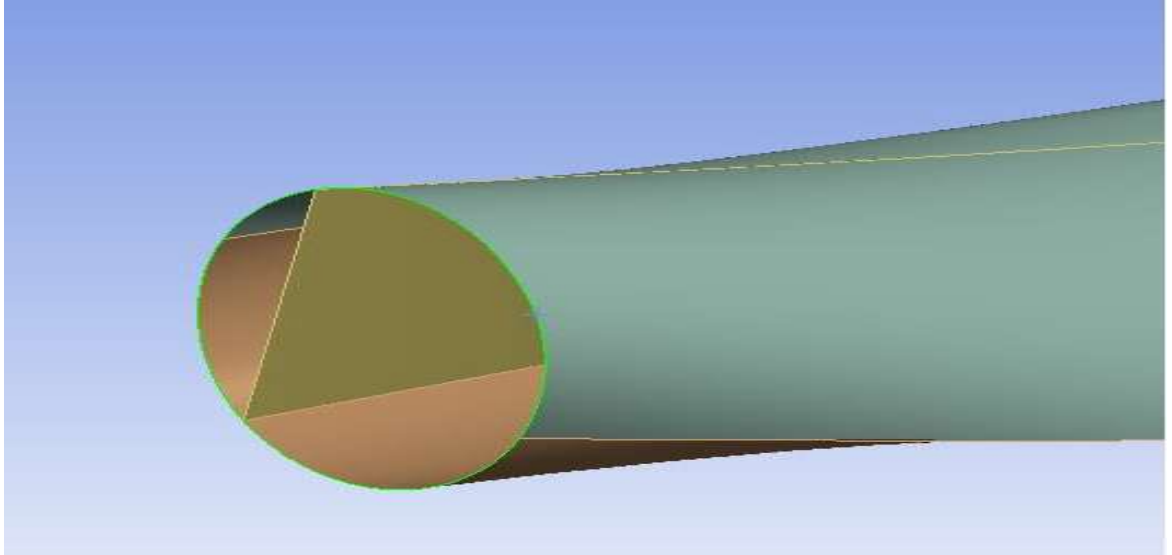
Figure 3.3: A zero total displacement constraint at the ring

3.3 Load Application

The BEM code only delivers 2-dimensional loads (lift, drag and aerodynamic moment) acting at the aerodynamic centre of a certain profile section. In [18] the comparison was made between the results of a FEM blade model loaded by a pressure distribution (pressure applied per element of the FE model) and a discrete sectional BEM loading. The concluding remarks stated that for detailed stress/strain analysis the pressure distribution delivers much better results. However, almost no difference was noted with regard to the general deflections [5].
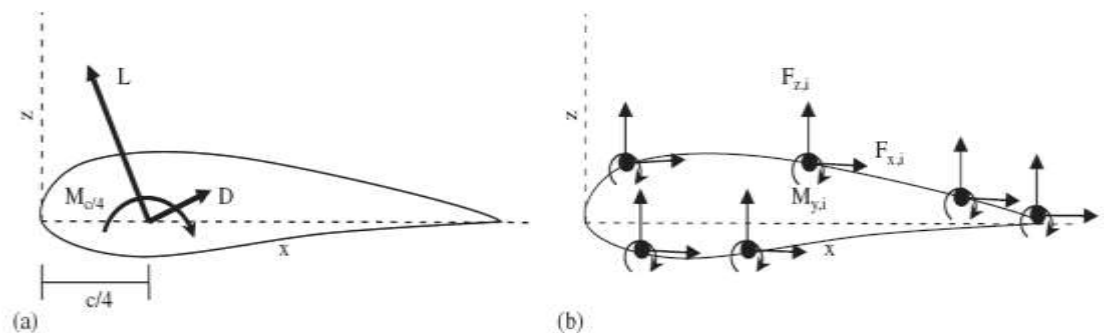
Figure 3.12: Actual and discretized system of BEM loading on profile [19]

In [19] all the nodal points of the selected profile are loaded, based on the actual and known pressure distribution, as can be seen in figure 3.4. The approach discretizes the pressure distributions over the available nodes of the profile section, in which the original 2D lift and drag forces remain equal to the summed discretized ones. The resultant aerodynamic moment is not necessary the same in both cases, so the difference is then distributed over the available nodes in order to assure a correct loading.

3.3.1 Chord Length, Aerodynamic Centre and Twist Angle

In ANSYS, the section parameters, chord length and twist angle, are calculated based on coordinates of the leading and trailing edge of specific section (see figure 3.5)
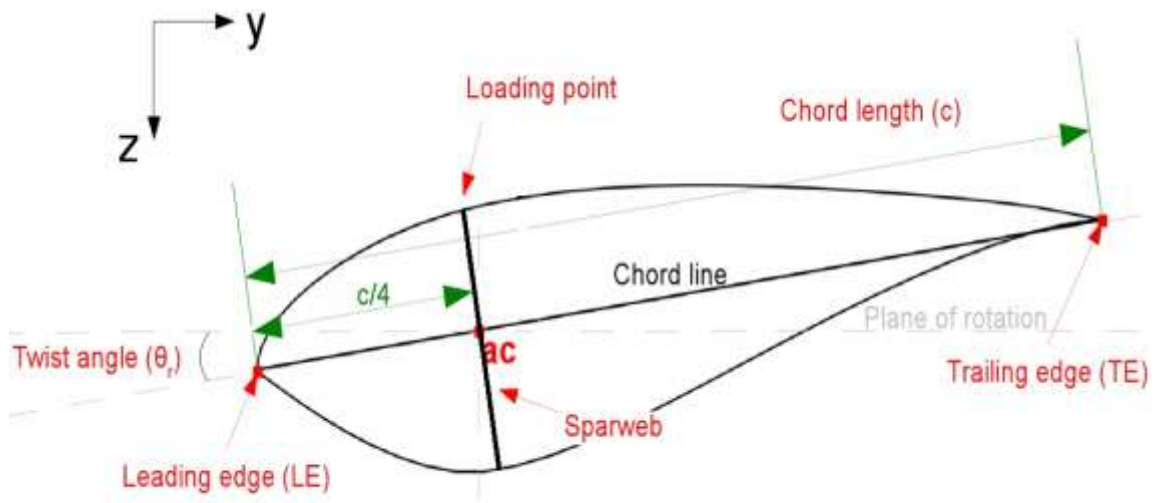
Figure 3.13: Determining aerodynamic centre, chord length and twist angle for the ANSYS model

3.3.2 Load Application and Moment Correction

Since the aerodynamic centre is not a real loading point in the ANSYS model (hollow blade section), the following translating strategy is considered in the program:

- One loading point per section (above the sparweb) for the axial and tangential forces. Since the aerodynamic forces are now translated from the aerodynamic centre to the loading point, a correction moment has to be applied in order compensate for the changed aerodynamic moment around the aerodynamic centre (see figure 3.6). The correction moment is then defined as:

$$M_{corr} = (F_{ax}.\Delta y - F_{tan}.\Delta z) * (-1) \qquad (3.1)$$
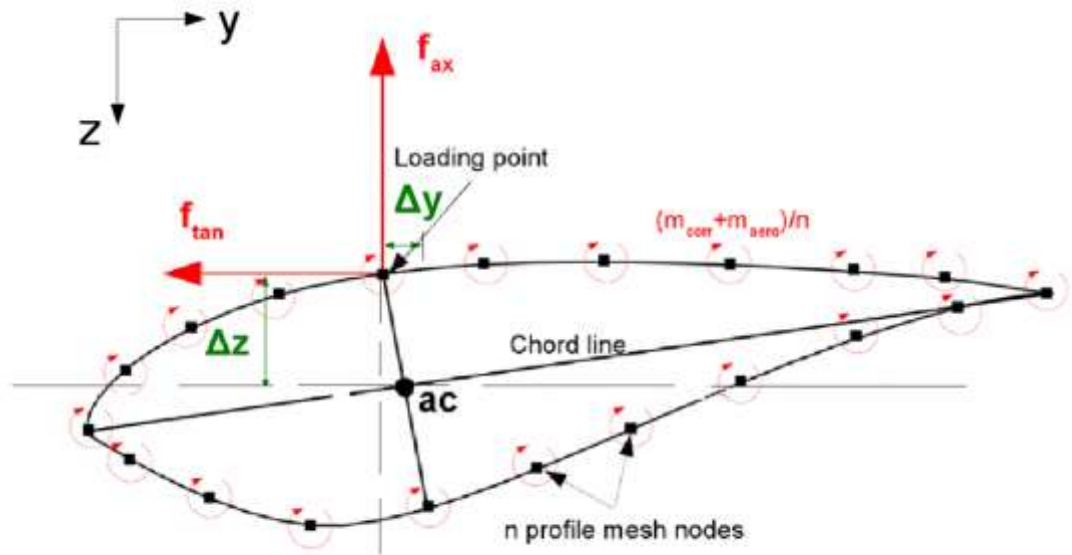
Figure 3.14: Aerodynamic loading in ANSYS (loading point) and its relation with the aerodynamic centre

Where the aerodynamic moment per unit of length is defined as:

$$m_{aero} = 1/2\rho V_{res}^2 c^2 C_m \quad [N] \tag{3.2}$$

With C_m being the coefficient of moment also available that is function of the angle of attack.

- The aerodynamic moment is in both cases distributed over all available section nodes. The correction moment is added to the aerodynamic moment and distributed over all section nodes. The aerodynamic moment is defined positive in the pitch up direction, which coincides with the positive moment direction around the spanwise x-axis in the ANSYS model. The calculated moments are shown in Table 3.1.

	dy	*dz*	*f_{ax}*	*f_{az}*	*m_{aero}*	*m_{corr}*	*m*
radius 1	0.1195	0.352	22048	2262	1130	-1838.51	-177.128
radius 2	0.0384	0.3269	-22453	-2052	6996	191.3964	1796.849
radius 3	0.01322	0.2086	-30305	-2208	6439	-59.9567	1594.761
radius 4	0.0005	0.15717	-70883	-3621	7013	-533.671	1619.832

F

Table 3.1: Calculated aerodynamic moment for respective blade cross section

Figure 3.7 illustrates the correct aerodynamic loadings of the blade including both moments and the forces (tangential and normal) for 4 distinct blade cross sections. This approach allowed for a better modeling of the aerodynamic forces giving a more rational stress distribution.
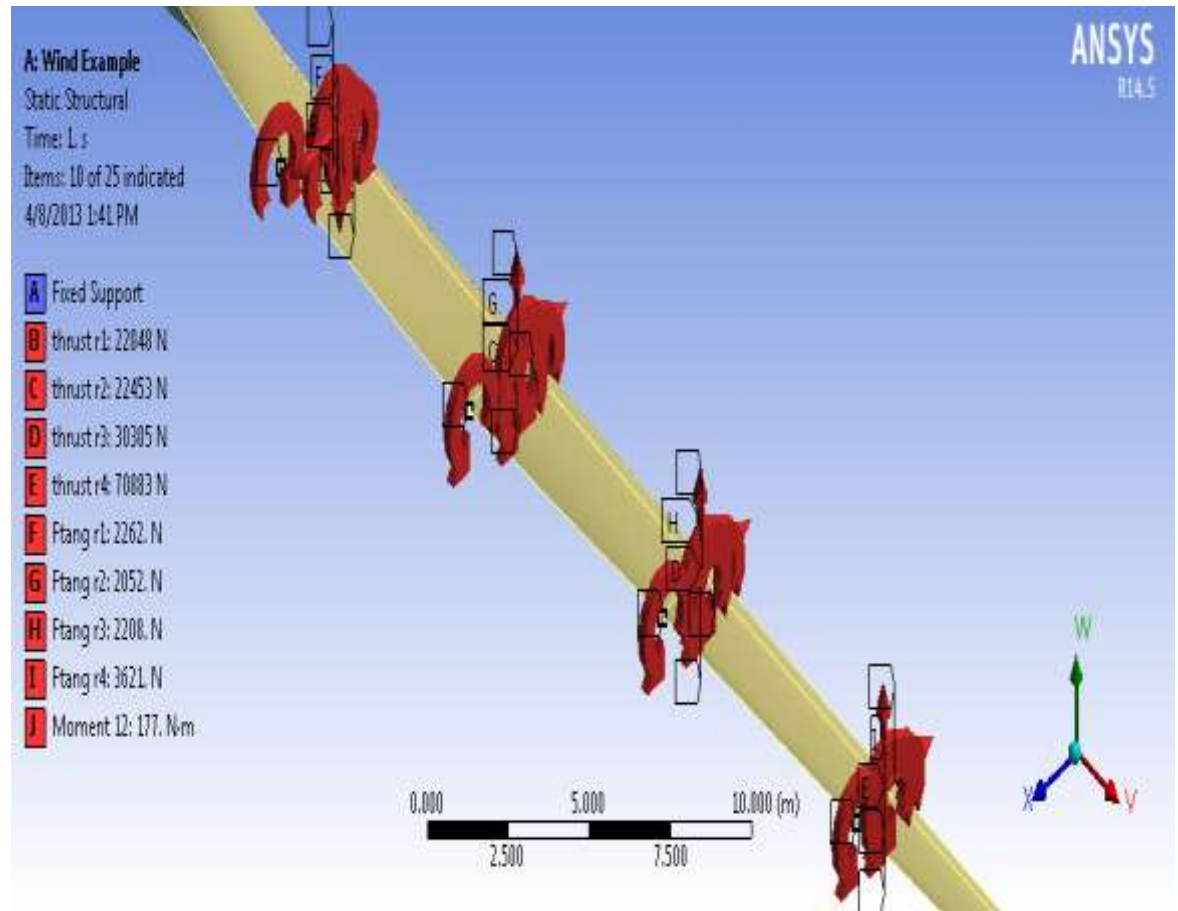
Figure 3.15: Modeling of the aerodynamic loads

3.4 Material Elastic Properties

The aerodynamic modeling is quite rapid and does not require much computational effort. On the other hand, material definition requires much work and is still a major field of research. For instance, the innovations and developments in the field of material science in general and in composite materials specifically since a quarter century ago are extraordinary.

Many types of materials are used in wind turbines. Two of the most important of these are steel and composites. The composites are typically comprised of fiberglass or wood together with a matrix of polyester or epoxy. Other common materials include copper and concrete [20].

Composites are materials comprising at least two dissimilar materials, most commonly fibers held in place by a binder matrix. Composites used in wind turbine applications include those based on fiberglass, carbon fiber, and wood. The main advantage of composites is that they have a high strength and high stiffness to weight ratio. They are also corrosion resistant, are electrical insulators, and lend themselves to a variety of fabrication methods [20].

It is not the interest of this thesis to define the optimum composite structure that will have the best cost to performance ratio or cost to endurance ratio but rather to perform a comparative study for defined composite materials. With the help of Hallal [3] [25], analysis of six previously derived composites was performed in a way to match a density of 1450 kg/m^3 and having a fiber content v_f = 40 % (see Table 3.2 and Table 3.3). Table 3.3 lists the orthotropic properties

Material	E_1 (GPa)	E_2 (GPa)	G_{12} (GPa)	v_{12}	v_{23}	X+ (MPa)	X- (MPa)	S (MPa)
T300J carbon	230	14	23	0.23	0.3	3530	2617	
RTM6	2.89	2.89	1.07	0.35	0.35	75	160	50

Table 3.2: Fiber and matrix properties

Composites	Ex (GPa)	Ey (GPa)	Ez (GPa)	Nuxy	Nuxz	Nuyz	Gxy (GPa)	Gxz (GPa)	Gyz (GPa)
Interlock-71	56.94	39.03	9.51	0.057	0.389	0.349	4.33	4.22	3.54
Interlock-H2	35.25	68.97	11.63	0.043	0.349	0.337	5.93	5.34	5.16
LTL1	53.98	67.54	8.34	0.031	0.342	0.345	4.16	3.65	3.51
[0,90]	49.99	49.99	6.39	0.035	0.362	0.362	2.69	2.43	2.43
[0,90,0]	64.70	35.27	6.37	0.05	0.36	0.35	2.69	2.52	2.34
[90,0,90]	35.27	64.70	6.37	0.027	0.35	0.36	2.69	2.34	2.52
Br35	45.9	6.93	5.55	1.03	0.12	0.202	9.9	2.68	2.36
Br45a	31.8	14.669	6.25	0.74	0.11	0.239	15.7	2.50	2.37
Br60	23.5	31.8	6.24	0.31	0.24	0.245	12.5	2.38	2.50

Table 3.3: Composite Elastic Properties

Now that we have derived the materials properties, it is possible to conduct our finite element analysis. In the solution toolbar in the static structural workbench, ANSYS allows the display of the total deformation showing the rigidity and flexibility of the blade under static conditions (figure 3.8).

The general procedure of work that is repeated for each material type can be illustrated in figure 3.9.

Aerodynamic Loads (via BEM theory code)

Physical Parameters

Geometric Parameters

Thrust   Tangential Force   Torsion Moment

Static Structural Analysis

FEM

ANSYS

Structural/Elastic Properties
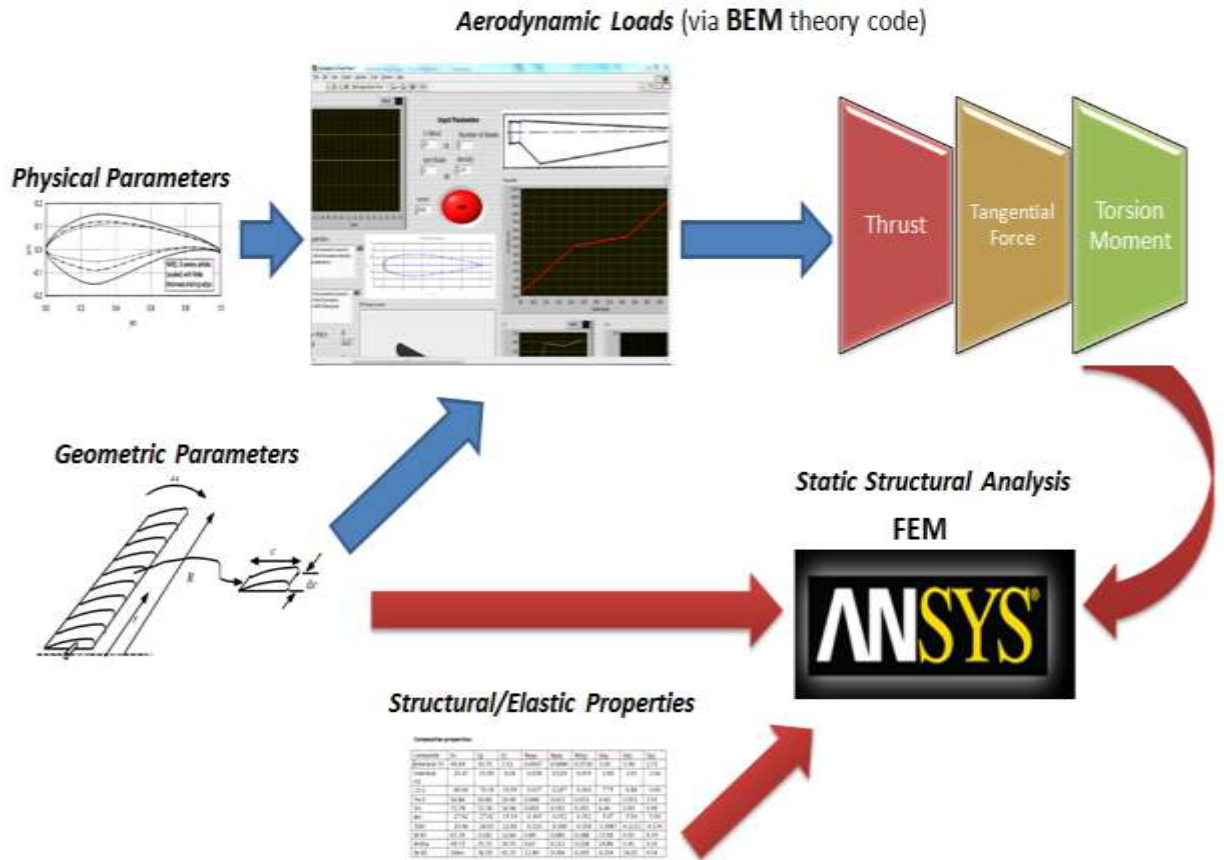
Figure 3.9 : The General work procedure

Type: Total Deformation
Unit: m
Time: 1
6/4/2013 1:40 PM

0.77485 Max
0.68875
0.60266
0.51656
0.43047
0.34438
0.25828
0.17219
0.086094
0 Min

0.000   5.000   10.000 (m)

2.500   7.500

Geometry \ Print Preview \ Report Preview /
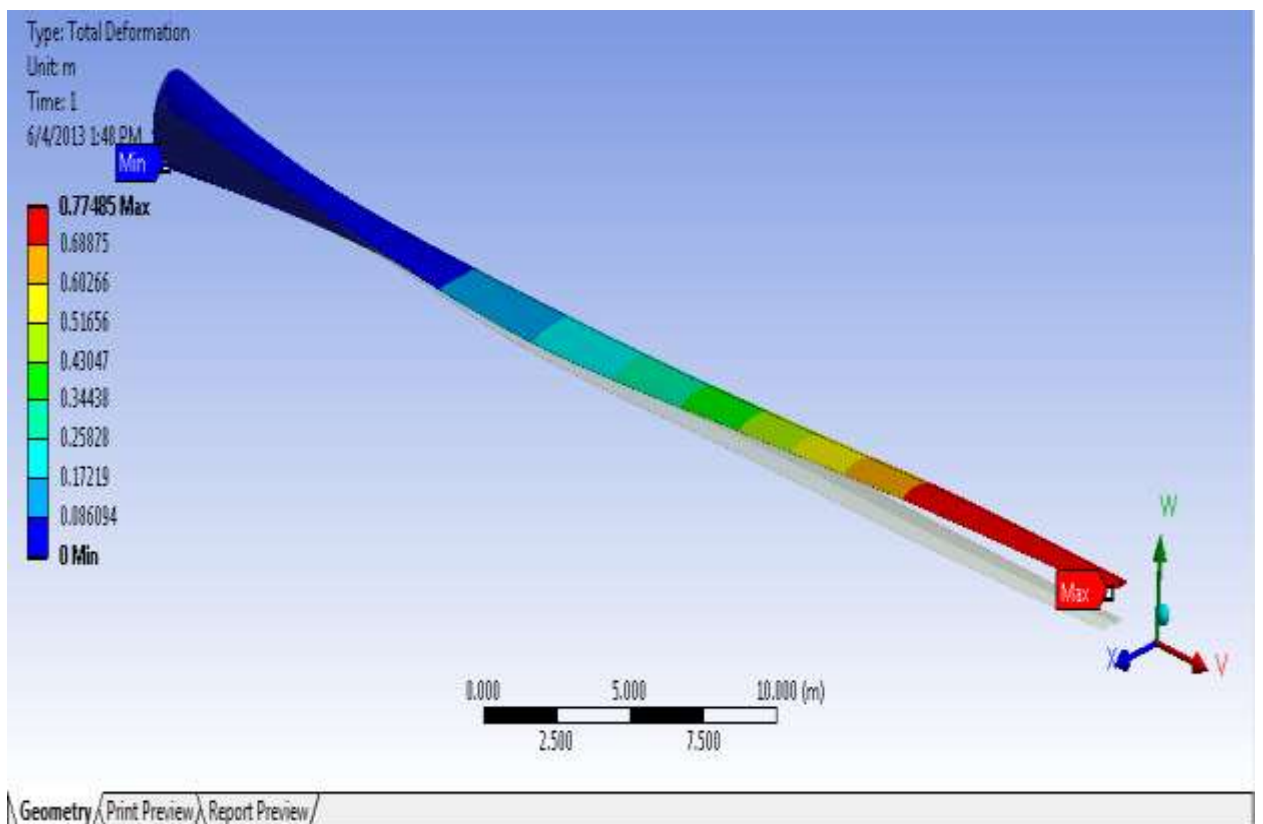
Figure 3.8: Total deformation for Interlock 71

3.5 Static Failure Criteria's

The failure criteria proposed to predict lamina failure could be divided in two main groups:

1. Failure criteria not associated with failure modes
2. Failure criteria associated with failure modes

The concern of this work is focused around the first category. This group includes all polynomial and tensorial criteria, using mathematical expressions to describe the failure surface as a function of the material strengths. Generally, these expressions are based on the process of adjusting an expression to a curve obtained by experimental tests. The most general polynomial failure criterion for composite materials is *Tensor Polynomial Criterion* proposed by Tsai and Wu [22]. This criterion may be expressed in tensor notation as [21]:

$$F_i \sigma_i + F_{ij} \sigma_i \sigma_j + F_{ijk} \sigma_i \sigma_j \sigma_k \geq 1 \qquad (3.3)$$

where i, j, k = 1, ... , 6 for a 3-D case. The parameters F_i, F_{ij} and F_{ijk} are related to the lamina strengths in the principal directions. For practical proposes, and due to the large number of material constants required, the third-order tensor F_{ijk} is usually neglected [23]. Therefore, the general polynomial criterion reduces to a general quadratic expression given by [21]:

$$F_i \sigma_i + F_{ij} \sigma_i \sigma_j \geq 1 \qquad (3.4)$$

where i, j = 1, ... , 6. Considering that the failure of the material is insensitive to a change of sign in shear stresses, all terms containing a shear stress to first power must vanish: $F_4 = F_5 = F_6 = 0$. Then, the explicit form of the general expression is:

$$F_1 \sigma_1 + F_2 \sigma_2 + F_3 \sigma_3 + 2F_{12} \sigma_1 \sigma_2 + 2F_{13} \sigma_1 \sigma_3 + 2F_{23} \sigma_2 \sigma_3 + F_{11} \sigma_1^2 + F_{22} \sigma_2^2 +$$
$$F_{33} \sigma_3^2 + F_{44} \sigma_4^2 + F_{55} \sigma_5^2 + F_{66} \sigma_6^2 \geq 1 \qquad (3.5)$$

After transferring the shear and normal stresses to an excel sheet, the static rupture criteria can be applied to each nodal element. In this thesis, two failure criteria were applied; Tsai- Hill and the Hoffman criteria's.

The criterion of Hill written in expression 3.6 is an interactive failure criterion. It is among the first to be applicable to anisotropic materials. It is a quadratic test, not taking into account the difference in the behavior of materials in tension and compression [24]. This criterion is very compatible in our case of study due to the absence of the elastic and strength properties in the compression mode.

$$(\frac{\sigma_L}{X})^2 + (\frac{\sigma_T}{Y})^2 + (\frac{\sigma_{T'}}{Z})^2 - \left(\frac{1}{X^2} + \frac{1}{Y^2} - \frac{1}{Z^2}\right)\sigma_L\sigma_T - \left(\frac{1}{X^2} + \frac{1}{Z^2} - \frac{1}{Y^2}\right)\sigma_L\sigma_{T'} - \left(\frac{1}{Y^2} + \frac{1}{Z^2} - \frac{1}{X^2}\right)\sigma_{T'}\sigma_T + (\frac{\sigma_{LT}}{S})^2 + (\frac{\sigma_{LT'}}{R})^2 + (\frac{\sigma_{TT'}}{Q})^2 = 1 \qquad (3.6)$$

The Hoffman criterion expressed by equation 3.7 generalizes the criterion of Tsai-Hill to take account of the difference between the tensile behavior and compression.

$$C_1(\sigma_T - \sigma_{T'})^2 + C_2(\sigma_{T'} - \sigma_L)^2 + C_3(\sigma_L - \sigma_T)^2 + C_4\sigma_L + C_5\sigma_T + C_6\sigma_{T'} + C_7\sigma_{TT'}^2 + C_8\sigma_{LT'}^2 + C_9\sigma_{LT}^2 = 1 \qquad (3.7)$$

C_i being characteristic constants that depend on the strength of the material. They can be expressed in expression 3.8, with + signifying the behavior in tension and − in compression.

$$C_1 = \frac{1}{2}\left[\frac{1}{Y^+Y^-} + \frac{1}{Z^+Z^-} - \frac{1}{X^+X^-}\right], \quad C_2 = \frac{1}{2}\left[\frac{1}{Z^+Z^-} + \frac{1}{X^+X^-} - \frac{1}{Y^+Y^-}\right], \quad C_3 = \frac{1}{2}\left[\frac{1}{X^+X^-} + \frac{1}{Y^+Y^-} - \frac{1}{Z^+Z^-}\right], \quad C_4 = \frac{1}{X^+} - \frac{1}{X^-}, \quad C_5 = \frac{1}{Y^+} - \frac{1}{Y^-}, \quad C_6 = \frac{1}{Z^+} - \frac{1}{Z^-}, \quad C_7 = \frac{1}{Q^2}, \quad C_8 = \frac{1}{R^2}, \quad C_9 = \frac{1}{S^2},$$
$$\qquad (3.8)$$

Since the analytical model used for the prediction of the elastic properties is only valid for tensional mode, an assumption that the compression and tension behaviors are the same was made. With the help of the work of Hallal [3] and [25], the strength properties in tension for the previously defined composites are described in Table 3.4

Composites	X (MPa)	Y (MPa)	Z (MPa)	S (MPa)	R (MPa)	Q (MPa)
Interlock-71	672*	238*	80	35	55	55
Interlock-H2	392*	478*	80	25	55	55
LTL1	848*	596*	80	195	55	55
[0,90]	600	600	70	45	45	40
[0,90,0]	820	390	70	45	45	40
[90,0,90]	390	820	70	45	45	40
Br30	500	90	75	135	50	50
Br45a	380	135	75	170	50	50
Br60	250	300	75	170	50	50

*values are experimental

Table 3.4: Strength properties for the composite materials

CHAPTER IV: RESULTS

In this chapter, the static failure results are presented by applying to each node (15103 in total) both Tsai-Hill and the Hoffman criteria's. This process is achieved by exporting the normal and shear forces from the ANSYS Workbench to an excel sheet. The corresponding $f(\sigma)$ is applied to each tensor of forces giving an entity that is smaller or larger than one, indicating the absence or presence of static rupture.

A graphical display of the excel sheet is traced, representing the percentage for each range of $f(\sigma)$ allowing for a much better comparative study between the textures and identifying possible rupture.

4.1 Static Failure: Interlock Textures

Three interlock textures were chosen for this study; interlock 71, interlock H2, LTL1. In the previous chapter, the corresponding strength and elastic properties were derived for tension mode. Simulation results for the interlock textures show an advantage for the interlock 71& LTL1 over the interlock H2, since possible rupture in the interlock H2 was observed (figure 4.1 - 4.4).

Hoffman vs. Hill : Interlock 71

	<0	0--0.001	0.001--0.005	0.005--0.02	0.02--0.08	0.08--1	1>
Hoffman	0.079454413	10.32907369	23.61120307	36.66159041	18.59895385	10.71972456	0
Hill	0.271469245	16.59935112	37.52896775	22.04197841	13.06362974	10.49460372	0
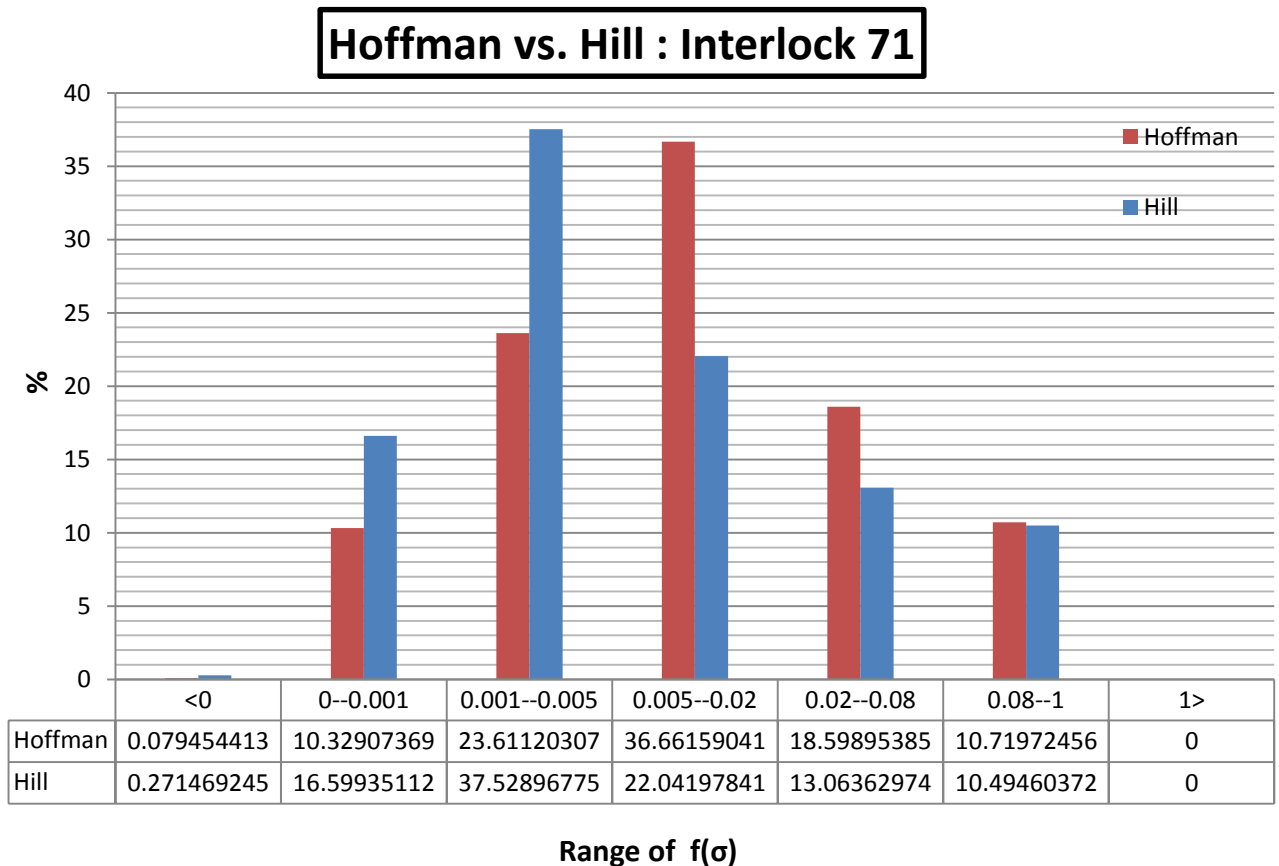
Range of f(σ)

Figure 4.1: Hoffman vs. Hill: Interlock 71

Hoffman vs. Hill : Interlock H2

Range of f(σ)	<0	0--0.001	0.001--0.005	0.005--0.02	0.02--0.08	0.08--1	>1
Hoffman	0.178772429	15.13606568	24.11441435	28.35198305	13.60656823	17.47997087	1.132225386
Tsai-Hill	0.099318016	16.4867907	25.67039661	25.92862345	13.20267497	17.41375886	1.198437397
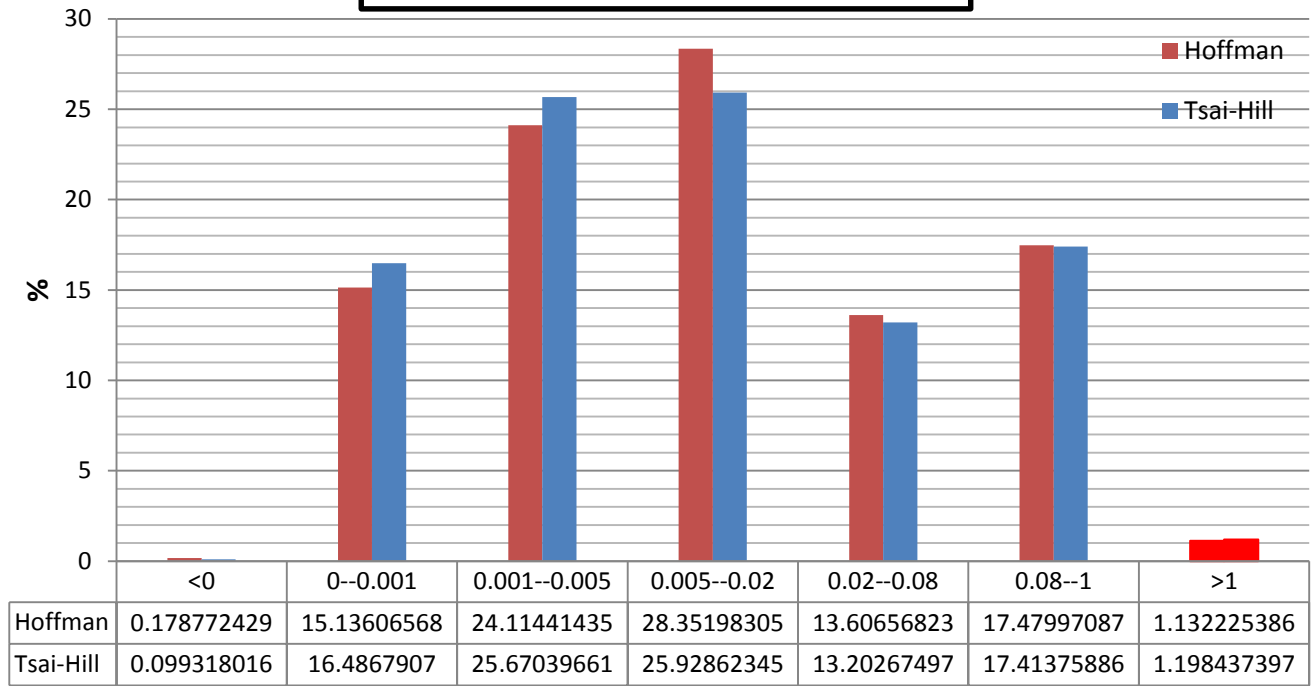
Figure 4.2: Hoffman vs. Hill: Interlock H2

Tsai Hill: Interlock 71 & Interlock H2

Range of f(σ)	<0	0--0.001	0.001--0.005	0.005--0.02	0.02--0.08	0.08--1	>1
Interlock 71	0.271469245	16.59935112	37.52896775	22.04197841	13.06362974	10.49460372	0
Interlock H2	0.099318016	16.4867907	25.67039661	25.92862345	13.20267497	17.41375886	1.198437397
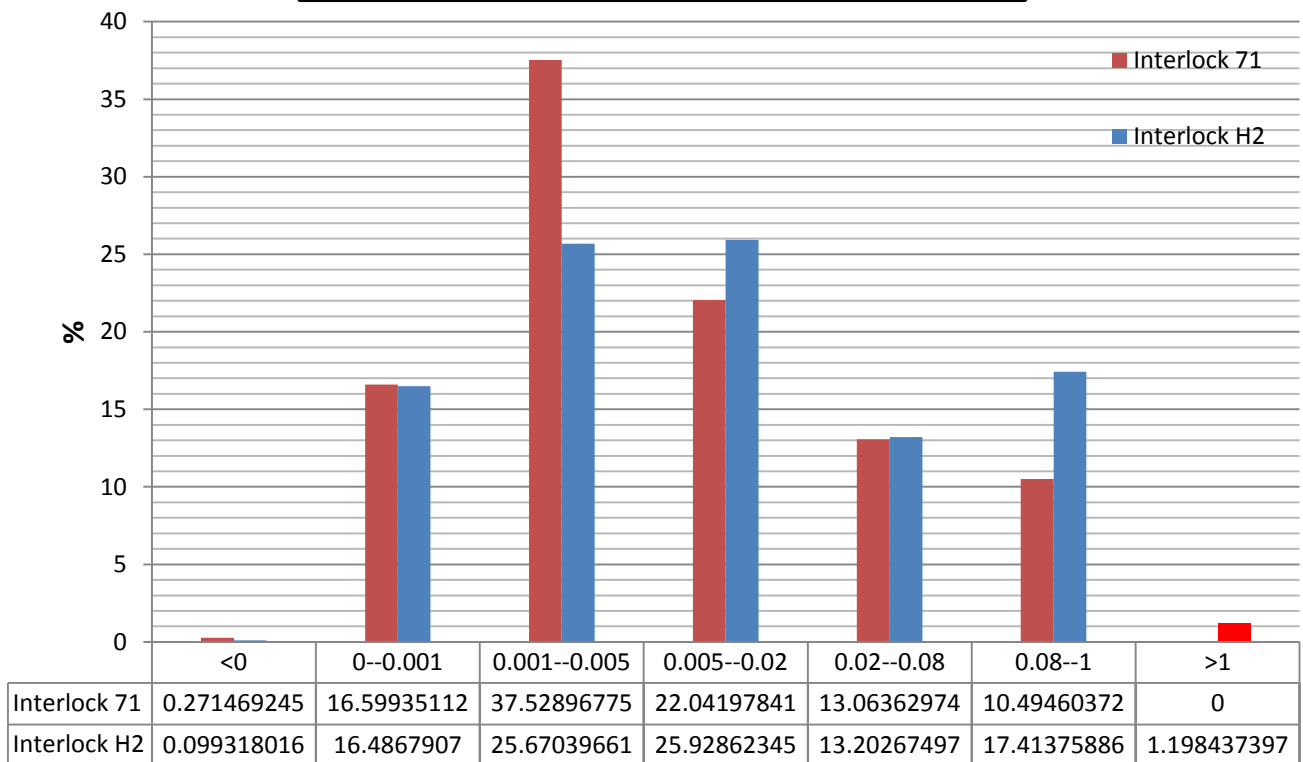
Figure 4.3: Comparison between interlock 71 & H2 under the Tsai Hill criteria
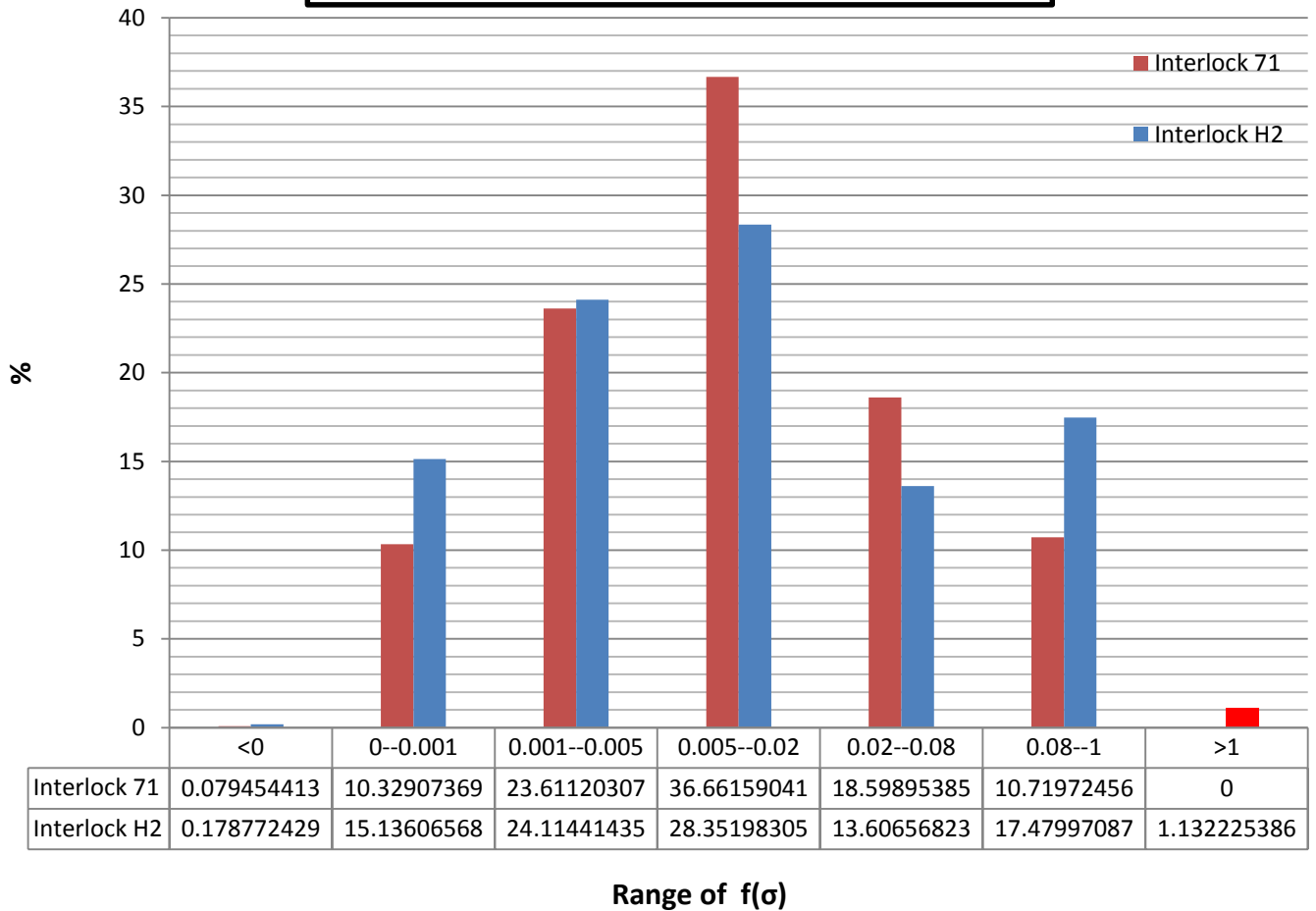
Figure 4.4: Comparison between interlock 71 & H2 under the Hoffman criteria

From Fig 4.3 and 4.4, the advantage in interlock 71 can be seen due to the presence of rupture in the interlock h2 texture (that is marked in red). Additional statistical study of the data justifies our conclusion for the interlock textures.

If we define χ as the average $f(\sigma)$ and ϑ as the corresponding standard deviation, we can interpret a comparative expression expressed by the ratio of the product $\beta = 1/ (\chi^* \vartheta)$. If the texture has a high safety factor, then it will have a fairly low average and standard deviation (near zero), hence β allows for further justification of the graphical interpretation. Defining β as the ratio of either the two is not significant in the purpose of this study since the interest is to identify a composite with a high safety factor (low average) and a superior confidence (low standard deviation)

Between the laminates and the interlock composite materials that were tested, it is the LTL1 that demonstrated the best performance. No static rupture was detected and the obtained value of β is the highest, meaning a greater safety factor.

Tsai Hill :LTL1

	<0	0--0.001	0.001--0.005	0.005--0.02	0.02--0.08	0.08--1	>1
Tsai Hill	0.450241674	42.21677812	40.47540224	12.46772164	4.217705092	0.172151228	0

Range of f(σ)
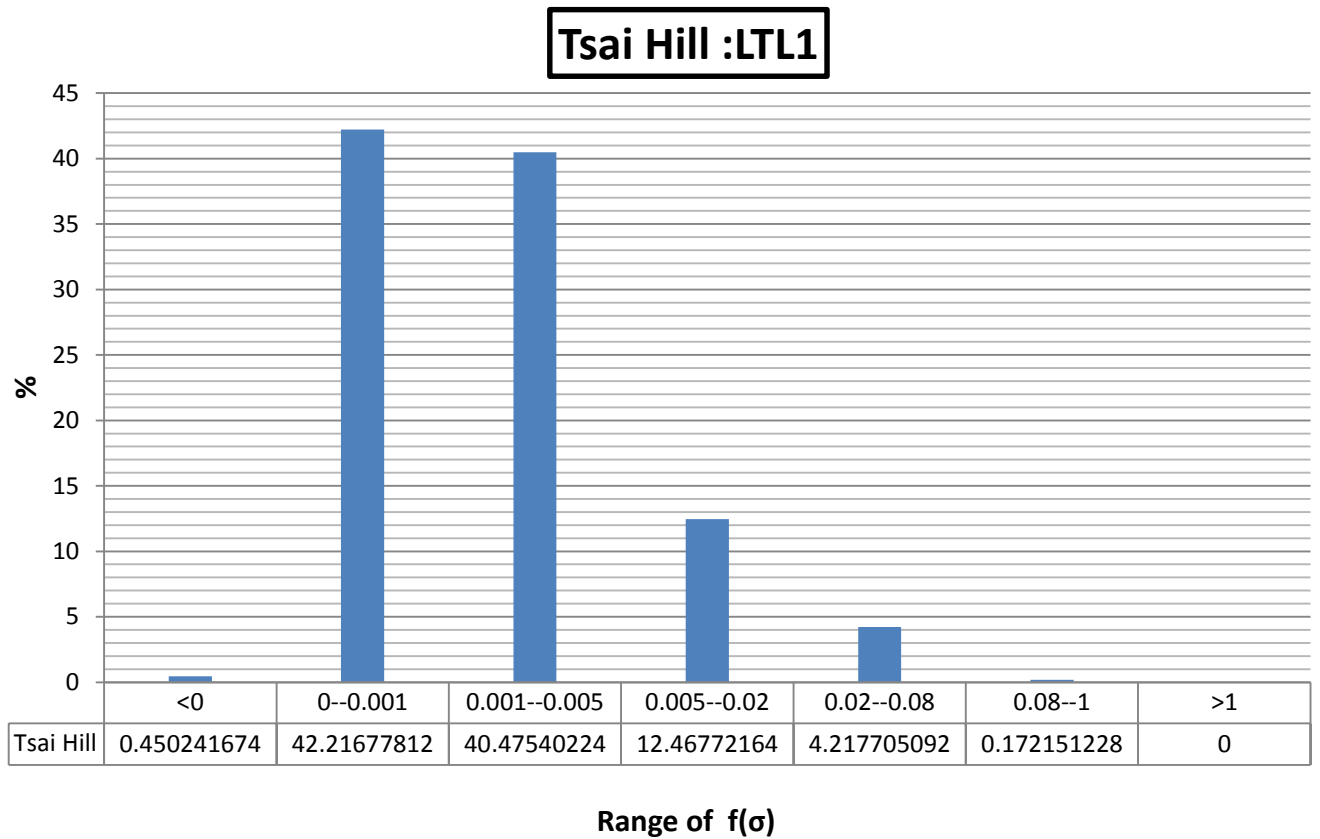
Figure 4.5: Tsai-Hill for LTL1

Hoffman: LTL1

	<0	0--0.001	0.001--0.005	0.005--0.02	0.02--0.08	0.08--1	>1
Hoffman	7.521684434	30.05363173	44.75269814	15.837913	1.834072701	0	0

Range of f(σ)
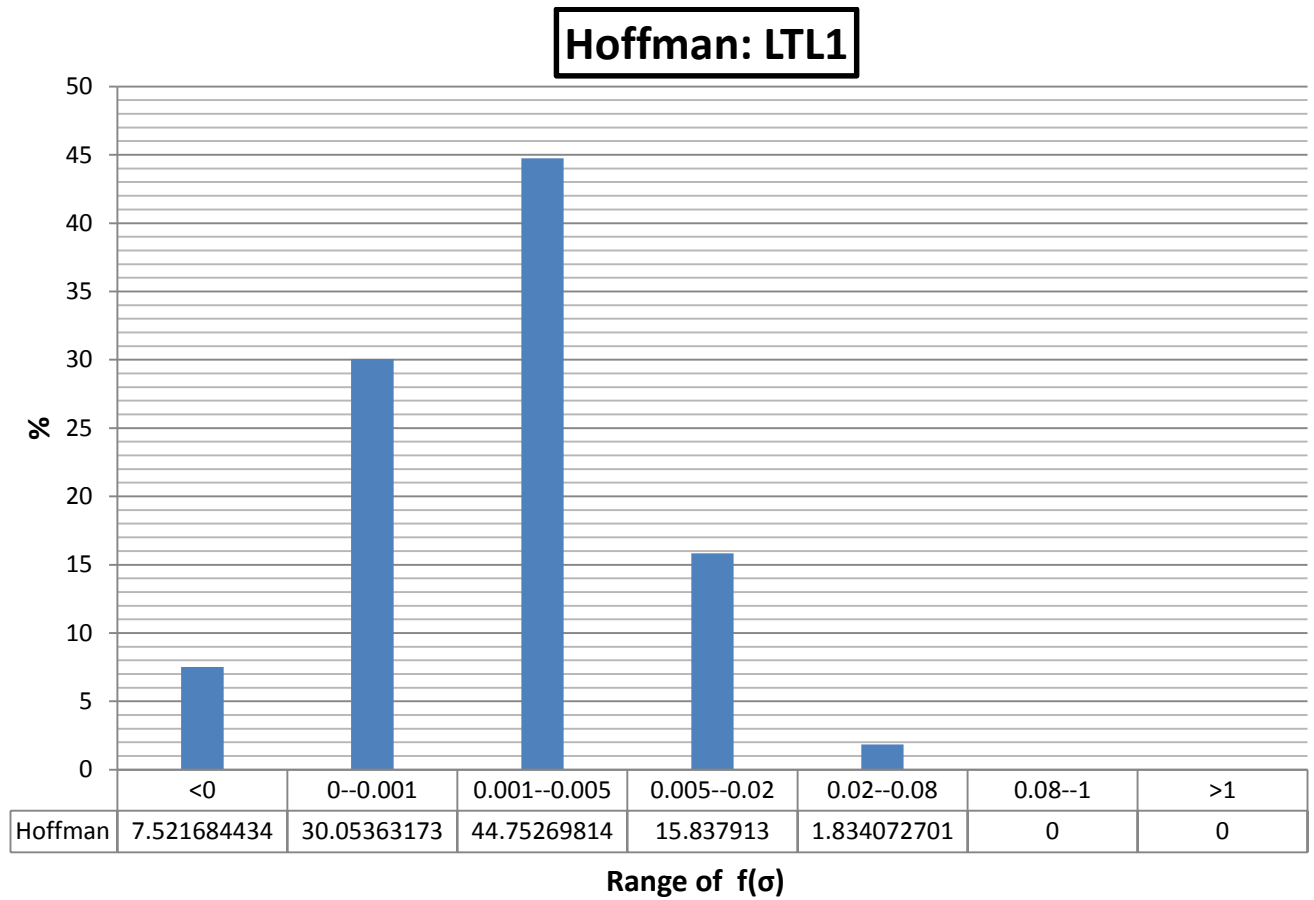
Figure 4.6: Hoffman for LTL1

Hoffman vs. Tsai-Hill : LTL1

	<0	0--0.001	0.001--0.005	0.005--0.02	0.02--0.08	0.08--1	>1
Hoffman	7.521684434	30.05363173	44.75269814	15.837913	1.834072701	0	0
Tsai-Hill	0.450241674	42.21677812	40.47540224	12.46772164	4.217705092	0.172151228	0

Range of f(σ)
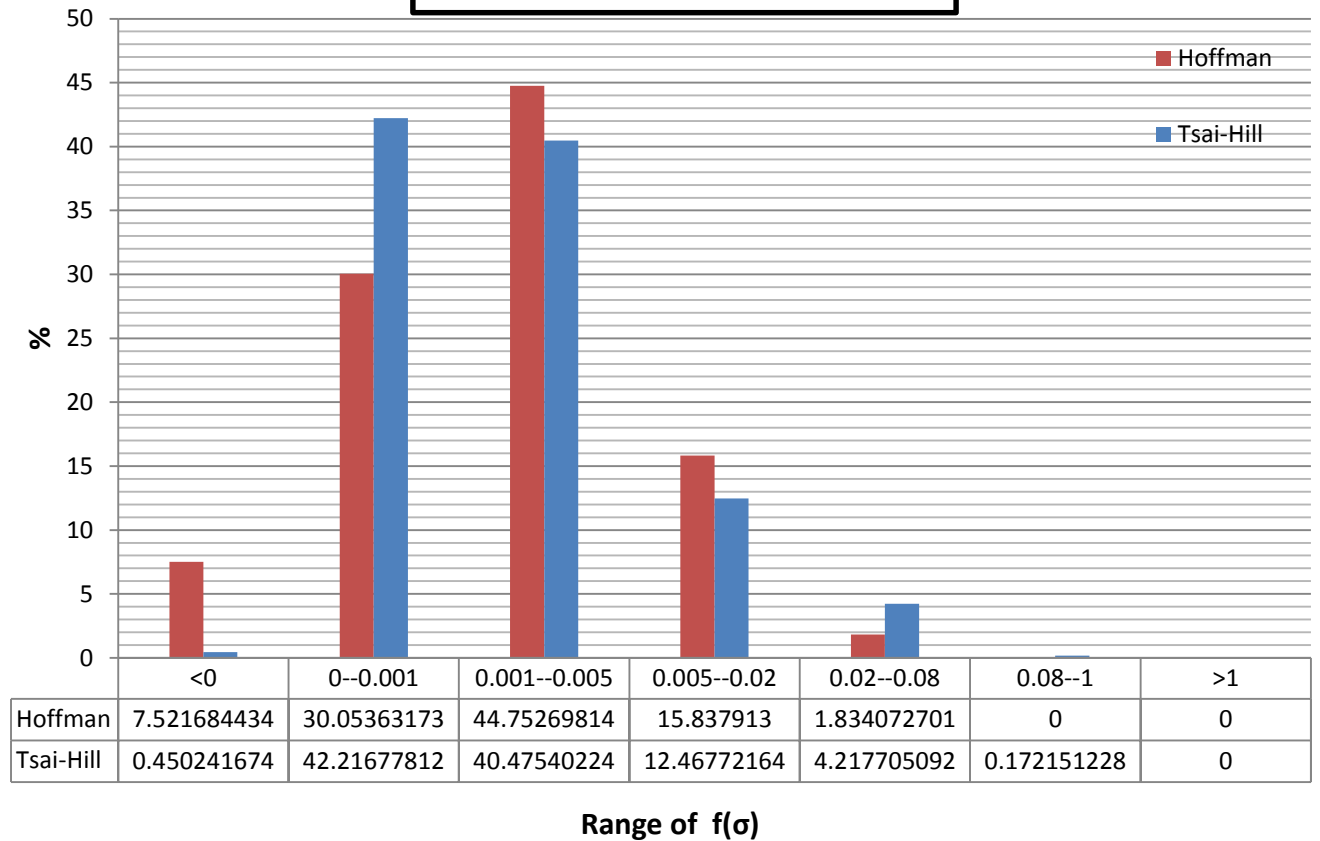
Figure 4.7: Comparison between Tsai Hill and Hoffman for LTL1

Interlock 71, Interlock H2, LTL1: Hoffman

	<0	0--0.001	0.001--0.005	0.005--0.02	0.02--0.08	0.08--1	>1
Interlock 71	0.079454413	10.32907369	23.61120307	36.66159041	18.59895385	10.71972456	0
Interlock H2	0.178772429	15.13606568	24.11441435	28.35198305	13.60656823	17.47997087	1.132225386
LTL1	7.521684434	30.05363173	44.75269814	15.837913	1.834072701	0	0

Range of f(σ)
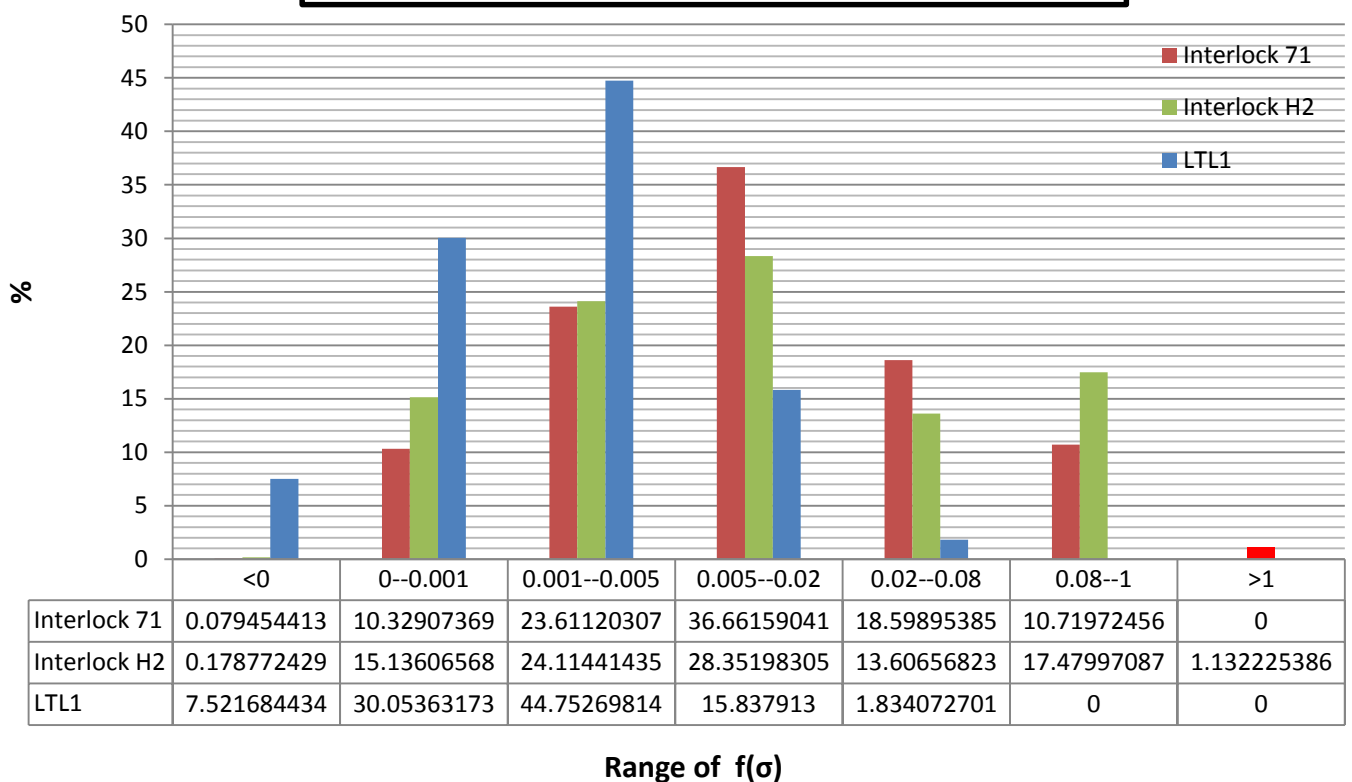
Figure 4.16: Comparison for the interlocks under the Hoffman criteria
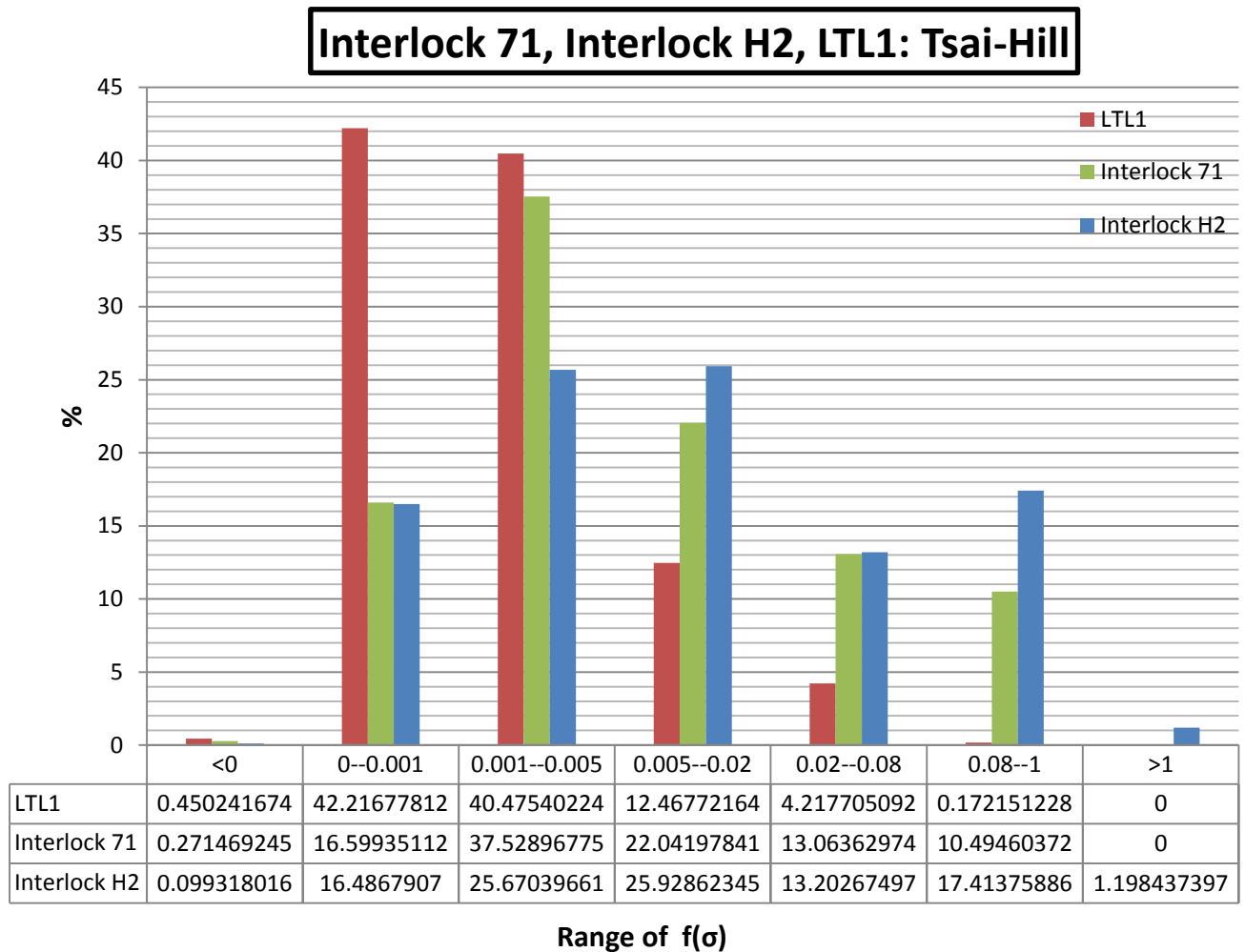
Figure 4.9: Comparison for the interlocks under the Tsai-Hill criteria

As for the statistical study that was performed on the interlock textures, the values for the LTL1, interlock 71 and interlock H2, as said are an additional tool that permit a comparison between the composite materials. As the graphs appear to show that in terms of behavior in static mode, the LTL1 is the most performing. Equally are the values of beta which demonstrate that the LTL1 possess the highest value, secondly followed by the interlock 71 and lastly the interlock H2 which indicated rupture.

LTL1	$\chi = 0.002813$	$\vartheta = 0.005525$	$\beta = \mathbf{64342.45}$
Interlock 71	$\chi = 0.032138$	$\vartheta = 0.06537$	$\beta = 475.99$
Interlock H2	$\chi = 0.082805$	$\vartheta = 0.207279$	$\beta = 58.26$

4.2 Static Failure: Orthogonal Laminates

Three orthogonal laminates were chosen for the purpose of this study: 0-90, 0-90-0 and 90-0-90 laminates. In theory, the behavior of the previously mentioned laminates should be similar, since only the order in which the laminate are distributed in varied but orthogonality is kept.

Tsai Hill : 0-90

	<0	0--0.001	0.001--0.005	0.005--0.02	0.02--0.08	0.08--1	>1
Tsai Hill	0.317817652	14.10977951	39.14454082	26.15374429	13.80520426	6.468913461	0

Range of f(σ)
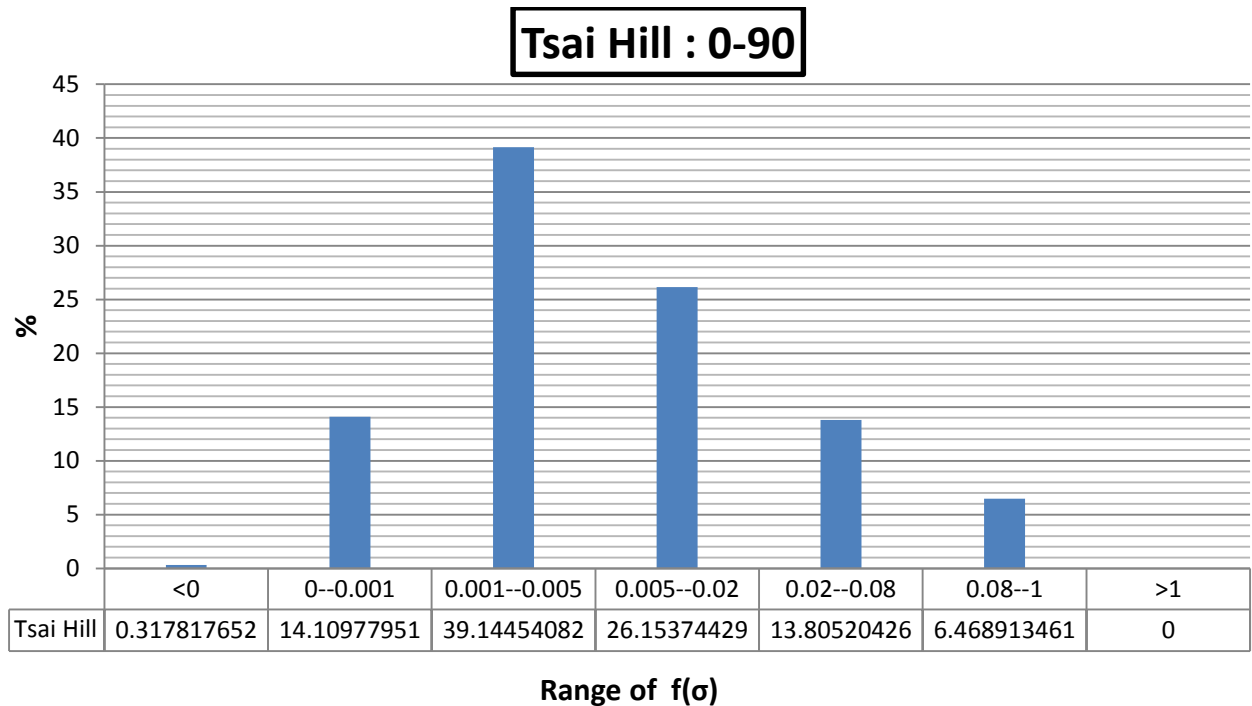
Figure 4.10: Tsai-Hill for the 0-90 laminate texture

Hoffman: 0-90

	<0	0--0.001	0.001--0.005	0.005--0.02	0.02--0.08	0.08--1	>1
Hoffman	1.032907369	12.99741773	33.88730716	31.78838641	15.32808051	4.965900814	0

Range of f(σ)
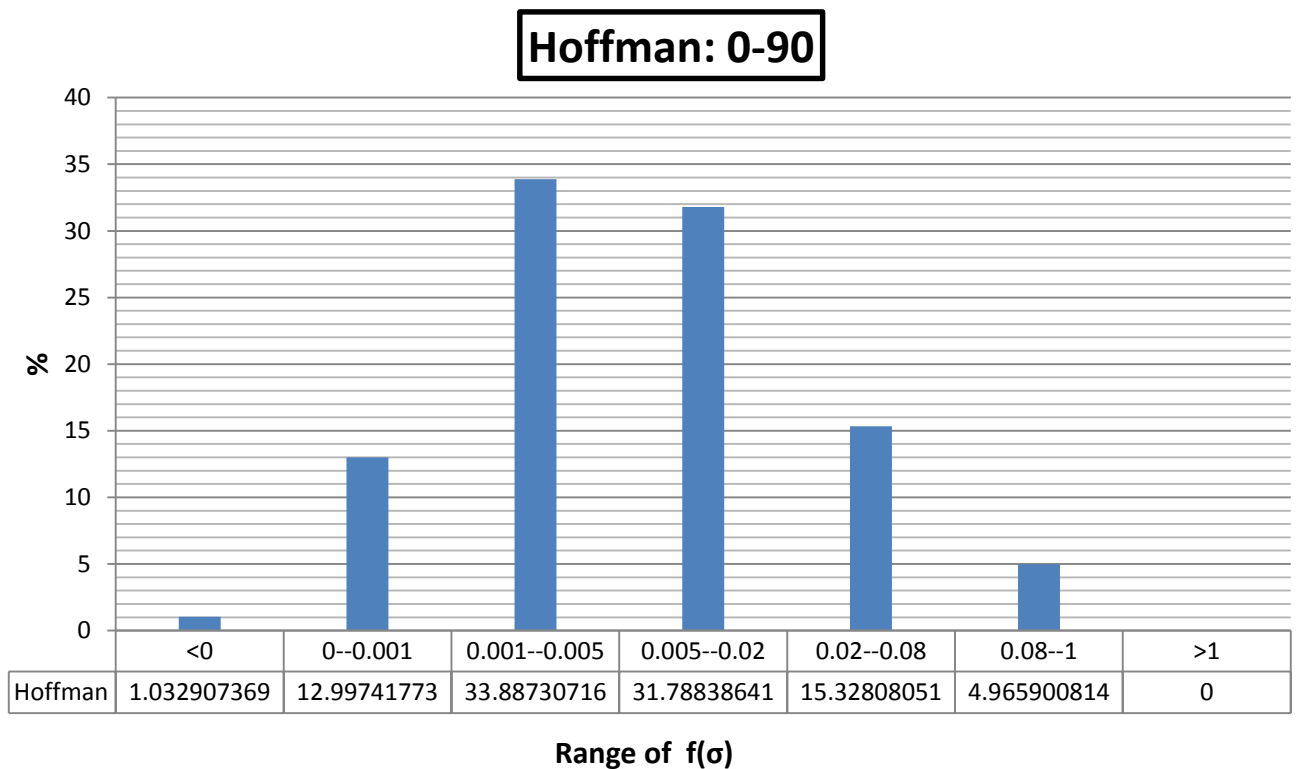
Figure 4.11: Hoffman for the 0-90 laminate texture

Tsai Hill vs. Hoffman : 0-90

	<0	0--0.001	0.001--0.005	0.005--0.02	0.02--0.08	0.08--1	>1
Hoffman	1.032907369	12.99741773	33.88730716	31.78838641	15.32808051	4.965900814	0
Tsai-Hill	0.317817652	14.10977951	39.14454082	26.15374429	13.80520426	6.468913461	0

Range of f(σ)
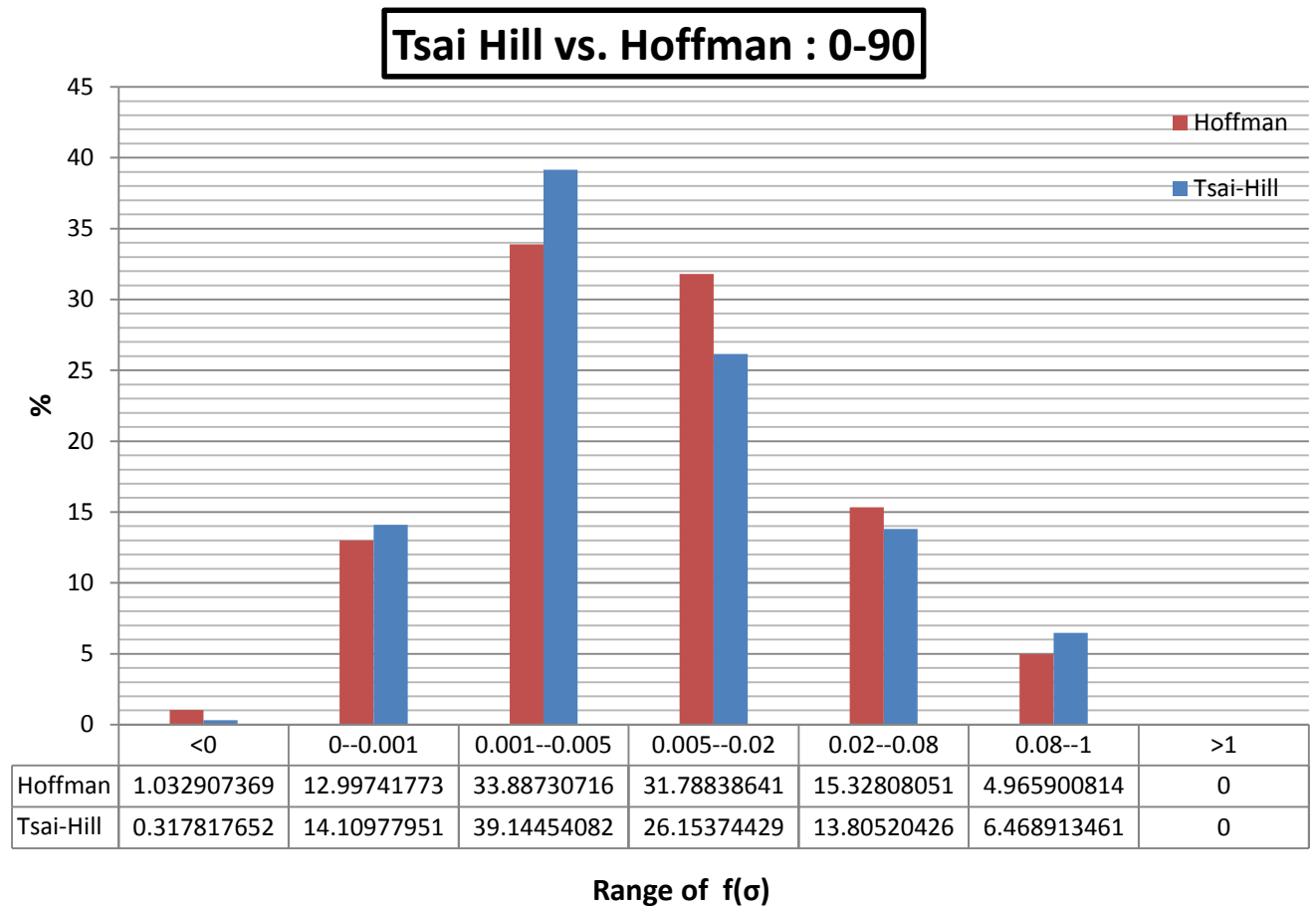
Figure 4.12: Comparison between Tsai-Hill and Hoffman criteria's for 0-90

Tsai Hill : 0-90-0

	<0	0--0.001	0.001--0.005	0.005--0.02	0.02--0.08	0.08--1	>1
Percentage	0.523074886	15.16917169	40.8461895	24.53817122	14.77852082	4.14487188	0
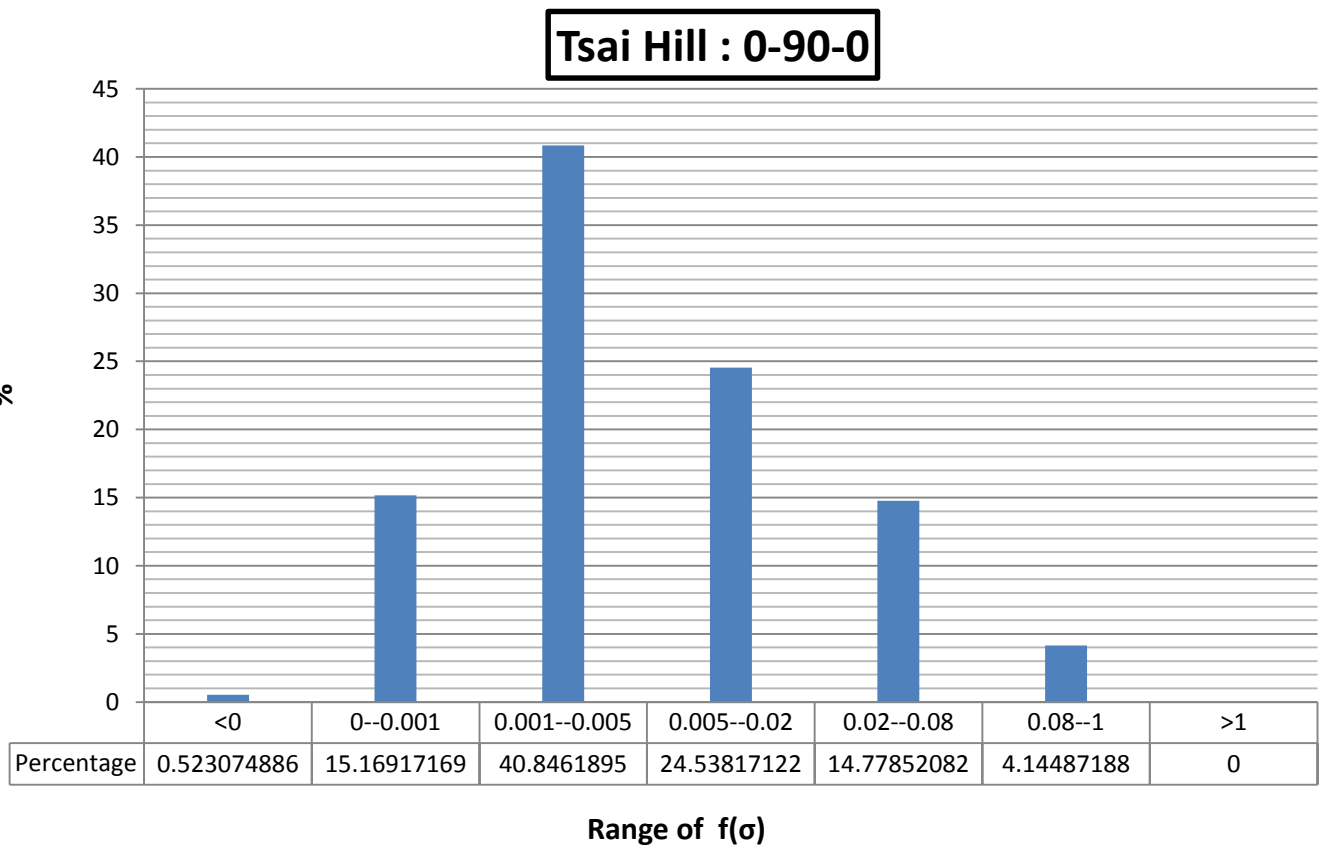
Range of f(σ)

Figure 4.13: Tsai-Hill for the 0-90-0 laminate texture

Hoffman: 0-90-0

	<0	0--0.001	0.001--0.005	0.005--0.02	0.02--0.08	0.08--1	>1
Percentage	0.576044494	10.85214858	28.14010461	38.4426935	19.22796795	2.761040853	0
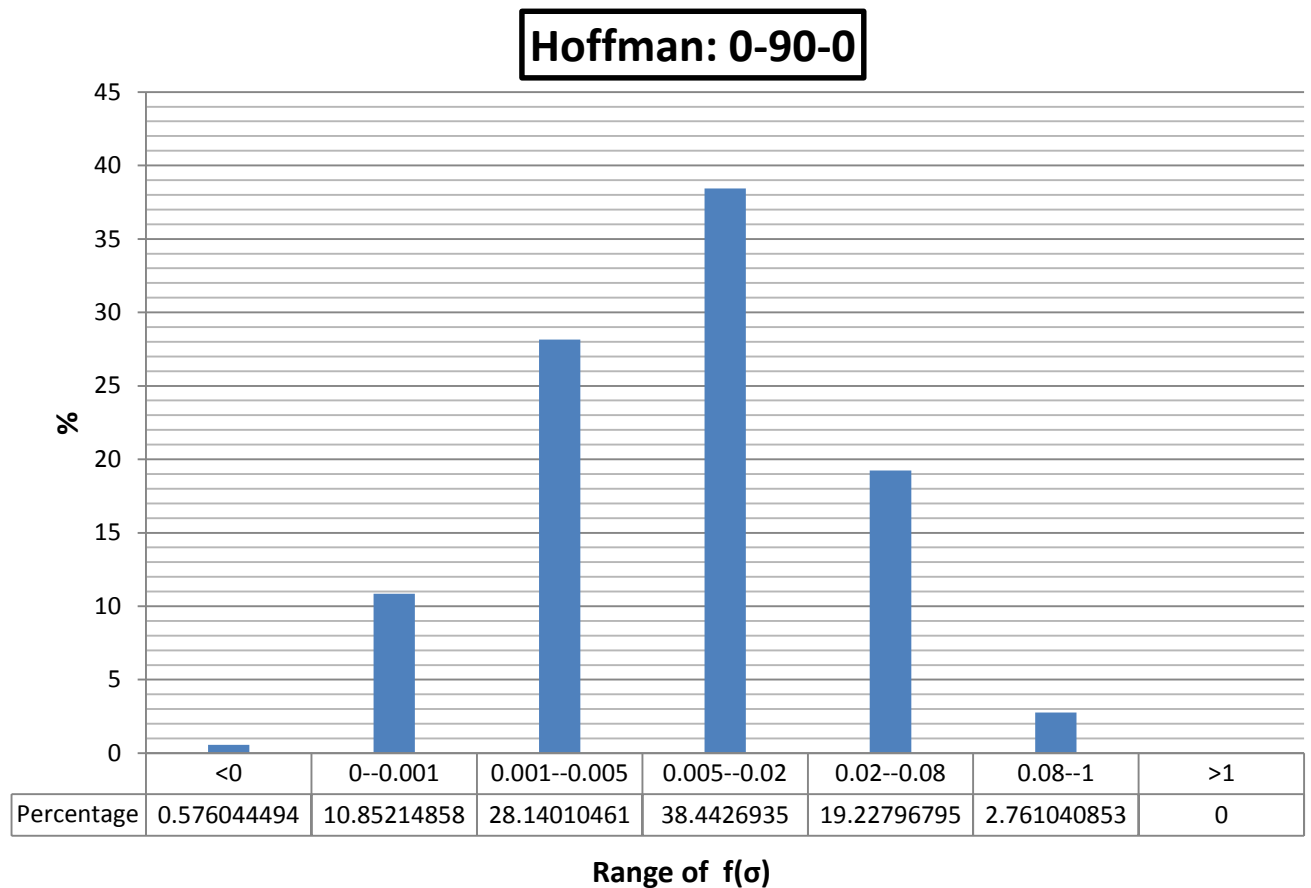
Range of f(σ)

Figure 4.14: Hoffman criteria for the 0-90-0 laminate texture

Tsai Hill vs. Hoffman : 0-90-0

	<0	0--0.001	0.001--0.005	0.005--0.02	0.02--0.08	0.08--1	>1
Hoffman	0.576044494	10.85214858	28.14010461	38.4426935	19.22796795	2.761040853	0
Tsai Hill	0.523074886	15.16917169	40.8461895	24.53817122	14.77852082	4.14487188	0
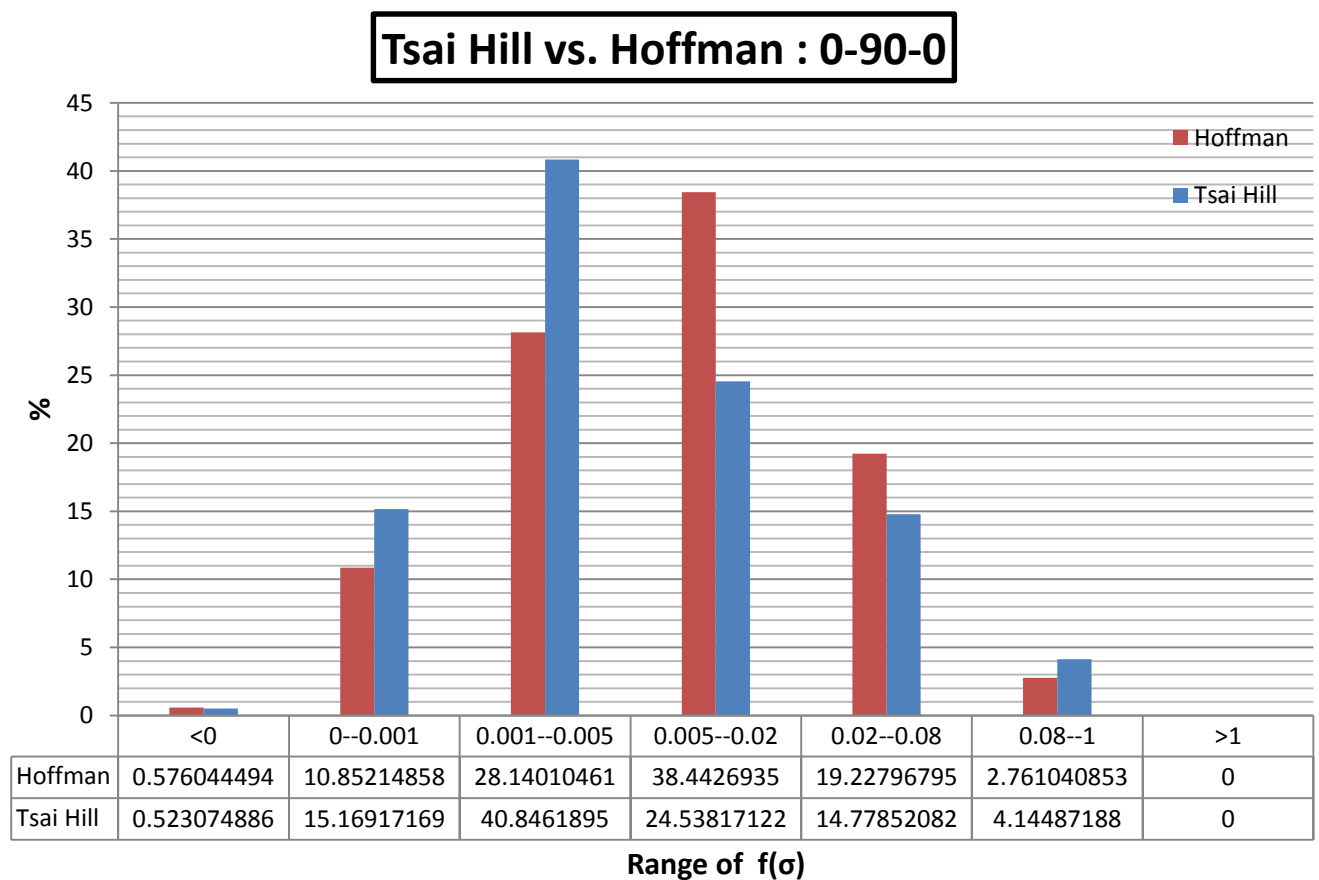
Range of f(σ)

Figure 4.15: Comparison between Tsai-Hill and Hoffman criteria for the 0-90-0 texture

Tsai Hill : 90-0-90

	<0	0--0.001	0.001--0.005	0.005--0.02	0.02--0.08	0.08--1	>1
Percentage	0.178772429	13.01066013	33.45030789	31.82811362	14.12302192	7.409124015	0
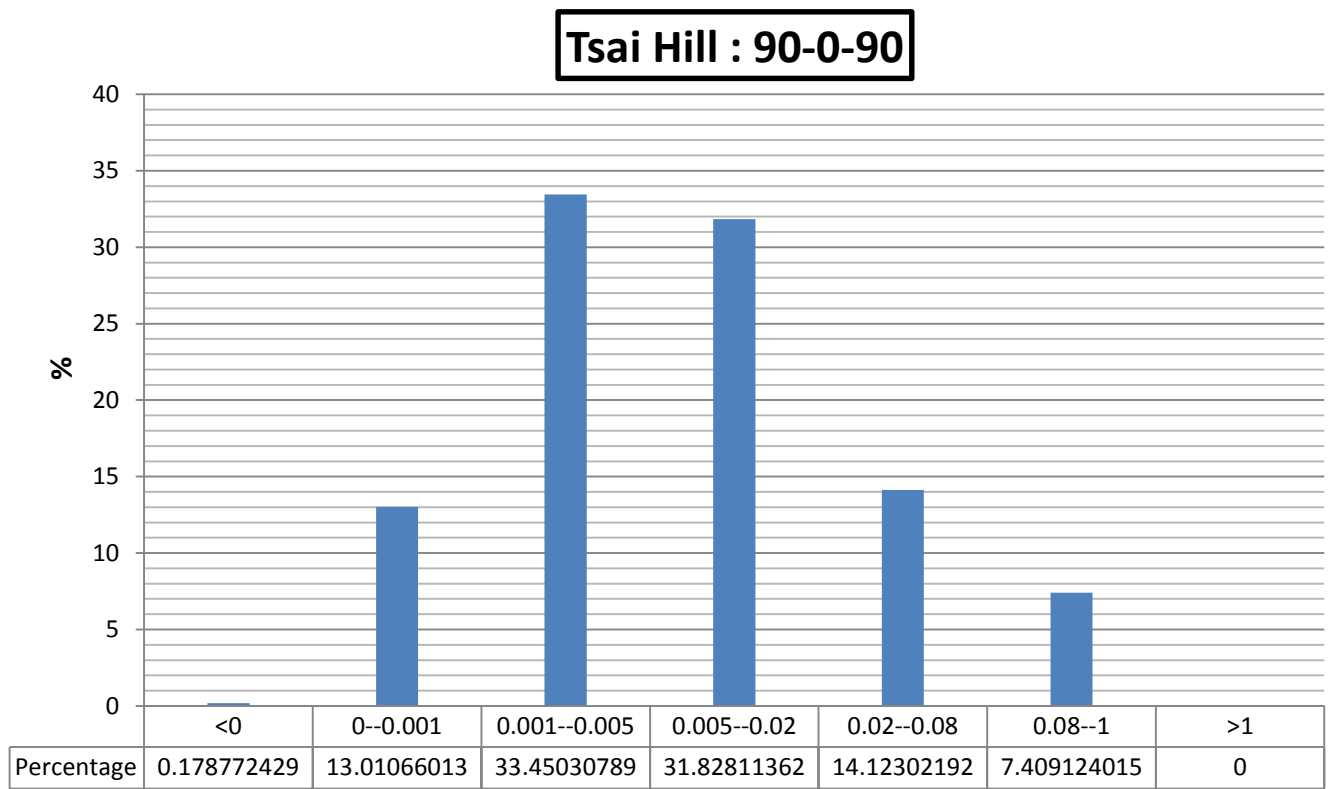
Range of f(σ)

Figure 4.16: Tsai-Hill for the 90-0-90 laminate texture

Hoffman: 90-0-90

	<0	0--0.001	0.001--0.005	0.005--0.02	0.02--0.08	0.08--1	>1
Percentage	0.483347679	13.01066013	31.89432563	32.9537178	15.37442892	6.28351983	0
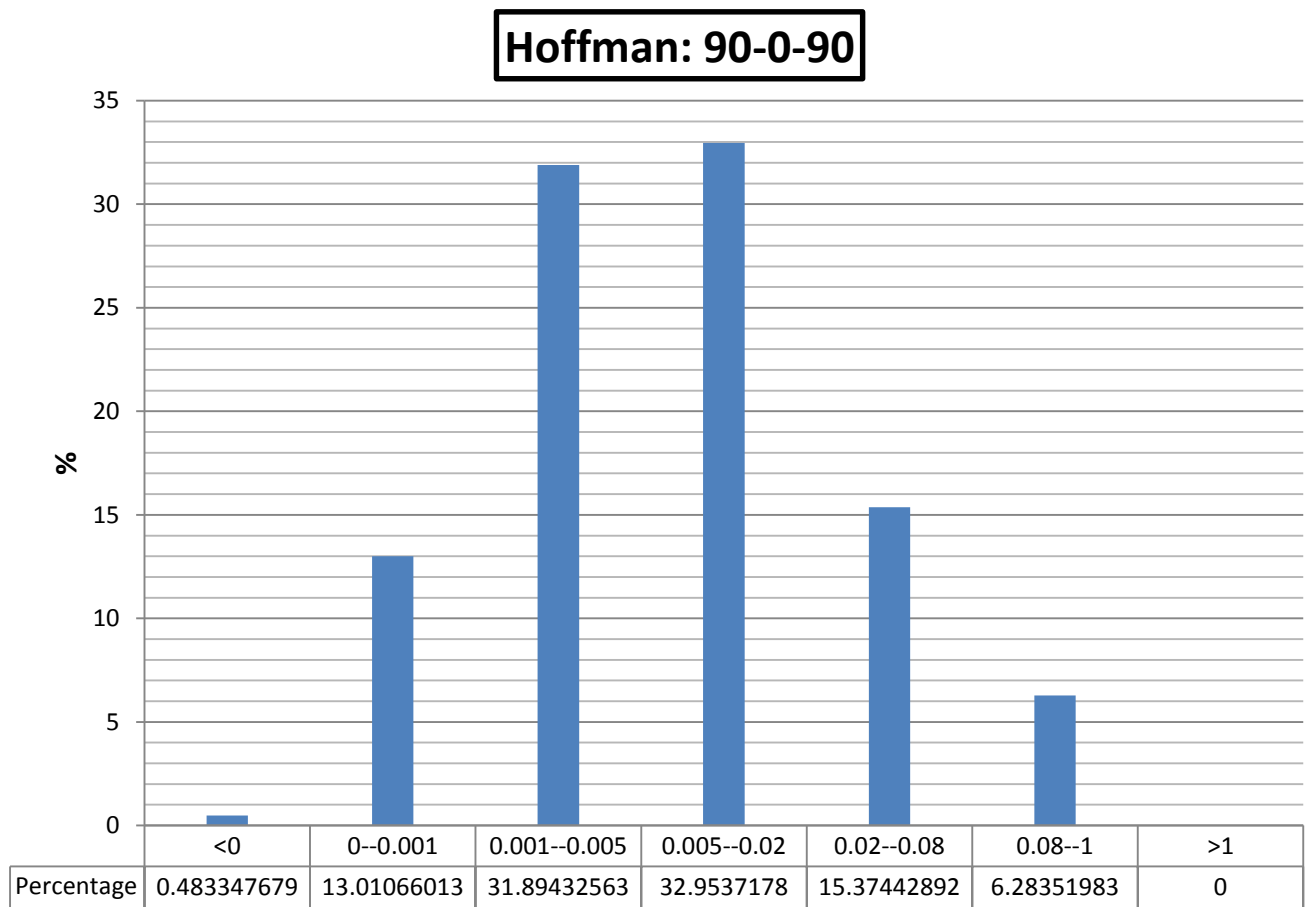
Range of f(σ)

Figure 4.17: Hoffman criteria for the 90-0-90 laminate texture

Tsai Hill vs. Hoffman : 90-0-90

Range of f(σ)	<0	0--0.001	0.001--0.005	0.005--0.02	0.02--0.08	0.08--1	>1
Hoffman	0.483347679	13.01066013	31.89432563	32.9537178	15.37442892	6.28351983	0
Hill	0.178772429	13.01066013	33.45030789	31.82811362	14.12302192	7.409124015	0

Range of f(σ)
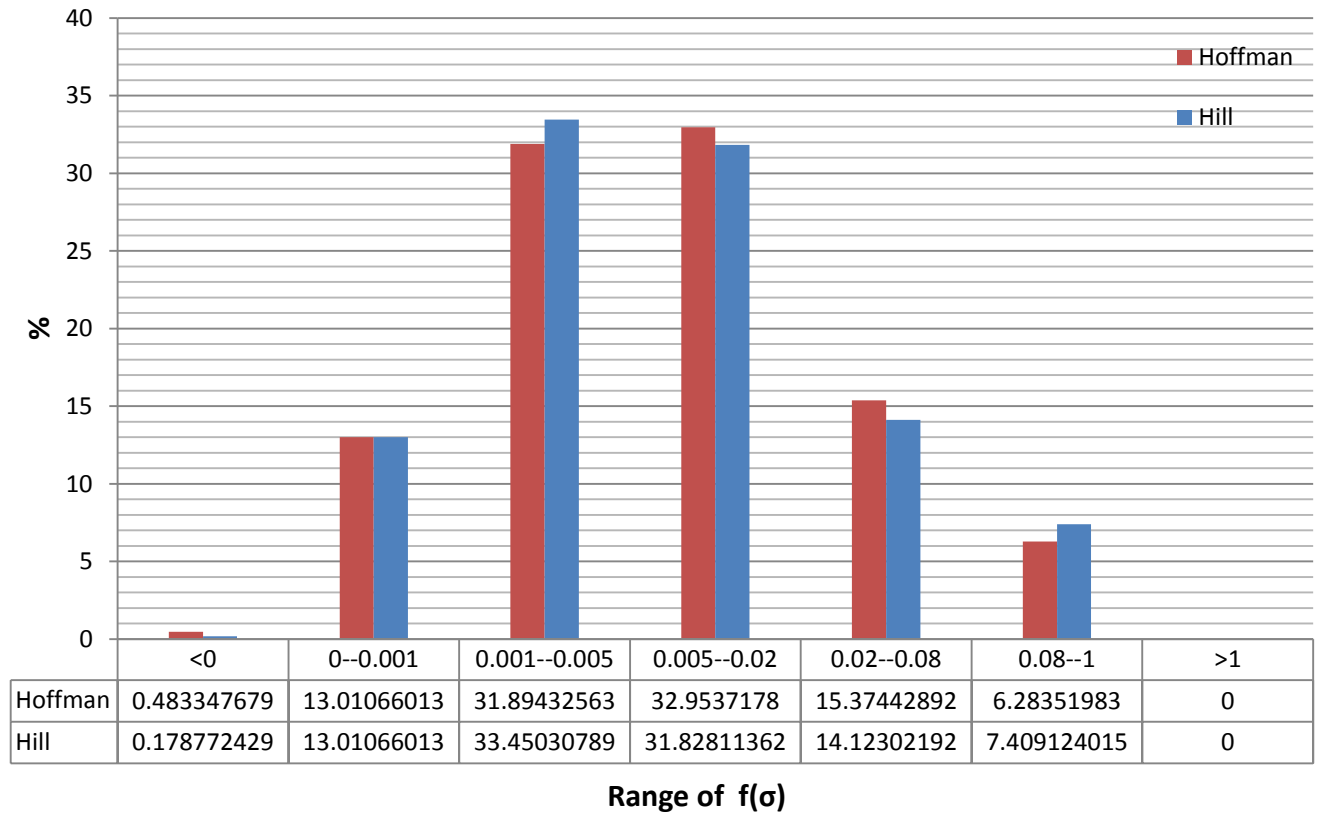
Figure 4.18: Comparison between Tsai-Hill and Hoffman criteria for the 90-0-90 texture

(0-90), (0-90-0), (90-0-90) Hill

Range of f(σ)	<0	0--0.001	0.001--0.005	0.005--0.02	0.02--0.08	0.08--1	>1
0-90	0.324438853	13.27550818	39.09157121	27.18003046	14.0435675	6.084883798	0
0-90-0	0.741574522	19.20148315	41.87909687	21.83672118	13.33509899	3.006025293	0
90-0-90	0.178772429	13.01066013	33.45030789	31.82811362	14.12302192	7.409124015	0

Range of f(σ)

Figure 4.19: Comparison between all three laminates under Tsai-Hill

(0-90), (0-90-0), (90-0-90) Hoffman

	<0	0--0.001	0.001--0.005	0.005--0.02	0.02--0.08	0.08--1	>1
90-0-90	0.483347679	13.01066013	31.89432563	32.9537178	15.37442892	6.28351983	0
0-90	1.032907369	12.99741773	33.88730716	31.78838641	15.32808051	4.965900814	0
0-90-0	0.576044494	10.85214858	28.14010461	38.4426935	19.22796795	2.761040853	0

Range of f(σ)
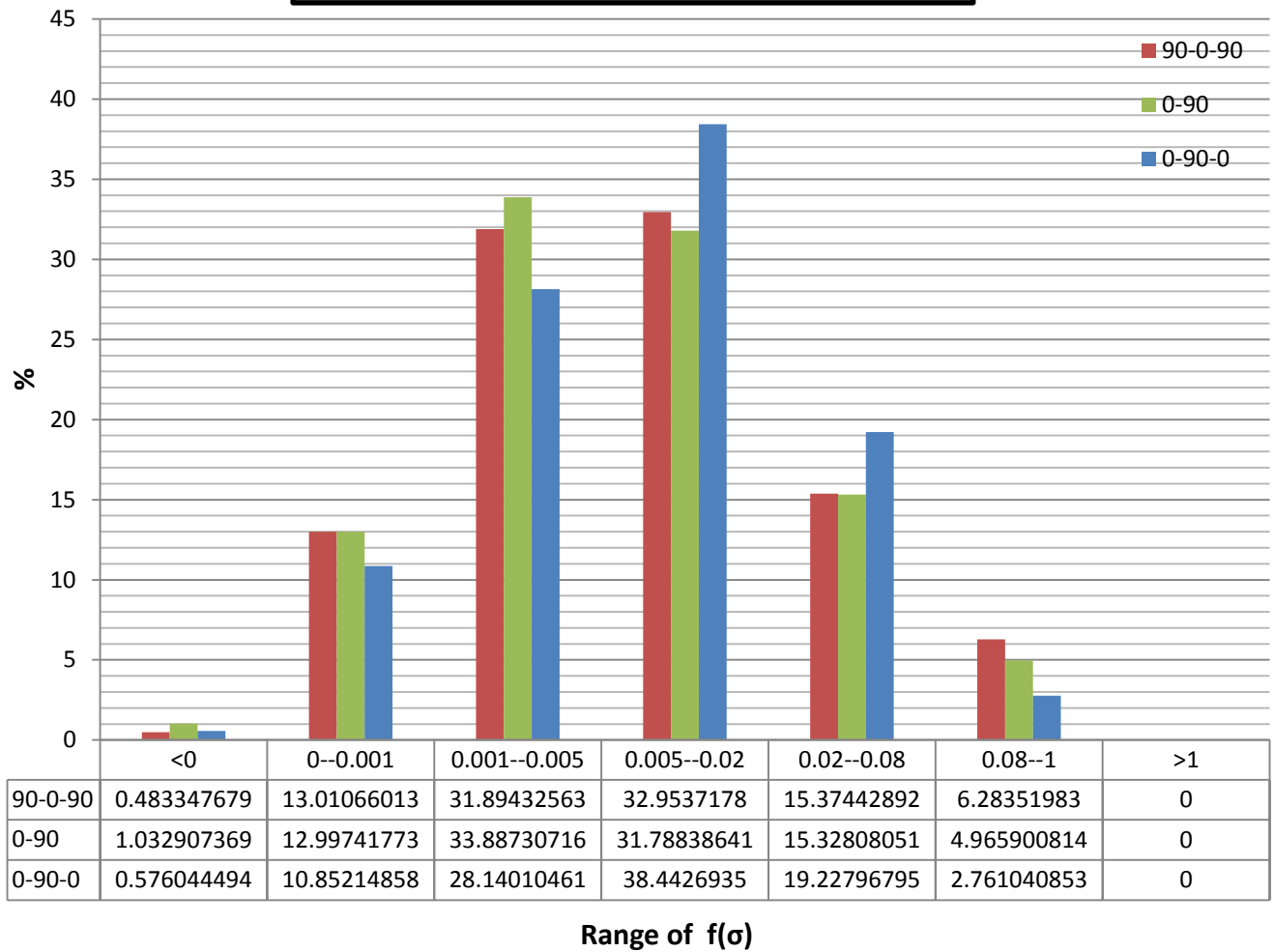
Figure 4.20: Comparison between all three laminates under Hoffman

<u>0-90</u>	$\chi = 0.016626$	$\vartheta = 0.030134$	$\beta = 1995.935$
<u>0-90-0</u>	$\chi = 0.015299$	$\vartheta = 0.022855$	$\beta = \mathbf{2860.05}$
<u>90-0-90</u>	$\chi = 0.01953$	$\vartheta = 0.036978$	$\beta = 1384.704$

The resemblance between the three laminates that is expressed in figures 4.19 and 4.20 is demonstrated by the values of β. Clearly the 0-90 and 90-0-90 offer similar performan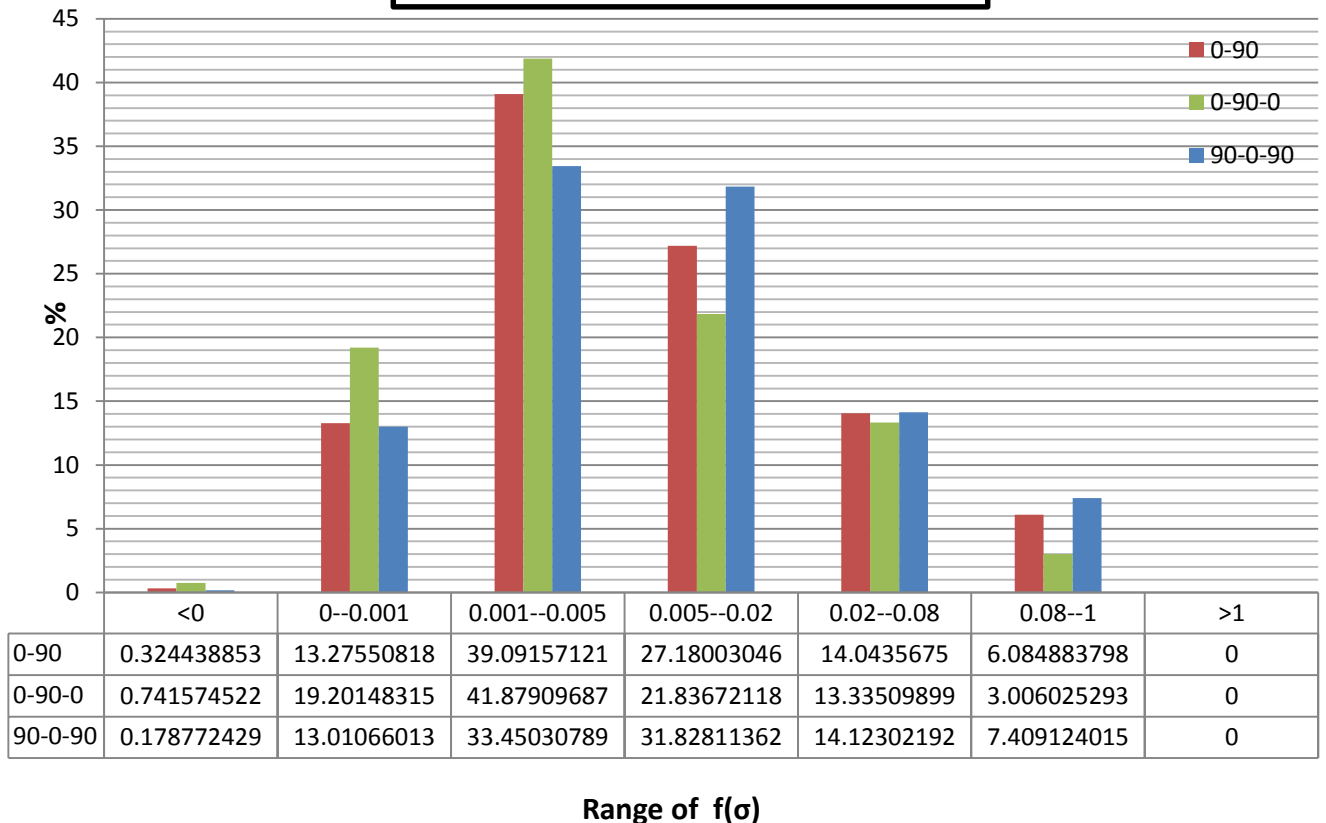ce having almost identical β parameters, but a slight advantage is noticed by the 0-90-0 texture, that possible justification is observed in fig. 4.19 and 4.20 where the 0-90-0 has the least percentage for a range near unity. In general, it is uncertain to make an absolute judgment between the laminates but rather to conclude that the performance of all three is quite similar till the conduction of further study to validate otherwise.

4.3 Static Failure: Braided Textures

Three braided composite textures were chosen for the purpose of this study: Br 30, Br 45a and Br 60.

Tsai-Hill : Br 30

	<0	0--0.001	0.001--0.005	0.005--0.02	0.02--0.08	0.08--1	1>
Percentage	0	46.81189168	29.30543601	14.88446004	8.547970602	0.450241674	0

Range of f(σ)
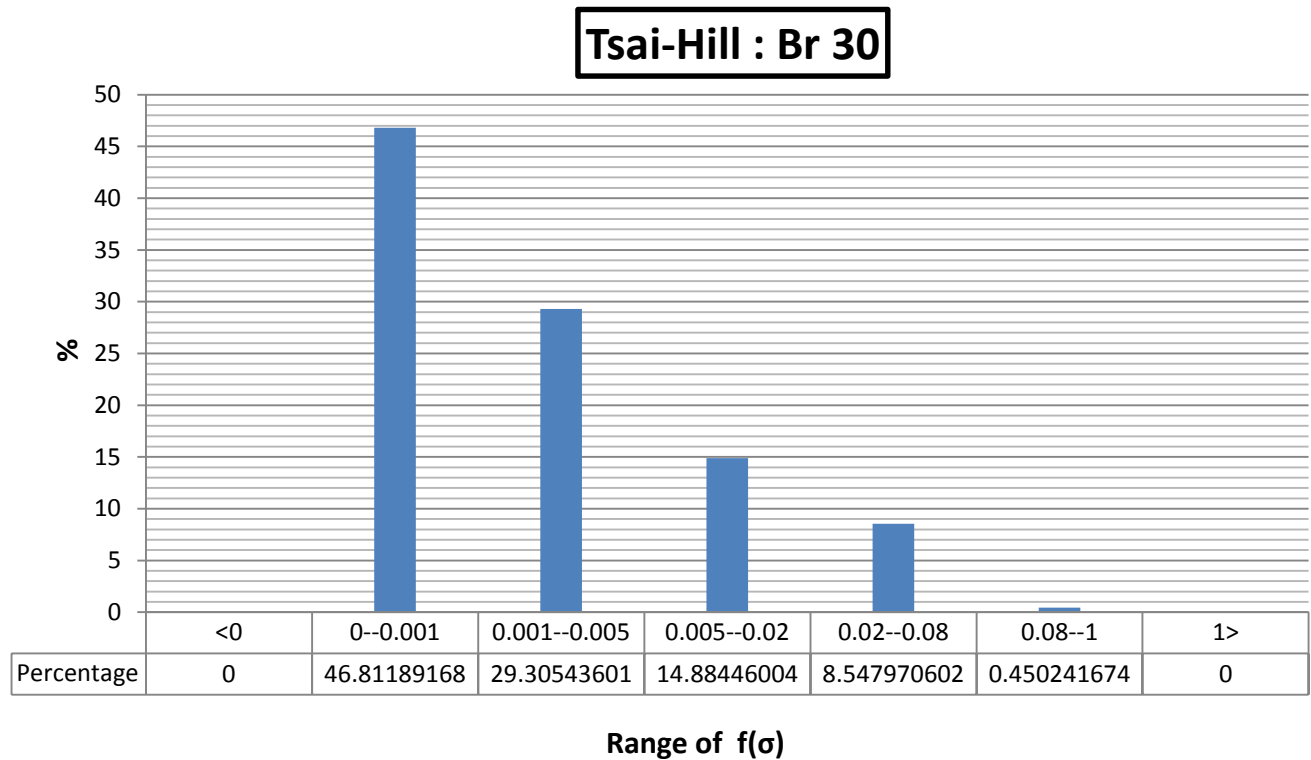
Figure 4.21: Tsai-Hill for the Br30 braded texture

Hoffman : Br 30

	<0	0-0.001	0.001--0.005	0.005--0.02	0.02--0.08	0.08--1	1>
Percentage	0	17.45348606	19.40674038	34.47659405	26.67019797	1.992981527	0

Range of f(σ)
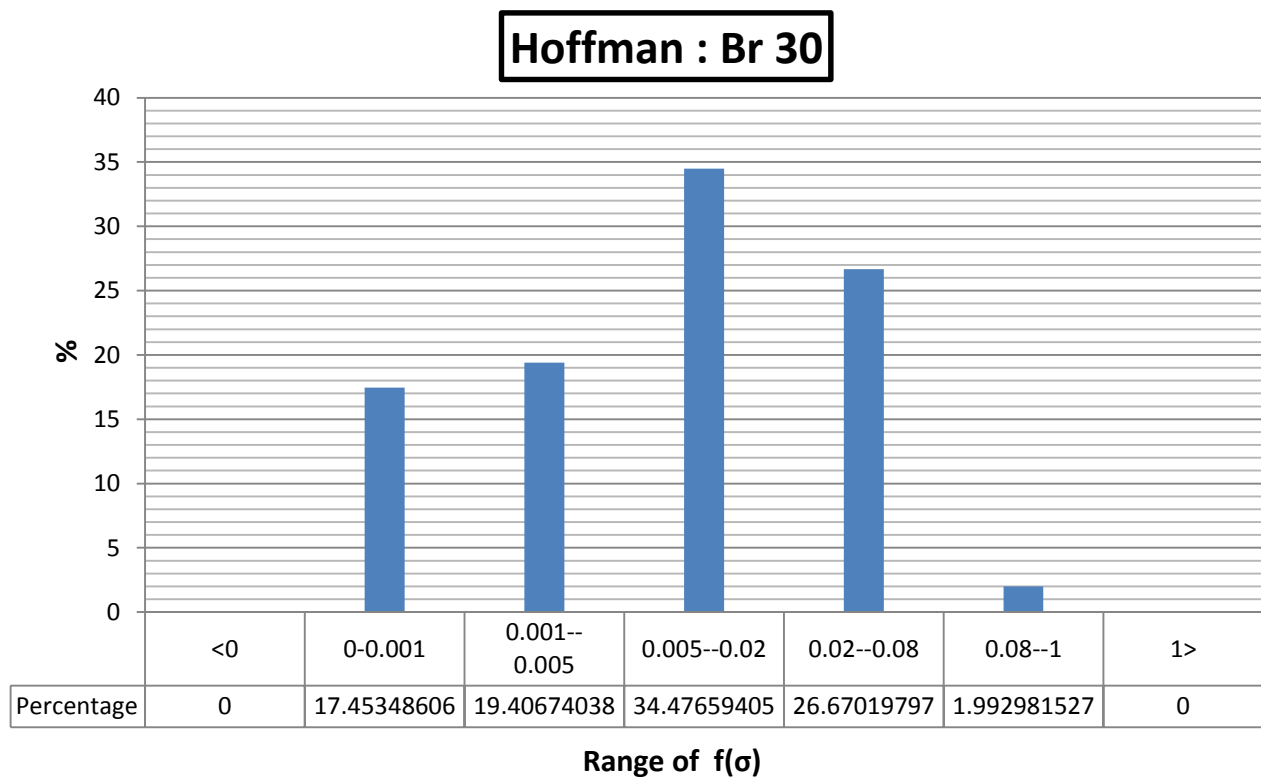
Figure 4.22: Hoffman for the Br30 braded texture

Tsai Hill vs. Hoffman : Br 30

	<0	0--0.001	0.001--0.005	0.005--0.02	0.02--0.08	0.08--1	1>
Hoffman	0	17.45348606	19.40674038	34.47659405	26.67019797	1.992981527	0
Tsai-Hill	0	46.81189168	29.30543601	14.88446004	8.547970602	0.450241674	0

Range of f(σ)
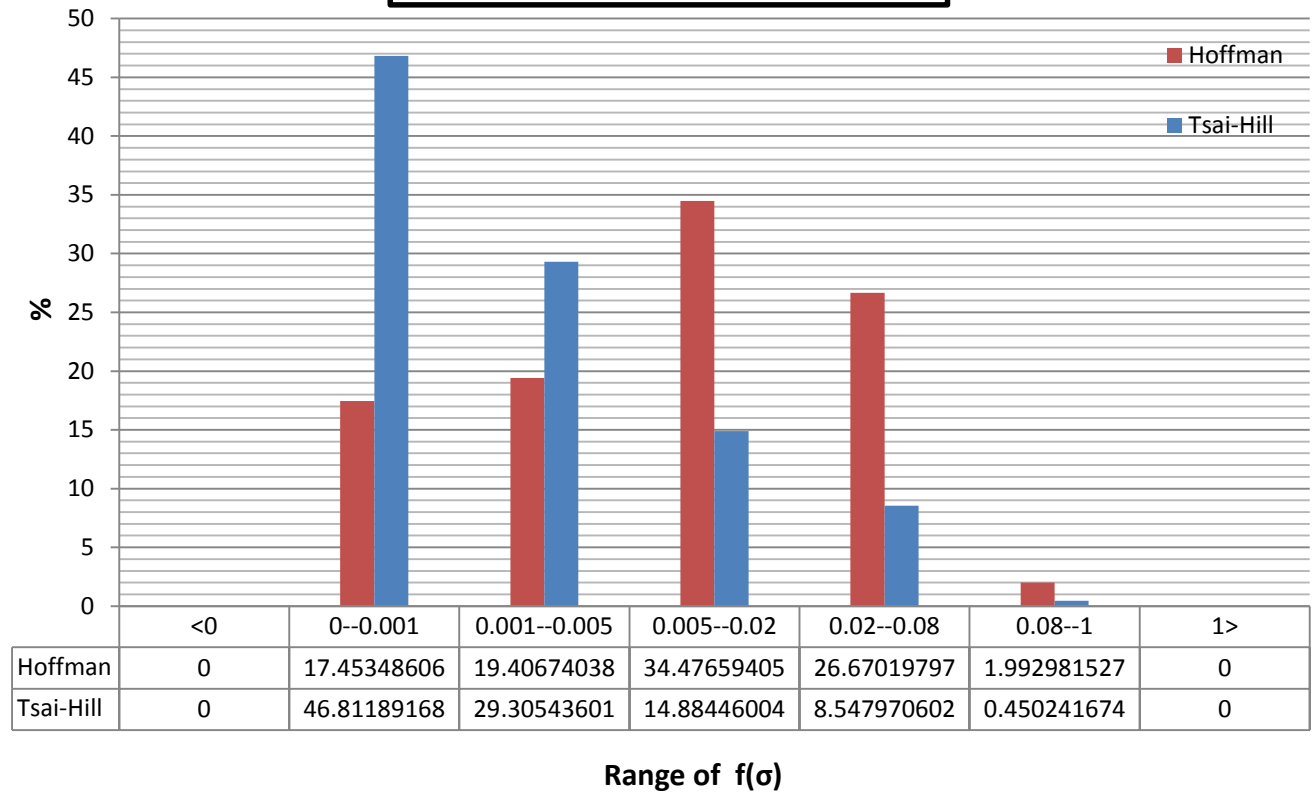
Figure 4.23: Tsai Hill vs. Hoffman: Br 30

Tsai-Hill : Br 45a

	<0	0--0.001	0.001--0.005	0.005--0.02	0.02--0.08	0.08--1	1>
Percentage	0.019863603	54.35343971	19.23458915	16.82447196	8.978348672	0.589286897	0

Range of f(σ)
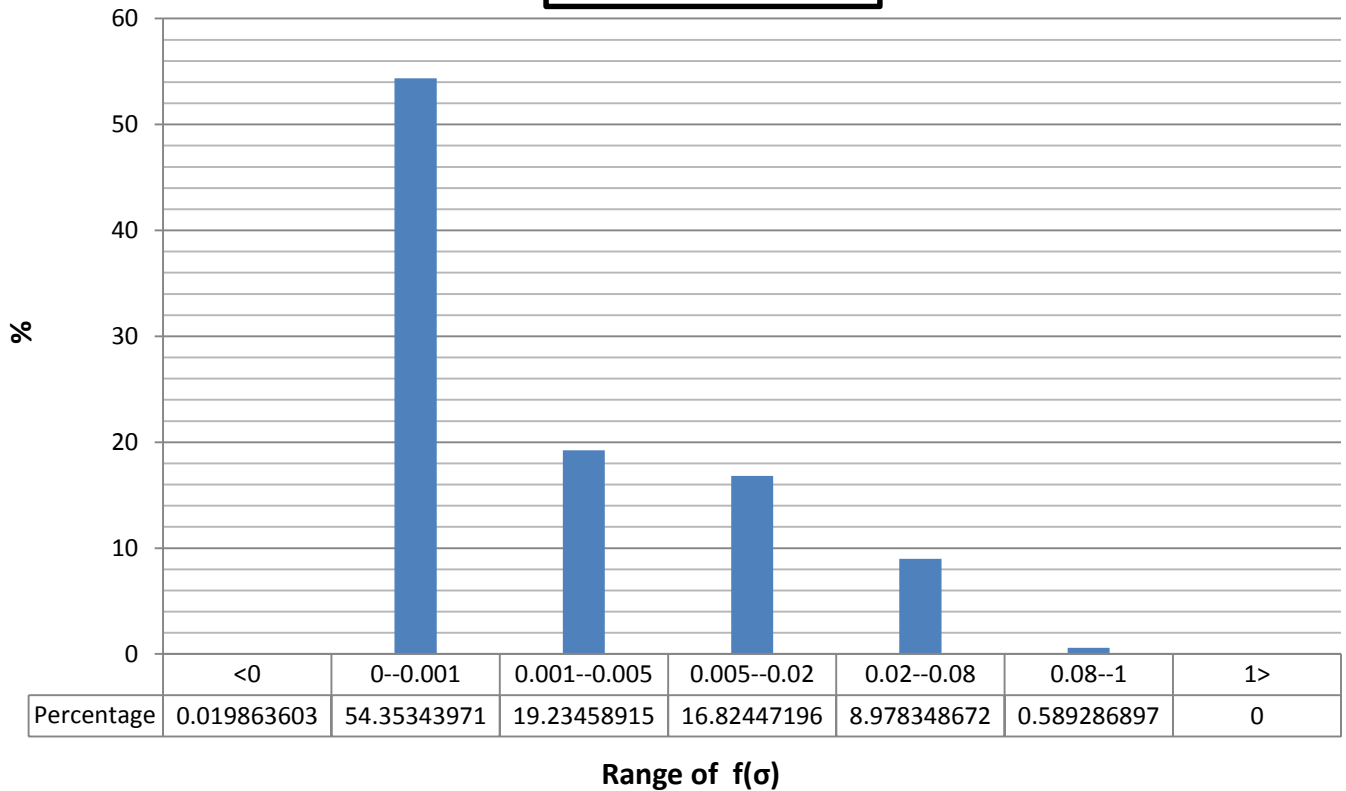
Figure 4.24: Tsai-Hill for the Br45a braded texture

Hoffman : Br 45a

	<0	0-0.001	0.001--0.005	0.005--0.02	0.02--0.08	0.08--1	1>
Percentage	0	31.79500761	29.04058796	29.59014765	9.282923922	0.291332848	0

Range of f(σ)
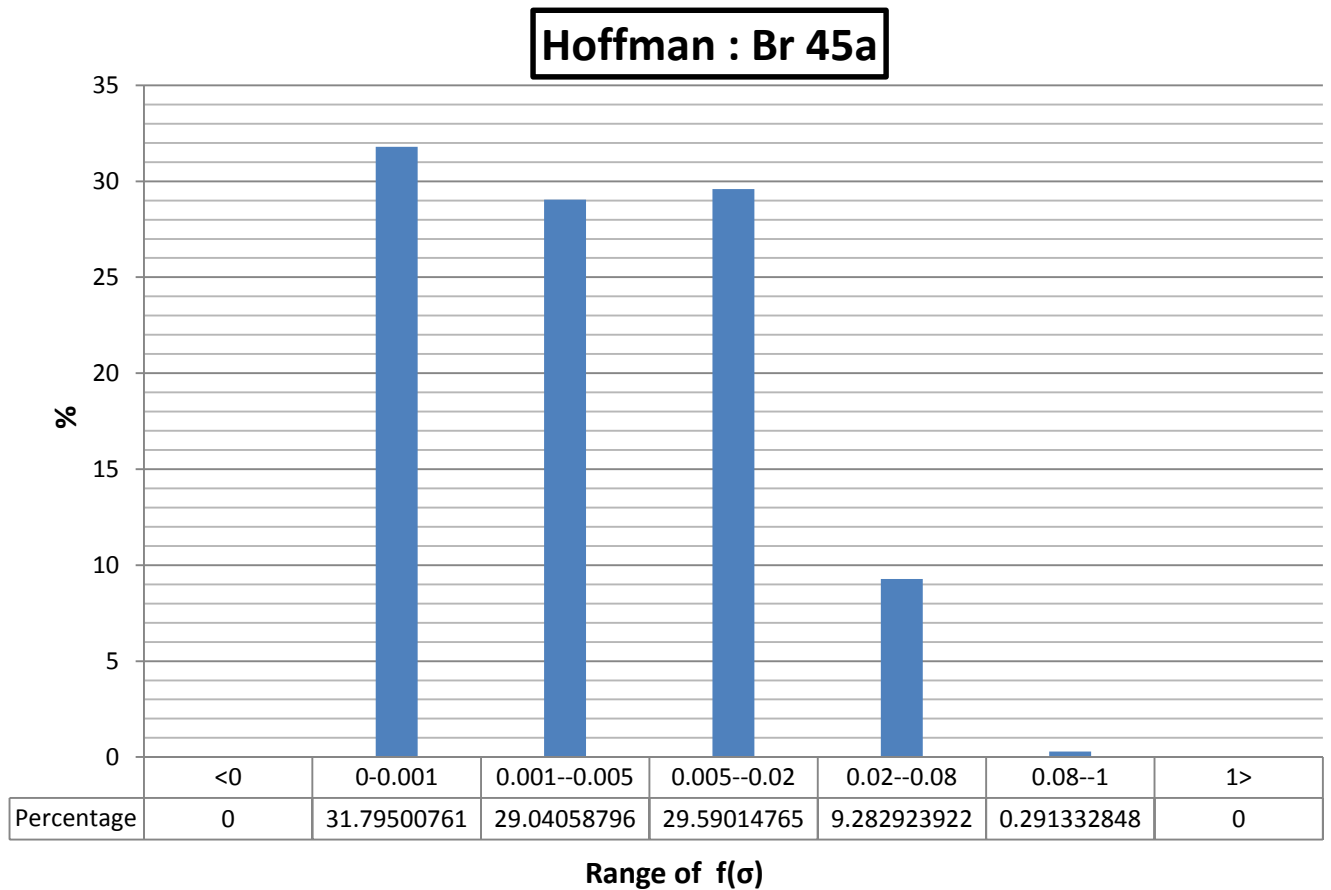
Figure 4.25: Hoffman for the Br45a braded texture

Tsai-Hill vs. Hoffman : Br 45a

	<0	0--0.001	0.001--0.005	0.005--0.02	0.02--0.08	0.08--1	1>
Hoffman	0	31.79500761	29.04058796	29.59014765	9.282923922	0.291332848	0
Hill	0.019863603	54.35343971	19.23458915	16.82447196	8.978348672	0.589286897	0

Range of f(σ)
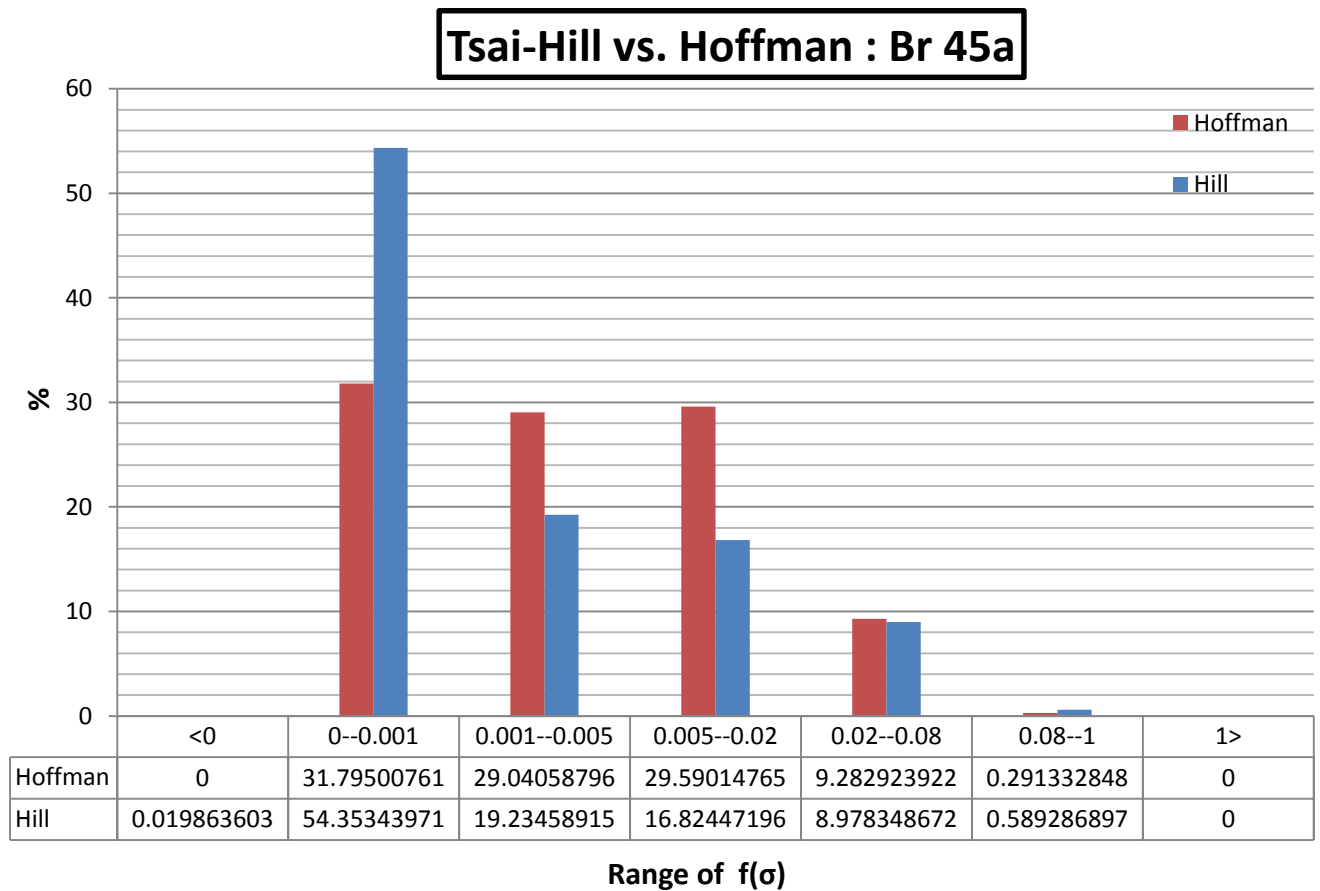
Figure 4.26: Tsai Hill vs. Hoffman: Br 45a

Tsai-Hill : Br 60

	<0	0--0.001	0.001--0.005	0.005--0.02	0.02--0.08	0.08--1	1>
Percentage	0.11918162	44.20313845	29.71595047	17.20850162	8.402304178	0.350923658	0

Range of f(σ)
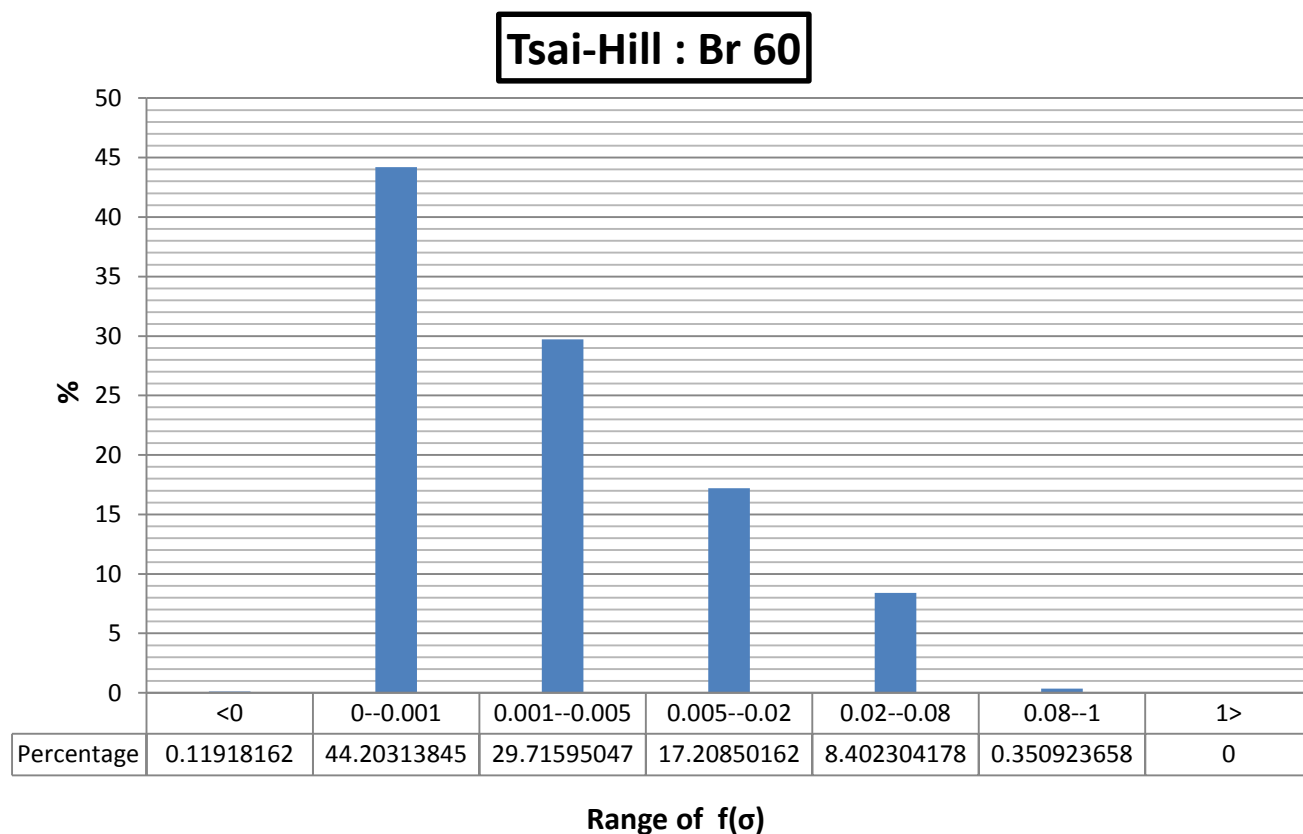
Figure 4.27: Tsai-Hill for the Br 60 braded texture

Hoffman : Br 60

	<0	0-0.001	0.001--0.005	0.005--0.02	0.02--0.08	0.08--1	1>
Percentage	0.284711647	39.46897967	31.97378004	19.72455803	8.541349401	0.006621201	0

Range of f(σ)
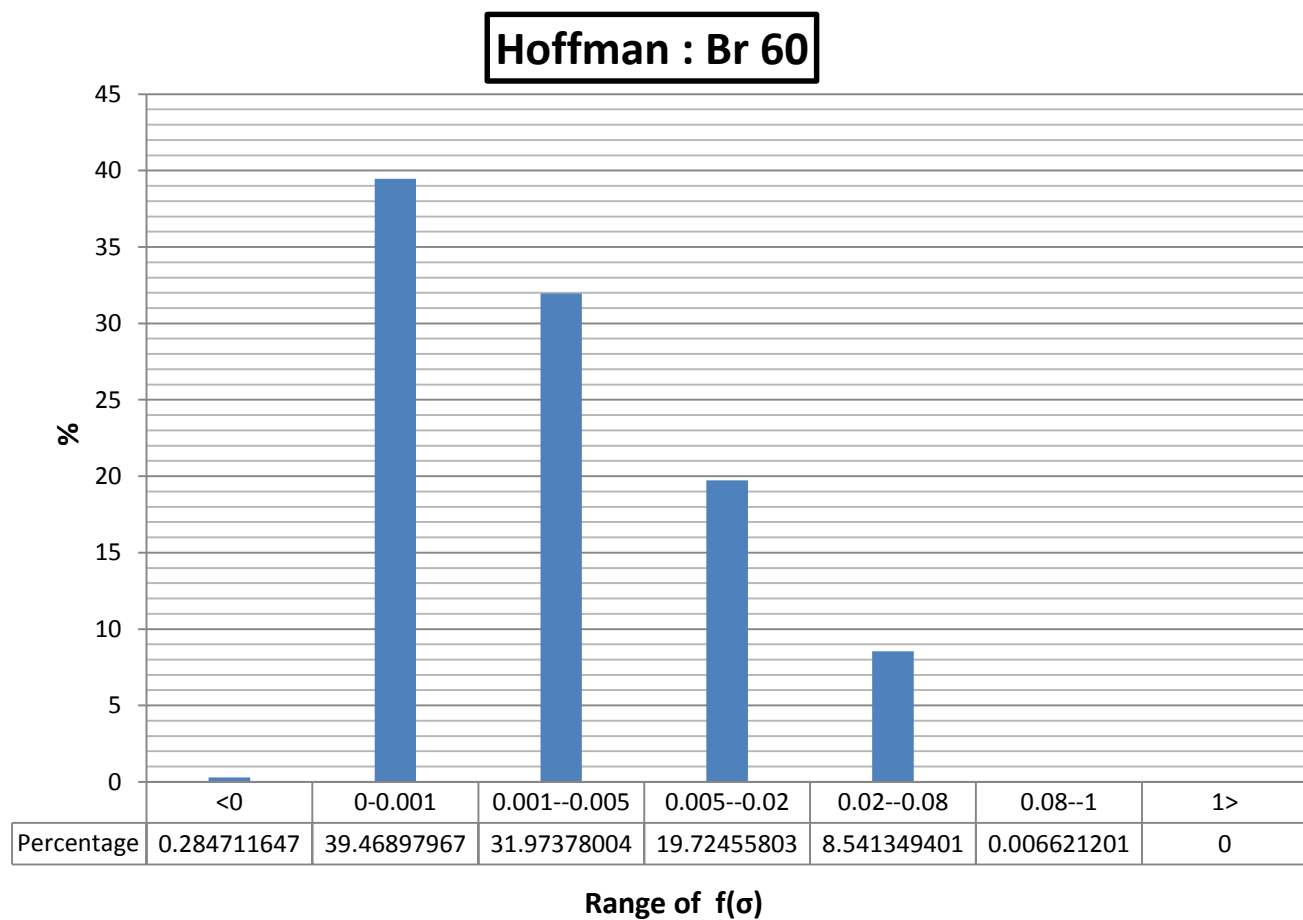
Figure 4.28: Hoffman for the Br 60 braded texture

Tsai-Hill vs. Hoffman : Br 60

	<0	0--0.001	0.001--0.005	0.005--0.02	0.02--0.08	0.08--1	1>
Hoffman	0.284711647	39.46897967	31.97378004	19.72455803	8.541349401	0.006621201	0
Hill	0.11918162	44.20313845	29.71595047	17.20850162	8.402304178	0.350923658	0

Range of f(σ)
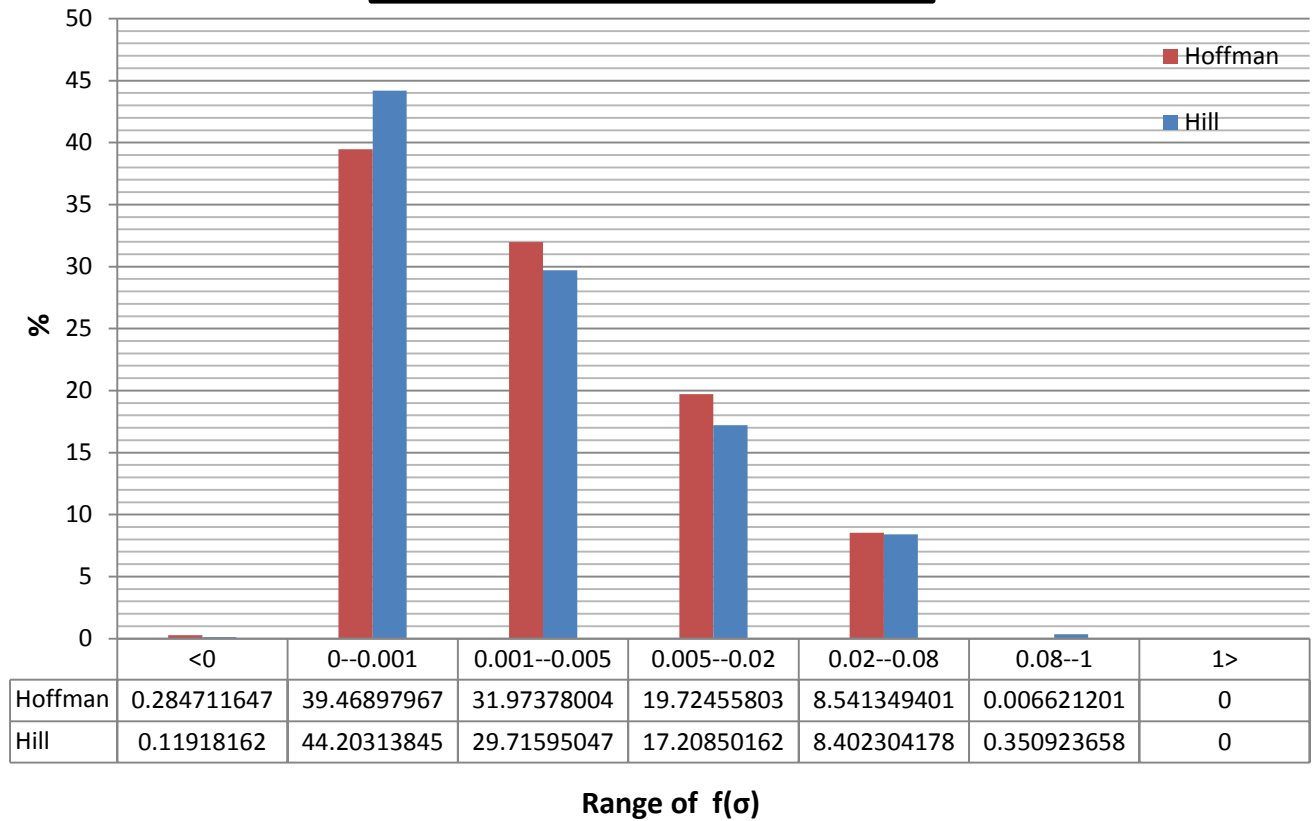
Figure 4.29: Tsai-Hill vs. Hoffman: Br 60

Br 30, Br 45a, Br 60 : Tsai-Hill

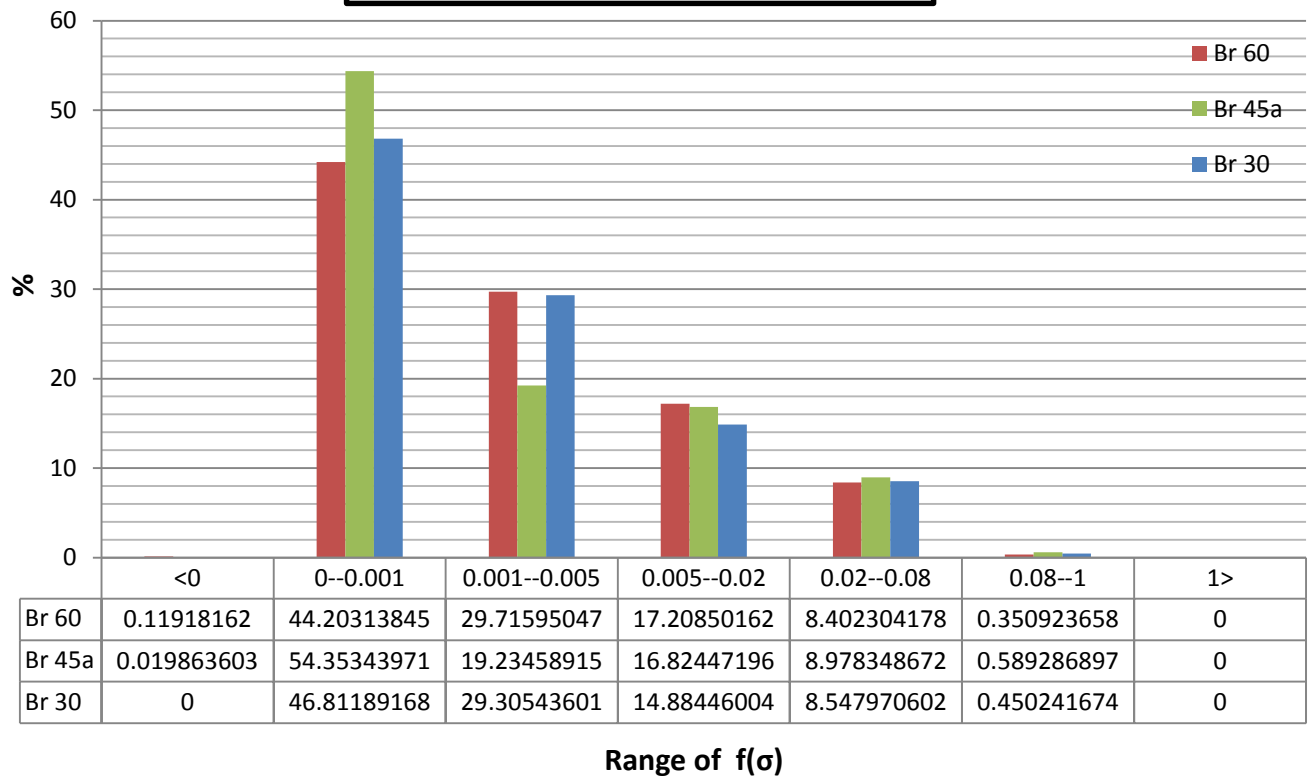|	<0	0--0.001	0.001--0.005	0.005--0.02	0.02--0.08	0.08--1	1>
Br 60	0.11918162	44.20313845	29.71595047	17.20850162	8.402304178	0.350923658	0
Br 45a	0.019863603	54.35343971	19.23458915	16.82447196	8.978348672	0.589286897	0
Br 30	0	46.81189168	29.30543601	14.88446004	8.547970602	0.450241674	0

Range of f(σ)

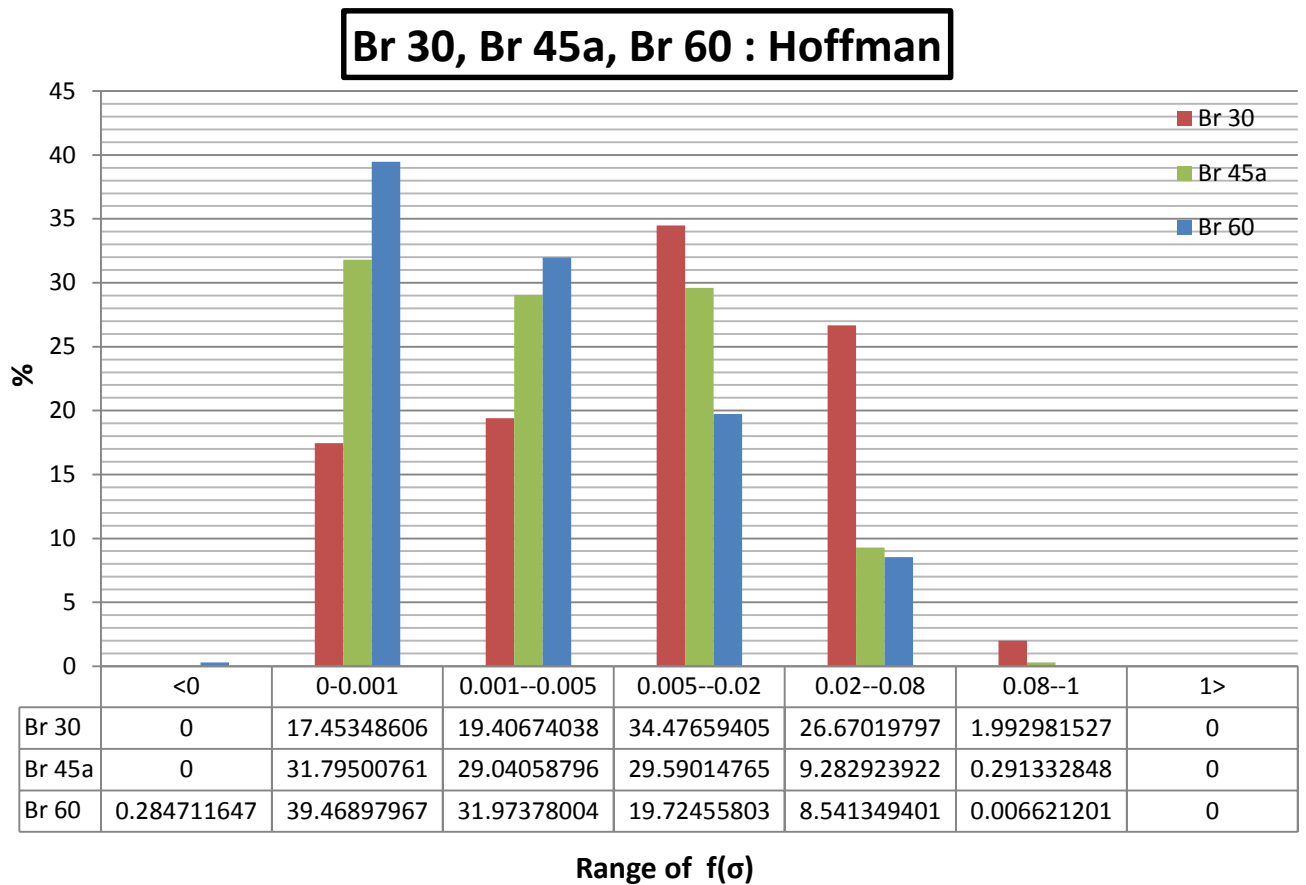Figure 4.30: Comparison between Br 30, Br 60 and Br 45a; Tsai-Hill

Figure 4.31: Comparison between Br 30, Br 60 and Br 45a; Hoffman

As for the statistical study that was performed on the interlock textures and from a direct comparison with the graphs, it is apparent that in terms of behavior in static mode, the Br 60 is the most performing.

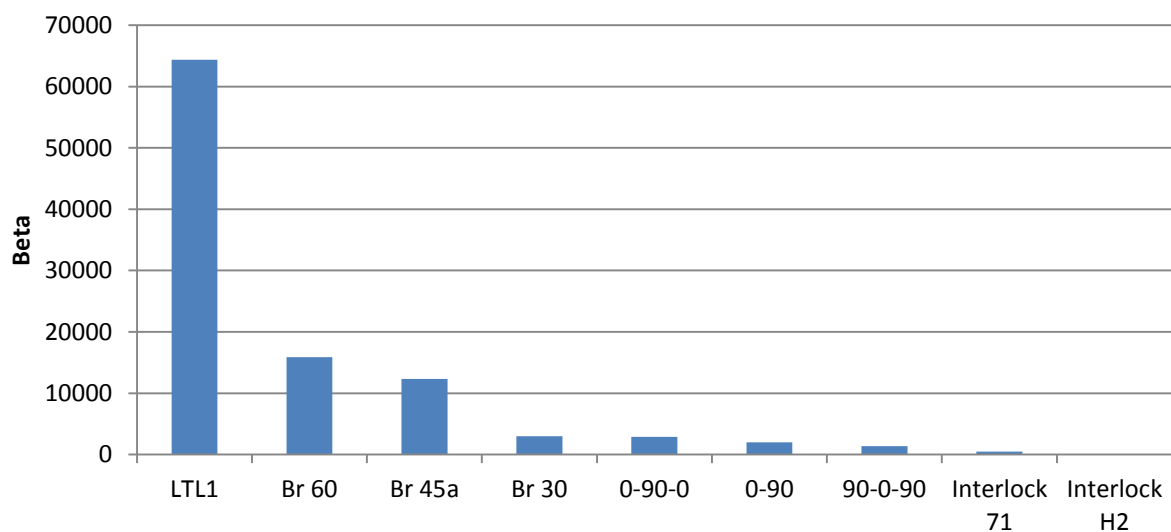|			
Br 30	$\chi = 0.016409$	$\vartheta = 0.020476$	$\beta = 2976.247$
Br 45a	$\chi = 0.007133$	$\vartheta = 0.011366$	$\beta = 12334.89$
Br 60	$\chi = 0.005894$	$\vartheta = 0.010673$	$\beta = \mathbf{15896.02}$

Figure 4.32: Comparison between Beta values of all composite textures

CHAPTER V: Fatigue Model

5.1 Overview

Even though composite materials are designated as being fatigue-insensitive, especially when compared to metallic ones, they also suffer from fatigue loads. The use of composite materials in a wide range of applications obliged researchers to consider fatigue when investigating a composite material and engineers to realize that fatigue is an important parameter that must be considered in calculations during design processes, even for structures where fatigue was not traditionally considered an issue. Although composites were initially used as replacements for ''conventional'' materials such as steel, aluminum or wood, and later as ''advanced'' materials allowing engineers to adopt a different approach to design problems, the fatigue behavior of composite materials is different from that of metallic materials. Therefore, the already developed and validated methods for the fatigue life modeling and prediction of ''conventional'' materials cannot be directly applied to composite materials [26].

Mathematical models have been developed to describe fatigue damage analytically and eventually predict the fatigue lifetime of FRP composite materials. The ideal fatigue theory is described by Sendeckyj in [27] as one based on a damage metric hat accurately models the experimentally observed damage accumulation process, considers all pertinent material, test and environmental variables, correlates the data for a large class of materials, permits the accurate prediction of laminate fatigue behavior from lamina fatigue data, is readily extendable to two-stage and spectrum fatigue loading and takes data scatter into account. These requirements cannot be met simultaneously for many reasons [27] and theoretical models that address only some of them have been introduced. For predicting the fatigue life of structural components made of composites, at least two alternative design concepts could be used: the damage-tolerant (or fail-safe) and the safe-life design concepts [26].

In the former it is assumed that a damage metric, such as crack length, delamination area, residual strength or stiffness, can be correlated to fatigue life via a valid criterion. The presence of damage is permitted as long as it is not critical i.e., it cannot lead to sudden failure. In the latter safe-life design situations cyclic stress or strain is directly associated

to operational life via the S–N or e-N curves. The structure is allowed to operate since no damage is observed, e.g., before the initiation of any measurable cracks. Although this design approach ensures the use of safe structures, it considerably increases their cost since it requires very low design values, below the estimated fatigue threshold observed in fracture mechanics experiments on FRP materials [26].

One of the broadest groups of theoretical models, representing damage-tolerant design concepts, comprises the ''phenomenological fatigue failure theories'', also referred to as ''empirical fatigue theories''. Models of this type are based on the definition of reliable S–N curves and constant life diagram formulations that are used to estimate allowable numbers of cycles to failure under any given loading pattern from constant to variable amplitude. For most practical cases however, designers require models of behavior that can predict failure under realistic load combinations that yield realistic combinations of stresses, rather than under the uniaxial stress states that usually develop during laboratory experiments [26]. Multiaxial fatigue failure criteria have been developed to take multiaxial fatigue into account [28, 29]. Most of the aforementioned examples in the literature concentrate mainly on the introduction and validation of fatigue failure criteria suitable for constant amplitude multiaxial proportional stress fields without addressing the problem of life prediction under irregular load spectra [26].

The fatigue design of a structural application is generally based on full-scale fatigue test results. However, due to time and cost constraints, the replication of this kind of experiment is always limited. Therefore, in order to increase design reliability, experimental programs are performed on specimens in parallel and the supplemented experimental results are analyzed. The behavior of the examined material must be modeled. However, mathematical models expressed by deterministic equations, which can describe the behavior of any material system, cannot easily be developed due to uncertainty regarding several factors such as the scatter of the examined population and the unpredictable parameter relationship. The objective is to derive S–N curves (such as the form of equation 5.1) that correspond to high reliability levels in the range above 90% and conform with design codes. The derivation of models for the description of the material's fatigue behavior with some statistical significance requires the production of a large number of fatigue data per stress level in order to measure the distribution of the time to failure. However, several models have been presented in the past to overcome this problem and provide reliability-based S–N curves derived from limited datasets [26].

$$\log(N) = A + B\sigma \quad or \quad \sigma = \sigma_0 N^{\left(-\frac{1}{K}\right)} \tag{5.1}$$

5.1 Progressive Fatigue Damage Model

In this research, a new model is approached, based on progressive fatigue damage and critical element models to simulate fatigue behavior and predict the fatigue life of composite laminates with stress concentration. This model, called the "regional elements" model, has three major parts: stress analysis, failure analysis, and material property degradation. A critical region of the analyzed composite laminate is considered and the elements of this region are divided into critical and sub-critical layers. Using 2-dimensional stress analysis, failure modes of these regional elements are investigated and material properties in the critical and sub-critical layers are changed according to sudden and gradual material property degradation rules. Gradual material property degradation is performed on the longitudinal tensile strength of critical layers and the longitudinal tensile stiffness of sub-critical layers. By the iteration of the aforementioned loop, fatigue damage modeling is completed and an estimate of the fatigue life of a composite laminate is obtained. The finite element method is used to assess the capabilities of the current model through a user-friendly computer program. The model predicts initial and final failure loads to within 20% of experimental results for the case of static failure analysis. However, 3-dimensional stress and failure analyses are required to improve the model for fatigue failure analysis for all the configurations [30].

In order to apply the model, a critical region must be chosen, and it is only logic to apply the progressive fatigue damage model to the weakest point of the blade. In other words, the nodal point that showed the highest value of rupture of maximum $f(\sigma)$. The flowchart of the work is represented in figure 5.1.
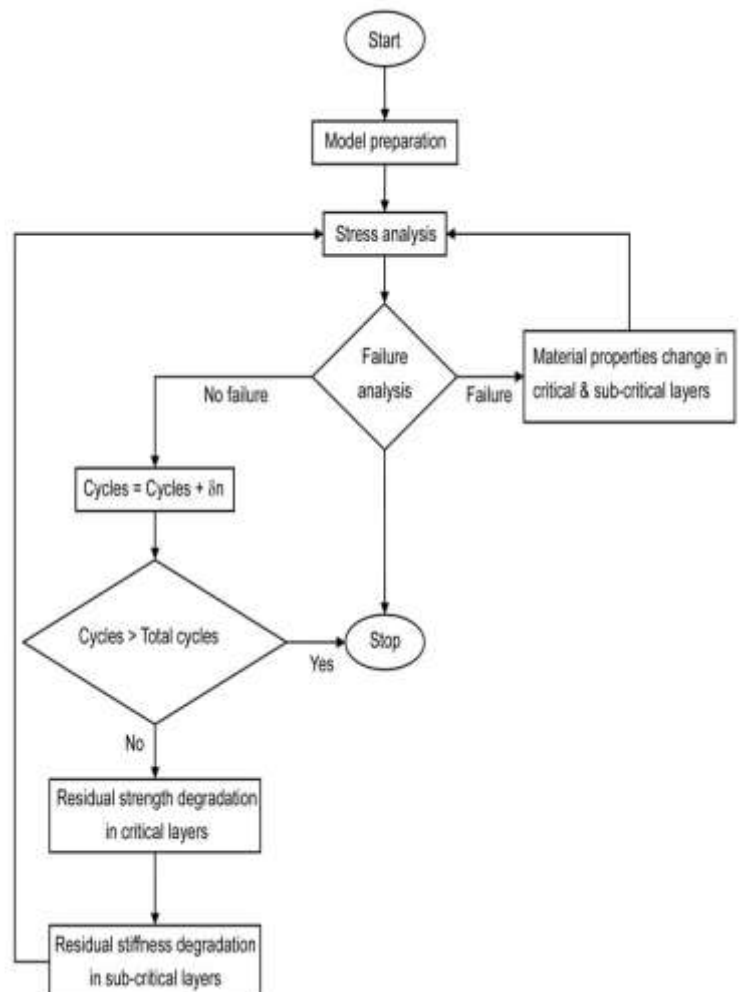

Figure 5.1: Flowchart of the progressive model

Stress Analysis is performed numerically by means of a finite element software such as ANSYS with initial model preparation that include load distribution, support fixing, initial elastic properties.

Fatigue Failure

As for the fatigue failure test, they are a set of quadratic polynomial fatigue failure criteria, capable of distinguishing between different modes of failure of a unidirectional ply under multi-axial fatigue loading conditions, were established by Shokrieh et al. In this model, only three failures were assumed possible: fiber tension, matrix tension and normal tension failure mode which are elaborated by equations 5.2, 5.3 and 5.4 respectively [4]:

$$
\left(\frac{\sigma_{xx}}{X_t(n,\sigma,R)}\right)^2 + \frac{\dfrac{\sigma_{xy}^2}{2E_{xy}(n,\sigma,R)} + 3/4\delta\sigma_{xy}^4}{\dfrac{S_{xy}^2(n,\sigma,R)}{2E_{xy}(n,\sigma,R)} + 3/4\delta\sigma_{xy}^4(n,\sigma,R)}
$$

$$
+ \frac{\dfrac{\sigma_{xz}^2}{2E_{xz}(n,\sigma,R)} + 3/4\delta\sigma_{xz}^4}{\dfrac{S_{xz}^2(n,\sigma,R)}{2E_{xz}(n,\sigma,R)} + 3/4\delta\sigma_{xz}^4(n,\sigma,R)} = g_{f+}^2
$$

(5.2)

$$
\left(\frac{\sigma_{yy}}{Y_t(n,\sigma,R)}\right)^2 + \frac{\dfrac{\sigma_{xy}^2}{2E_{xy}(n,\sigma,R)} + 3/4\delta\sigma_{xy}^4}{\dfrac{S_{xy}^2(n,\sigma,R)}{2E_{xy}(n,\sigma,R)} + 3/4\delta\sigma_{xy}^4(n,\sigma,R)} + \left(\frac{\sigma_{yz}}{S_{yz}(n,\sigma,R)}\right)^2 = g_{M+}^2
$$

(5.3)

$$
\left(\frac{\sigma_{zz}}{Z_t(n,\sigma,R)}\right)^2 + \frac{\dfrac{\sigma_{xz}^2}{2E_{xz}(n,\sigma,R)} + 3/4\delta\sigma_{xz}^4}{\dfrac{S_{xz}^2(n,\sigma,R)}{2E_{xz}(n,\sigma,R)} + 3/4\delta\sigma_{xz}^4(n,\sigma,R)} + \left(\frac{\sigma_{yz}}{S_{yz}(n,\sigma,R)}\right)^2 = g_{N+}^2
$$

(5.4)

n, σ, κ and δ are the number of cycles, stress state, stress ratio and parameter of material nonlinearity, respectively.

If $g_{f+} > 1$ then the failure is considered to be catastrophic but if either g_{N+} or g_{M+} are greater than one, in this case normal failure is detected.

Material Property Degradation

In the previous section, suitable failure criteria were established to detect the sudden fatigue failure modes of a unidirectional ply under biaxial state of stress. As failure occurs in a ply of a laminate, material properties of that failed ply are changed by a set of sudden material property degradation rules. Some of the failure modes are catastrophic and some of them are not.

Therefore, for a unidirectional ply failed under each mode of fatigue failure, there exists an appropriate sudden material property degradation rule [30].

Sudden Material Property Degradation Rules

The sudden material property degradation rules for some failure modes of a unidirectional ply under a bi-axial state of stress are available in literature. A complete set of sudden material property degradation rules for all the various failure modes of a unidirectional ply under a multi-axial state of static and fatigue stress was developed by Shokrieh et al. [4]. Sudden material degradation rules of a unidirectional ply under a biaxial state of fatigue stress are explained in the following sections.

1. Fiber tension failure degradation

Fibre Tension or Compression Property Degradation Fibre tension or fibre compression failure modes of a unidirectional ply are catastrophic modes of failure, and when one of them occurs the failed material cannot sustain any type of stress. Thus, all material properties of the failed ply were reduced to zero, as follows:

Stiffness and Poisson's ratios:

$$[E_{xx}, E_{yy}, E_{zz}, E_{xy}, E_{xz}, E_{yz}, \upsilon_{xy}, \upsilon_{xz}, \upsilon_{yz}, \upsilon_{yx}, \upsilon_{zx}, \upsilon_{zy}] \rightarrow [0,0,0,0,0,0,0,0,0,0,0,0]$$

Strengths:

$$[X_t, Y_t, Z_t, X_c, Y_c, Z_c, S_{xy}, S_{xz}, S_{yz}] \rightarrow [0,0,0,0,0,0,0,0,0]$$

2. Matrix tension failure degradation

Stiffness and Poisson's ratios:

$$[E_{xx}, E_{yy}, E_{zz}, E_{xy}, E_{xz}, E_{yz}, v_{xy}, v_{xz}, v_{yz}, v_{yx}, v_{zx}, v_{zy}] \rightarrow$$

$$[E_{xx}, 0, E_{zz}, E_{xy}, E_{xz}, E_{yz}, v_{xy}, v_{xz}, 0, 0, v_{zx}, v_{zy}]$$

Strengths:

$$[X_t, Y_t, Z_t, X_c, Y_c, Z_c, S_{xy}, S_{xz}, S_{yz}] \rightarrow [X_t, 0, Z_t, X_c, Y_c, Z_c, S_{xy}, S_{xz}, S_{yz}]$$

After detecting this mode of failure which is not catastrophic, the other modes of failure must be verified.

3. Normal tension failure degradation

Stiffness and Poisson's ratios:

$$[E_{xx}, E_{yy}, E_{zz}, E_{xy}, E_{xz}, E_{yz}, v_{xy}, v_{xz}, v_{yz}, v_{yx}, v_{zx}, v_{zy}] \rightarrow$$

$$[E_{xx}, E_{yy}, 0, E_{xy}, E_{xz}, E_{yz}, v_{xy}, v_{xz}, v_{yz}, v_{yx}, 0, 0]$$

Strengths:

$$[X_t, Y_t, Z_t, X_c, Y_c, Z_c, S_{xy}, S_{xz}, S_{yz}] \rightarrow [X_t, Y_t, 0, X_c, Y_c, Z_c, S_{xy}, S_{xz}, S_{yz}]$$

Gradual Material Property Degradation Rules

To simulate the behavior of a unidirectional ply under multi-axial fatigue loading a technique called the generalized residual material property degradation technique was established by Shokrieh et al. [4]. This technique consists of a normalized strength, a normalized residual stiffness and a normalized fatigue life model. A modified version of this technique was used in this research. For the residual strength of a unidirectional ply under arbitrary uni-axial state of stress ratio, an equation is presented by Shokrieh et al. [4] as follows eq.5.5:

$$R(n, \sigma, R) = \left[1 - \left(\frac{\log(n) - \log 0.25}{\log(N_f) - \log 0.25}\right)^{\beta}\right]^{\frac{1}{\alpha}} (R_s - \sigma) + \sigma \qquad (5.5)$$

where R(n,σ,κ), R_s, n, σ, N_f, and *R* represent residual strength, static strength, number of cycles, magnitude of applied maximum stress, fatigue life at σ, and stress ratio, respectively. Parameters α and β are experimental curve fitting parameters.

In this thesis, the modeling of the gradual degradation of the stiffness and the strength was assumed to follow a normalized polynomial form where:

$$E(n) = [A\left(\frac{n}{N_f}\right) + 1]E_s \qquad (5.6)$$

Where E and E_s are the residual and static stiffness, respectively, n the number of cycle, N_f the number of cycles to failure and A an experimental fitting parameter. It is assumed that this degradation applies to all the directions of the laminates [31].

In the same way to stiffness, the gradual degradation of strength was modeled by fitting experimental data. The general form of the polynomials in terms of residual strength and normalized number of cycles is:

$$T(n) = [B\left(\frac{n}{N_f}\right)^2 + C\left(\frac{n}{N_f}\right) + 1]T_s \qquad (5.7)$$

Where T and T_s are the residual and static strengths respectively, n the number of cycles, N_f the number of cycles to failure, and B, C are experimental fitting parameters. Equation 5.7 is used in order to model the degradation of all strength components.

Another LabView code was written to translate the flowchart explained in figure 5.1. Refer to Annex C.

CONCLUSION & FUTURE WORK

From the current results, following conclusions can be drawn:

- The BEM method for aerodynamic modeling offered great simplicity and accuracy. In Annex B, some of the performance validations of a wind turbine are made. Also, reference [5] and [6] regarded a similar subject displaying the deflection along the blade length, tip deflection, power curves and force/moment curves; these results confirm the correctness of our BEM code.
- The effectiveness of the finite-element method using the ANSYS software permitting an integrated approach with the BEM method.
- The similarity with the results of each static failure criteria which is predictable mainly due to the assumptions made in regards to the compression mode.
- Between all the tested composite materials, the LTL1 gave the highest degree of safety. As for the interlocks, the interlock 71 had an advantage over the interlock h2, the last showed signs of possible rupture and hence weaker fatigue behavior. The laminates had almost alike performance, but some signs that the 0-90-0 texture has some lead to be justified.

Many issues remain unanswered. Some of the following points can be considered

- The fatigue model requires more elaboration especially in terms of the proper definition of a REV or Representative Elementary Volume to which continuous degradation of a critical REV will be made.
- Experimental validation for the derivation of the experimental fitting parameters for the fatigue model.
- Airfoil data were extracted from Xfoil and a unique airfoil was assumed for the whole blade. Further research could detail further the study by decomposing the blade into different airfoils for various blade regions as it is in reality.
- Proper layer modeling of the blade should be made rather than introducing a thickness. This makes for a more rational finite-element modeling but as a result a longer computational time

- It would be interesting to verify the results by means of a CFD-FEM coupling, such as the use of COMSOL to determine the pressure distribution over a 2D airfoil or model the entire blade.

- Investigate the dynamic behavior of the wind turbine to include all the loads other than the static loadings, these loads contribute to fatigue and blade deterioration of both material properties and performance loss. A way must be found to model and transfer these loads to the FEM solver.

It is concluded that with respect to a material blade design cycle, the coupling between a finite element package and blade element and momentum code under steady and static conditions can be useful. Especially when an integration between this coupled approach and a dynamic simulation tool could be established, a more advanced flexible blade design can be then analyzed for a novel generation of more flexible wind turbine blades.

ANNEX

A. Aerodynamic Blade Data

The geometry that was used in the finite element analysis is a 41 m blade having an S821 airfoil profile. During the aerodynamic analysis, it was possible to decompose the blade into multiple sections but it was regarded that for the intention of a comparative study between composite textures, dividing the blade into 4 sections is reasonable. Table A.1 shows all the geometric and physical parameters of the cross sections and figure A.1-A.2-A.3 include the airfoil aerodynamic data.

Radius [m]	Chord [m]	Angle of Incidence [deg]
8.25	3.16	18.8
16.5	2.74	5.8
24.75	2.14	3.95
33	1.57	0
41.25	1.1	0

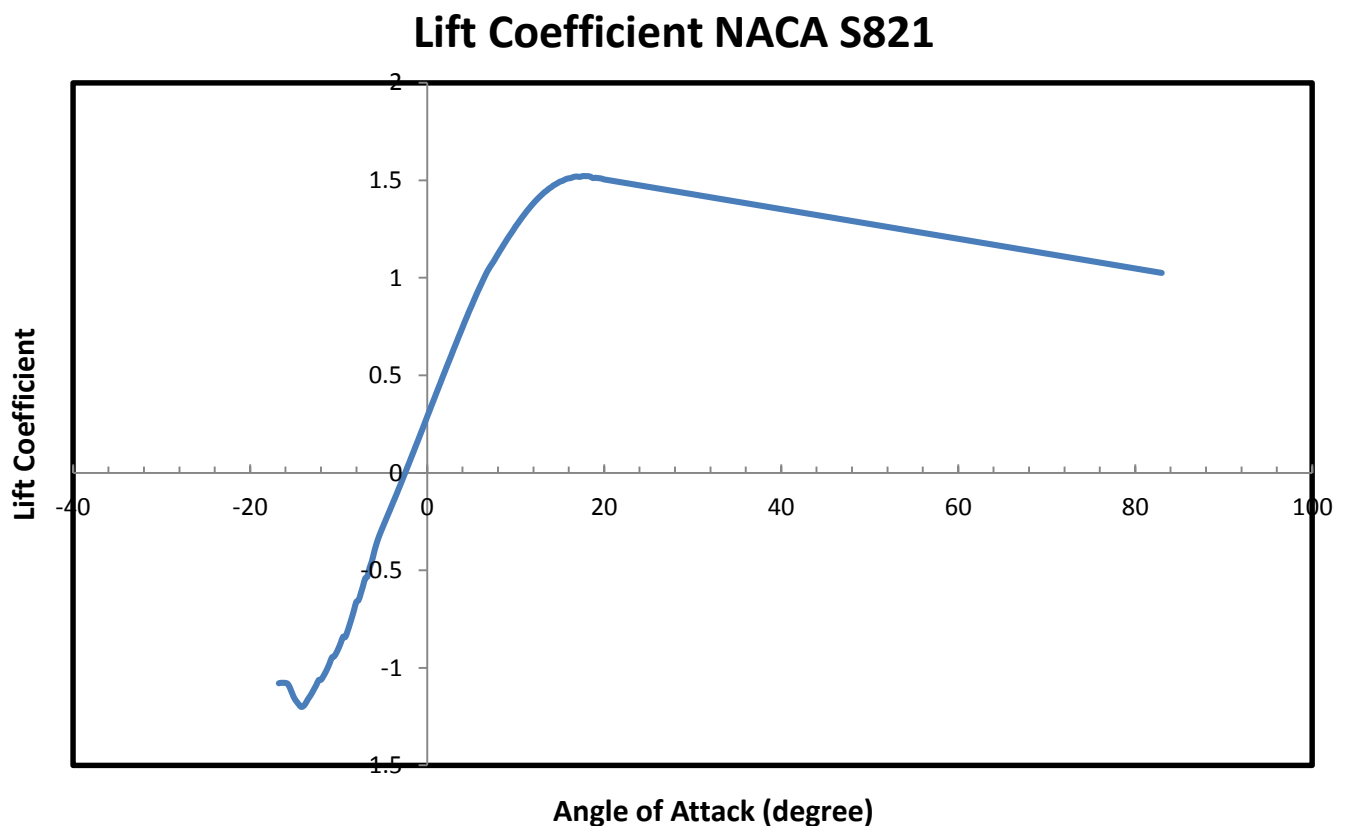**Table A.4: Blade properties**

Figure A.1: Lift coefficient for NACA S821
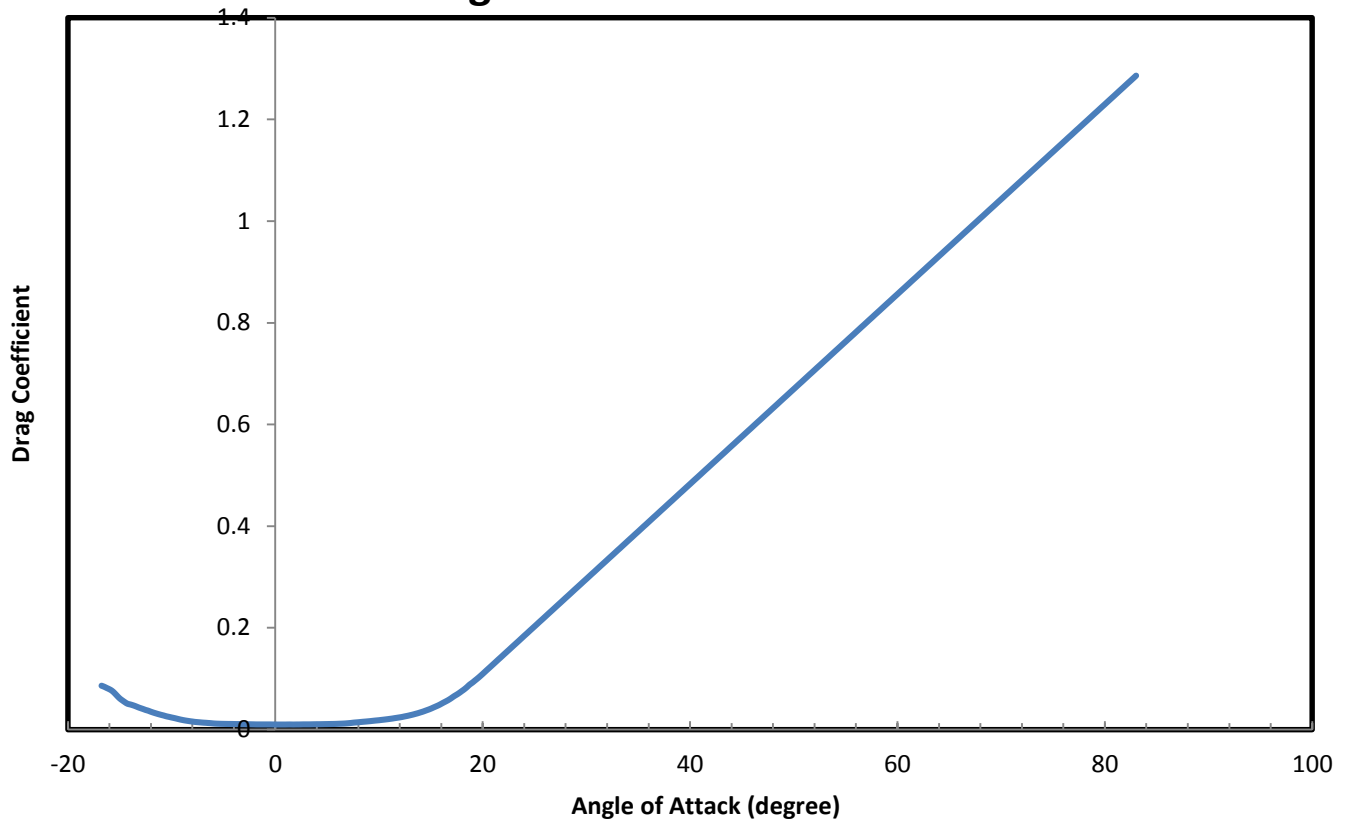
Drag Coefficient NACA S821

Figure A.5: Drag coefficient for NACA S821
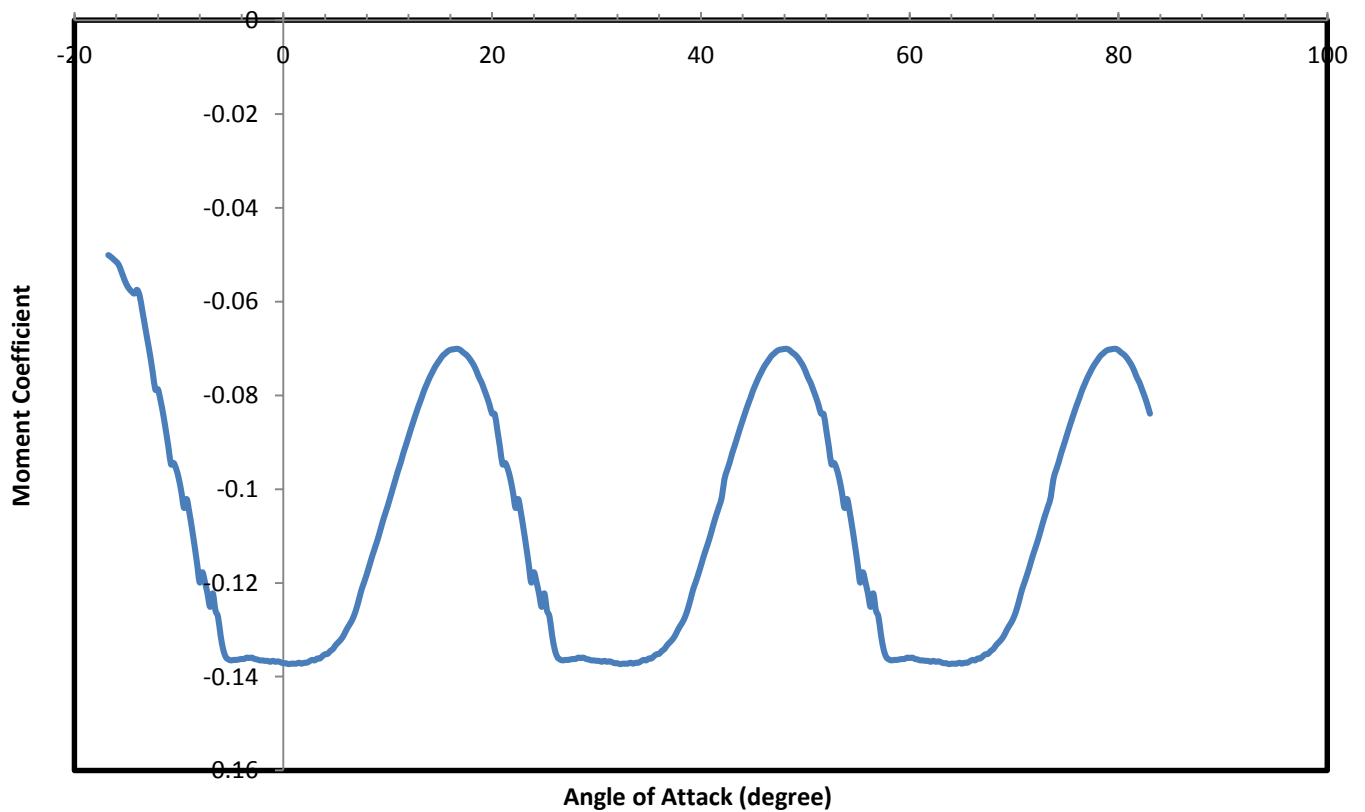
Moment Coefficient NACA S821

Figure A. 6: Moment coefficient for NACA S821

B. BEM Model Verification

To verify the output of the BEM code, a 1.5 MW wind turbine was chosen. The main configurations are explained in Table B.1 and the structural descriptions can be found in Table B.2. The wind turbine blade structure used in this work is based on the WindPACT 1.5 MW Baseline 3-Bladed Turbine (WP1.5MW) described in the WindPACT Turbine Rotor Design Study [32]. Validation of the performance of the wind turbine is shown in Fig B.3. The block diagram of the BEM code appears in Fig B.4.

Rating	1.5 MW
Configuration	3 blades, upwind
Drive train	High speed, multiple-stage gearbox
Control	Variable speed and pitch control
Max. rotor speed	20.5 rpm
Blade coning	0°
Rated wind speed	11.8 m/s
Cut-out wind speed	27.5 m/s
Rotor diameter	70 m
Hub height	84 m
Rotor mass	32.02 tons
Nacelle mass	52.84 tons
Tower mass	122.52 tons

Table B.1: Parameters of the WP1.5MW machine

r/R	Twist [deg]	Mass density [kg/m]	Flap Stiff [N.m^{2}x10^6]	Edge Stiff [N.m^{2}x10^6]	Torsional Stiff [N.m^{2}x10^6]
0	11.1	1447.607	7681.46	7681.46	2655.23
0.052	11.1	181.672	1020.62	1092.28	343.81
0.157	11.1	186.138	523.14	833.66	127.19
0.263	9.5	178.321	234.57	614.65	16.8
0.368	6.3	158.222	154.9	435.26	12.64
0.473	3.1	138.123	75.23	255.87	8.48
0.578	2.1	107.669	49.75	179.86	5.76
0.684	1.1	77.215	24.27	103.85	3.04
0.789	0.48	51.861	9.27	54.25	1.38
0.894	0.24	31.607	4.75	31.06	0.78
1	0	11.353	0.23	7.87	0.18

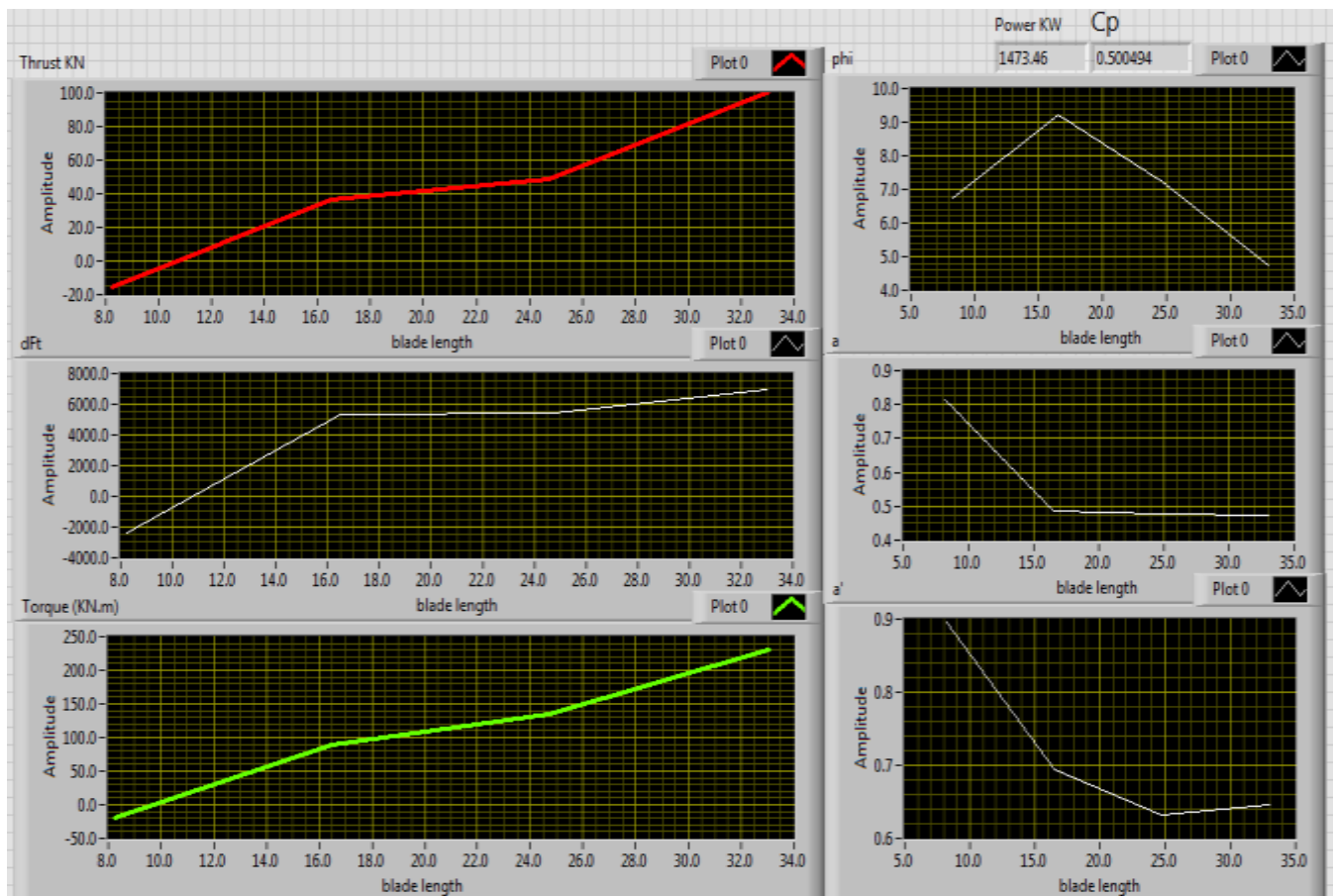**Table B.2: WP1.5MW Structural Blade Definition**

Figure B.3: BEM performance results using LabView
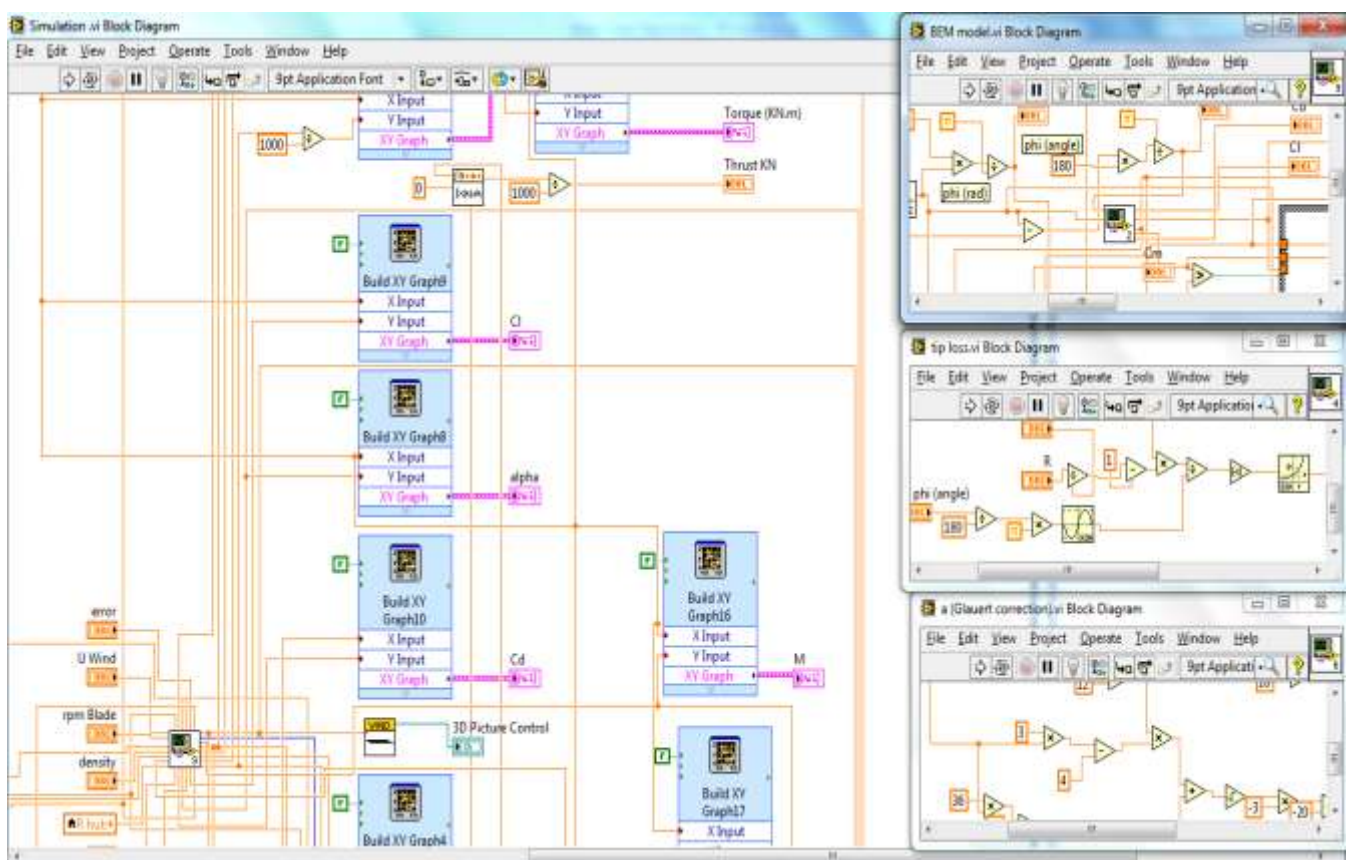

Figure B.4: Block diagram of the BEM code

C. Progressive Fatigue Damage Model

The flowchart that was presented in figure 5.1 along with the degradation rules for the strengths and the stiffness that must be repeated till failure is reached was also modeled using LabView. The user interface of this model is shown in fig C.1 and some of the block diagrams appear in fig C.2.
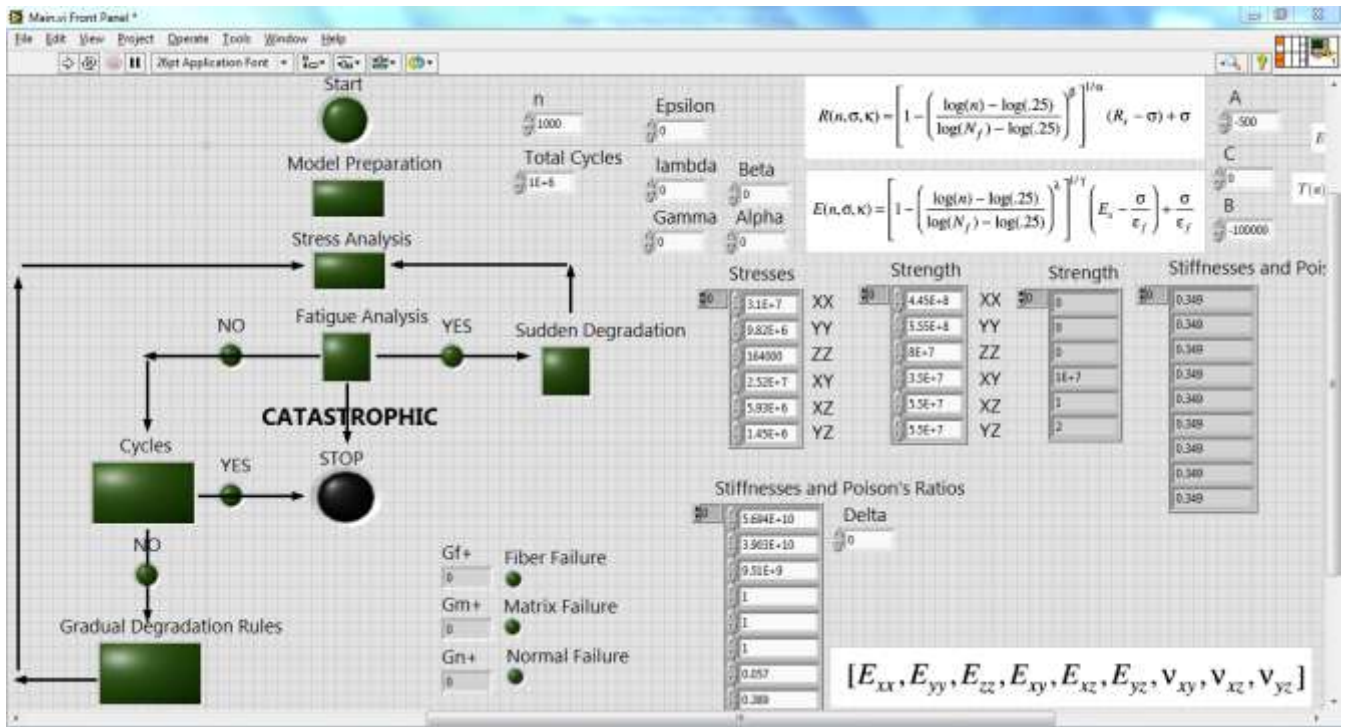

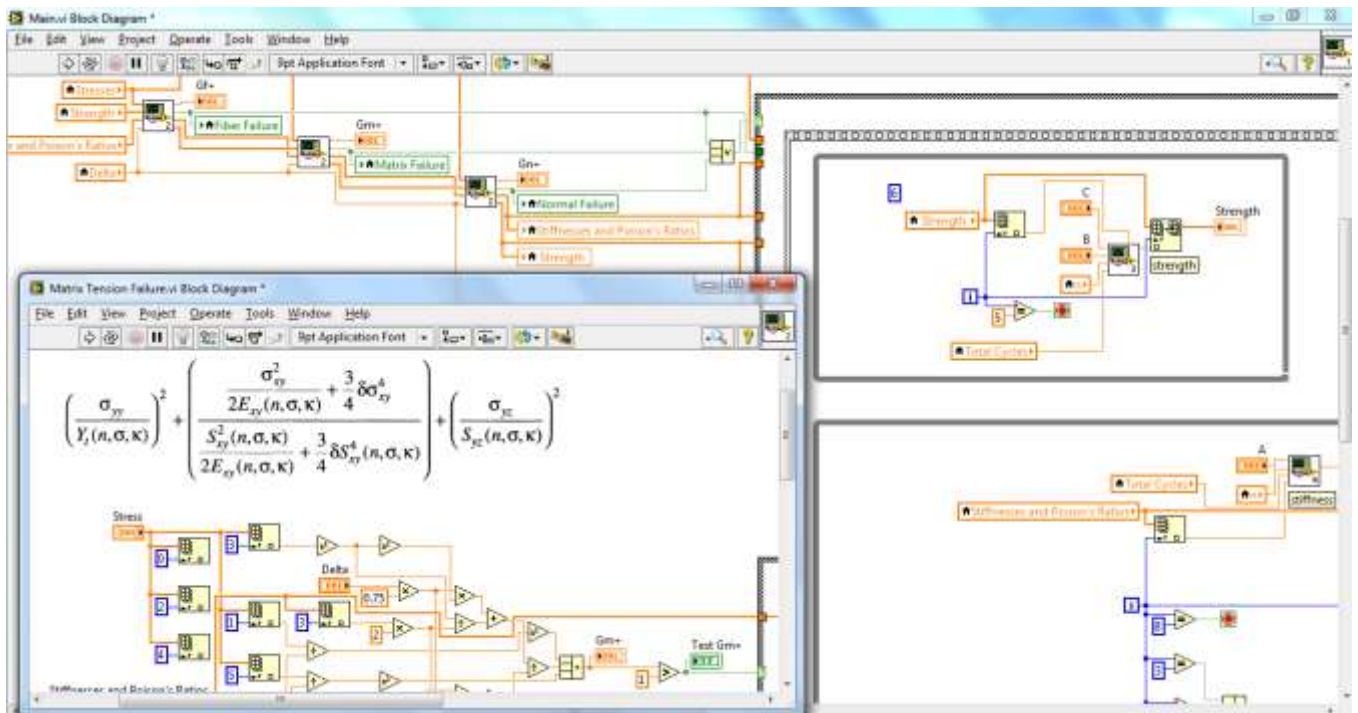**Figure C.1: The user interface for the progressive fatigue damage model**

Figure C.2: Block diagram of the progressive damage model

REFERENCES

[1] **NORLIN** J, **JÄRPNER** C, Fluid Structure Interaction on Wind Turbine Blades, *Master's Thesis in Solid and Structural Mechanics and Fluid Dynamics*, Chalmers University of Technology, Sweden, (2012)

[2] **MULLEN** B.J, ANSYS WB - Wind Turbine Blade, Cornell University, *Internet Online*, (2013)
https://confluence.cornell.edu/display/SIMULATION/Home

[3] **HALLAL** A, **YOUNES** R, **FARDOUN** F, Improved analytical model to predict the effective elastic properties of a 2.5D interlock woven fabric composite, *Composite Structures 94 3009–3028*, (2012)

[4] **SHOKRIEH** M, **LESSARD** L, Progressive Fatigue Damage Modeling of Composite Materials, Part I: Modeling, *Journal of Composite Materials* 2000 34: 1056, July, (2000)

[5] **VERELST** D, Flexible Wind turbine Blades: a BEM-FEM coupled model approach, *Master Thesis Report*, Delft University of Technology, January, (2009)

[6] **AHLSTRÖM** A, Aeroelastic Simulations of Wind Turbine Dynamics, *Doctoral Thesis*, Royal Institute of Technology, Department of Mechanics, Stockholm, Sweden, April, (2005)

[7] **MANWELL** J.F, **MCGOWAN** J.G, **ROGERS** A.L, Wind Energy Explained − Theory, Design and Application, Chapter 3 Aerodynamics of Wind Turbines, *John Wiley & Sons Ltd*, (2002)

[8] **PROFESSIONAL SERVICES GROUPS**, ADAMS/WT 2.0 User's Guide, *Technical report*,
Mechanical Dynamics, 6530 E. Virginia St. Mesa, AZ 85215, (1998)

[9] **WILSON** B, An aerodynamics and dynamics analysis code for horizontal-axis wind turbines. *Internet Online*, (27 Mars 2001)
http://wind2.nrel.gov/designcodes/fastad/

[10] **LARSEN** T.J, **HANSEN** A.M, Aeroelastic effects of large blade deflections for wind turbines, *The Science of making Torque from Wind*, pages 238–246, Delft University of Technology Roskilde, Denmark, (2004)

[11] **HANSEN** A.C, **LAINO** D.J, User's Guide: YawDyn and AeroDyn for ADAMS, *Technical Report*, Mechanical Engineering Department, University of Utah, Salt Lake City, UT, (1998)

[12] **HOLIERHOEK** J, Aeroelasticity of Large Wind Turbines, *Doctoral thesis*, Aerospace Engineering Department, Delft University of Technology Roskilde, Denmark, (2008)

[13] **ABEDI** H, Aerodynamic loads on rotor blades, *Master's thesis*, Chalmers University of Technology, (2011)

[14] **MARTIN** O, **HANSEN** L, Aerodynamics of Wind Turbines, *Earthscan*, (2008)

[15] **WEINZIERL** G, A BEM Based Simulation-Tool for Wind Turbine Blades with Active Flow Control Elements, *Diploma* Thesis, Technical University of Berlin, (2011)

[16] **MORIARTY** P.J, **HANSEN** A.C, AeroDyn Theory Manual, *Technical Report*, NREL/TP-500-36881, National Renewable Energy Laboratory NREL, Golden, Colorado, (January 2005)

[17] **DRELA** M, XFOIL Subsonic Airfoil Development System, *Software*, (November 2007)
http://web.mit.edu/drela/Public/web/xfoil/

[18] **KNILL** T.J, The application of aeroelastic analysis output load distributions to finite element models of wind, *Wind Engineering Volume 29 Number 2*, pp. 153-168(16), (March 2005)
http://dx.doi.org/10.1260/0309524054797104

[19] **MAHERI** A, **NOROOZI** S, WTAB: a computer program for predicting the performance of horizontal axis wind turbines with adaptive blades, *Renewable Energy 31*, 1673-1685, (2006)
http://dx.doi.org/10.1016/j.renene.2005.09.023

[20] **MANWELL** J.F, **MCGOWAN** J.G, **ROGERS** A.L, Wind Energy Explained – Theory, Design and Application, Chapter 6 Wind Turbine Design, *John Wiley & Sons Ltd*, (2002)

[21] **COMANHO** P, Failure Criteria for Fiber-Reinforced Polymer Composites, Department of Mechanical Engineering and Industrial Management Faculty of Engineering, University of Porto, (2002)

[22] **TSAI** S.W, **WU** E. M, A General Theory of Strength for Anisotropic Materials, *Journal of Composite Materials*, 58-80, (1971)

[23] **SMITH** H, Predictions of the original and truncated maximum-strain failure models for certain fibrous composite laminates, *Composites Science and Technology*, 58:1151-79, (1998)

[24] **HAGE** C, Modélisation du comportement élastique endommageable de matériaux composites à renfort tridimensionnel - Troisième partie: Modélisation, *Doctoral Thesis,* Université de technologie de Compiègne, (October 2006)

[25] **HALLAL** A, **YOUNES** R, **FARDOUN** F, Review and comparative study of analytical modeling for the elastic properties of textile composites, *Composites part B: Engineering Volume 50*, Pages 22-31, (July 2013)

[26] **VASSILOPOULOS** A.P, **KELLER** T, Fatigue of Fiber-reinforced Composites, *Engineering Materials and Processes*, Springer, ISSN 1619-0181, (2011)

[27] **SENDECKYJ** G.P, Life prediction for resin-matrix composite materials, *Fatigue of Composite Materials*, Elsevier, Amsterdam, pp. 431–483, (1991)

[28] **HASHIN** Z, **ROTEM** A, A fatigue failure criterion for fibre–reinforced materials, *Journal of Composite Materials* 7(4), 448–464 (1973)

[29] **PHILIPPIDIS** T.P, **VASSILOPOULOS** A.P, Complex stress state effect on fatigue life of GFRP laminates, Part I, Experimental. Int. J. Fatigue 24(8), 813–823, (2002)

[30] **SHOKRIEH** M.M, **YAZDI** M.H, A Simplified Approach to Fatigue Damage Modeling of Composite Laminates with Stress Concentration: Regional Elements Model, *Composites Research Laboratory*, Mechanical Engineering Department, Iran University of Science and Technology Tehran, 16846-13114, Iran, (2009)

[31] **PAPANIKOS** P, **TSERPES** K.I, **PANTELAKIS** S, Modelling of fatigue damage progression and life of CFRP laminates, *Fatigue Fracture Engineering Master Structure,* INSTRAM, (2002)

[32] **GALLARDO** P.A.L, Static and Fatigue Analysis of Wind Turbine Blades Subject to Cold Weather Conditions Using Finite Element Analysis, *Master Thesis*, Department of Mechanical Engineering, Catholic University of Chile, (2011)